

Washington University in St. Louis

Washington University Open Scholarship

Arts & Sciences Electronic Theses and
Dissertations

Arts & Sciences

Summer 8-15-2019

Investigation and Classification of Planetary Materials and Surfaces using Novel Methods to Analyze Large Compositional Datasets: Quantitative X-ray Compositional Mapping and Lunar Reconnaissance Orbiter Narrow Angle Camera Photometric Analysis

Timothy Michael Hahn
Washington University in St. Louis

Follow this and additional works at: https://openscholarship.wustl.edu/art_sci_etds



Part of the [Geology Commons](#)

Recommended Citation

Hahn, Timothy Michael, "Investigation and Classification of Planetary Materials and Surfaces using Novel Methods to Analyze Large Compositional Datasets: Quantitative X-ray Compositional Mapping and Lunar Reconnaissance Orbiter Narrow Angle Camera Photometric Analysis" (2019). *Arts & Sciences Electronic Theses and Dissertations*. 1907.

https://openscholarship.wustl.edu/art_sci_etds/1907

This Dissertation is brought to you for free and open access by the Arts & Sciences at Washington University Open Scholarship. It has been accepted for inclusion in Arts & Sciences Electronic Theses and Dissertations by an authorized administrator of Washington University Open Scholarship. For more information, please contact digital@wumail.wustl.edu.

WASHINGTON UNIVERSITY IN ST. LOUIS

Department of Earth and Planetary Sciences

Dissertation Examination Committee:

Bradley L. Jolliff, Chair

Raymond E. Arvidson

Robert F. Dymek

Michael J. Krawczynski

Mark S. Robinson

Investigation and Classification of Planetary Materials and Surfaces using Novel Methods to
Analyze Large Compositional Datasets: Quantitative X-ray Compositional Mapping and Lunar
Reconnaissance Orbiter Narrow Angle Camera Photometric Analysis

by

Timothy M. Hahn Jr.

A dissertation presented to
The Graduate School
of Washington University in
partial fulfillment of the
requirements for the degree
of Doctor of Philosophy

August 2019
St. Louis, Missouri

© 2019, Timothy M. Hahn Jr.

Table of Contents

List of Figures	iv
List of Tables	vii
Acknowledgments	viii
Abstract of the Dissertation	x
1.1 Big Data Analytics in Planetary Science.....	1
1.2 Challenges in Big Data Applications and Analysis.....	3
1.3 Topics of the Dissertation.....	3
1.4 Statement of Labor	5
Chapter 2: Local Geology and Regolith at the Apollo 17 Landing Site from the Perspective of LROC NAC Photometric Analysis	9
Abstract.....	9
2.1 Introduction	10
2.2 Methods	12
2.2.1 Hapke photometric modeling	12
2.2.2 Model Implementation	16
2.2.3 Data preparation	18
2.2.4 Photometric series.....	20
2.2.5 Compositional Calibration.....	21
2.3 Results	23
2.3.1 Validation, Topography removal, and analysis of uncertainty.....	23
2.3.2 Hapke parameter maps	26
2.3.3 Compositional calibration.....	27
2.3.4 Maturity effects.....	29
2.4 Discussion.....	30
2.4.1 South Massif Light-Mantle Deposit(s) and Identification of Tycho Impact Melts.....	31
2.4.2 Ballistic Mixing of Lithologies on Massif Slopes.....	33
2.4.3 Pyroclastic Deposits at Apollo 17	33
2.5 Summary and Conclusions	34
Figures	36
Tables.....	68
Chapter 3: Characterizing the Geochemical and Lithologic Diversity of the Vestan Megaregolith: Implications for Remote Sensing and Planetsimal Differentiation	73
Abstract.....	73

3.1 Introduction	74
3.2 Materials and Methods	77
3.2.1 Samples.....	77
3.2.2 Electron Probe Microanalysis (EPMA).....	77
3.2.3 Laser Ablation ICP-MS.....	78
3.2.4 Instrumental neutron Activation Analysis (INAA)	79
3.2.5 Fused bead analysis	79
3.2.6 Compositional and Mineralogical Mapping by EPMA.....	81
3.3 Results	84
3.3.1 Petrography.....	84
3.3.2 Bulk Geochemistry	85
3.3.3 Geochemistry and Textures of Vestan Lithologies	87
3.3.4 Mineralogic and Lithologic Distribution Maps.....	90
3.4 Discussion.....	91
3.4.1 Pairing of the Dominion Range 2010 Howardites.....	91
3.4.2 Recognition of Distinct Lithologies	93
3.4.3 Samples of the Vestan Megaregolith.....	94
3.4.4 Implications for Remote Sensing	98
3.5 Conclusions and Summary	99
Figures	100
Tables.....	124
Chapter 4: A Novel Approach to Petrologic Investigations Using Quantitative Compositional Mapping and Image Processing: A view from analysis of meteorite sample NWA 2995..	133
Abstract.....	133
4.1 Introduction	134
4.2 Sample NWA 2995.....	135
4.3 Analytical procedure.....	136
4.3.1 Data acquisition	136
4.3.2 Mineralogic classification algorithms and routines.....	137
4.3.3 Ground-truth validation:	139
4.4 Results and Discussion	140
4.6 Summary and Future Work	141
Figures	143
Tables.....	155
References	156

List of Figures

Figure 2.1: The Taurus-Littrow Valley, WAC global mosaic	36
Figure 2.2: Variation diagram of Al_2O_3 vs. mafic content ($FeO+MgO+TiO_2$) for Apollo soils.....	37
Figure 2.3: Location of Apollo 17 sample stations and Lunar Roving Vehicle traverses	38
Figure 2.4: Photometric angles of NAC images for regional mosaic and photometric series.....	39
Figure 2.5: Input datasets for photometric processing.....	40
Figure 2.6: Reflectance profiles highlighting changes in apparent reflection.....	41
Figure 2.7: Locations of individual sampling sites at each sample station and LRV stop	42-44
Figure 2.8: Apollo 16 Lunar international standard calibration target	45
Figure 2.9: N-S transect across Camelot crater	46-47
Figure 2.10: E-W transect across Camelot crater	48-49
Figure 2.11: NE-SW transect across Bear Mountain	50-51
Figure 2.12: NW-SE transect across Bear Mountain	52-53
Figure 2.13: Effects of viewing and illumination geometry on the apparent surface	54-55
Figure 2.14: Regional scale single scattering albedo map of the valley of Taurus-Littrow	56
Figure 2.15: Probability density plot of select regions of interest within the TLV	57
Figure 2.16: Probability density plot of three basalt regions	58
Figure 2.17: Compositional correlation between the mafic content and single scattering albedo of Apollo 17 soils	59
Figure 2.18: Regional map of the mafic content within the valley of Taurus-Littrow.....	60
Figure 2.19: Effect of Maturity on single scattering albedo.....	61
Figure 2.20: Oblique view of the Taurus-Littrow valley showing South Massif.....	62
Figure 2.21: Average single scattering albedo of surface units near South Massif.....	63
Figure 2.22: High-resolution single scattering albedo map of South Massif and adjacent light mantle deposit.....	64

Figure 2.23: Summary statistics for surface units near South Massif.....	65
Figure 2.24: Oblique view of the Taurus-Littrow valley showing the locations of low albedo material....	66
Figure 2.25: Single scattering albedo map of Mons Vitruvius.....	67
Figure 3.1: Locations of the six DOM 10 howardites collected during the 2010 ANSMET field season.....	100
Figure 3.2: Summary graphic of the compositional mapping procedures	101
Figure 3.3: Element variation diagram for Cr and Ca	102
Figure 3.4: Element variation diagrams for select major- and trace-elements in the DOM 10...	103
Figure 3.5: Element variation diagram for K and La determined by INAA.....	104
Figure 3.6: INAA and fused bead data comparison.....	105
Figure 3.7: Comparison of fused bead data to literature data.....	106
Figure 3.8: Pyroxene compositions for the DOM 10 howardites	107
Figure 3.9: Rare earth-element chemistry of select pyroxenes in the DOM 10 howardites.....	108
Figure 3.10: Examples of types 1 and 2 diogenite lithic clasts observed in the DOM 10 howardites	109
Figure 3.11: Examples of types 3 and 4 diogenite polycrystalline clasts	110
Figure 3.12: Type 5 diogenite polymineralic lithic clast example	111
Figure 3.13: Minor-element concentrations vs. Mg# in diogenite pyroxenes	112
Figure 3.14: Rare earth element patterns for diogenite mineral fragments	113
Figure 3.15: Examples of cumulate eucrite lithic clasts	114
Figure 3.16: Basaltic eucrite lithic clasts with granoblastic textures	115
Figure 3.17: Types 5 through 8 basaltic eucrite lithic clasts and mineral fragments	116
Figure 3.18: Example of harzburgitic-dunitic lithology identified by Hahn et al. (2018) in the DOM 10 howardites.....	117
Figure 3.19: Dacite clast identified in the DOM 10 howardites by Hahn et al. (2018).....	118

Figure 3.20: Lithologic distribution maps	119
Figure 3.21: Lithologic distribution maps for DOM 10838 and 10839.....	120
Figure 3.22: Lithologic distribution maps for DOM 10105 and 10837.....	121
Figure 3.23: Calculated ratios of the abundances of eucrite to diogenite for various HEDs	122
Figure 3.24: Plagioclase depletion in DOM 10 howardites	123
Figure 4.1: Sawn face of feldspathic fragmental breccia NWA 2995.....	143
Figure 4.2: Backscattered electron image of NWA 2995.....	144
Figure 4.3: Schematic Venn diagram describing the components of a comprehensive petrologic investigation	145
Figure 4.4: Summary graphic of the compositional mapping procedures	146
Figure 4.5: Quantitative elemental concentration maps	147
Figure 4.6: Schematic of two main approaches to machine learning applications in quantitative compositional mapping and mineralogic classification	148
Figure 4.7: Unsupervised clustering results for subophitic olivine basalt and map area 1.....	149
Figure 4.8: Supervised classification results for subophitic olivine basalt and map area 1.....	150
Figure 4.9: High spatial resolution classification images of lithic clasts in NWA 2995.....	151
Figure 4.10: Unsupervised k-means clustering of isolated pyroxene data	152
Figure 4.11: Detailed view of supervised classification results	153
Figure 4.12: End-member compositions for pyroxene types	154

List of Tables

Table 2.1: Image data for Apollo 17 regional mosaic	68
Table 2.2: Image data for the photometric series at Apollo 17.....	69
Table 2.3: Average Composition of Apollo 17 soil samples and LRV surface soils	70-71
Table 2.4: External for ground-truth calibration sites.....	72
Table 3.1: Summary of attributes for howardite pairing groups.....	124
Table 3.2: Summary of attributes for howardite pairing groups.....	125
Table 3.3: Summary of attributes for howardite pairing groups.....	125
Table 3.4: Bulk geochemistry of DOM 10 howardite subsamples determined by INAA	126
Table 3.5: Summary of lithologic diversity in the DOM 10 howardites	127
Table 3.6: Lithologies identified within each howardite thin-section	127
Table 3.7: Representative pyroxene and olivine compositions from diogenites in the DOM 10 howardites.....	128
Table 3.8: Rare earth-element chemistry of selected diogenite lithologies	128
Table 3.9: Representative pyroxene compositions in cumulate eucrite lithic clasts.....	129
Table 3.10: Representative pyroxene compositions in basaltic eucrite lithic clasts	130
Table 3.11: Mineral modes determined for thin-sections from the DOM 10 howardites.....	131
Table 3.12: Comparison of mineralogical characteristics for selected howardites.....	132
Table 4.1: Calculated bulk composition of selected regions in NWA 2995.....	155

Acknowledgments

I am tremendously indebted to everyone who has provided unwavering encouragement and guidance throughout my graduate career. First and foremost, I would like to thank my remarkable wife, Erika, who has been by my side since the very beginning. Without her love, patience, and belief in me, I would certainly not be where I am today. Her dedication throughout these grueling years, and the many sacrifices she has made at each step, are beyond comprehension and I am forever grateful. Through all the sleepless nights and endless days of traveling we have cried together, laughed together, and managed to raise two beautiful children. Although this journey has been a difficult one, we have made it through this together. I am eagerly awaiting the many years and adventures ahead, and I look forward to the shade while standing in her shadow.

To my family and friends, who have marveled at what I have accomplished, I share this achievement with you because without your emotional and financial support this would have never been possible. All of your encouraging and comforting words have allowed me to get through some of my worst days, for which I am deeply appreciative. To those who have help our family through rough times and when I was unable to be present, your support means more than you may ever know. Lastly, through all the curiosity and interest you have shown, you have made this journey much more memorable to share the wonders of space with you.

I would like to express my genuine appreciation for my many mentors Drs. Brad Jolliff, Hap McSween, and Larry Taylor for their guidance and advice throughout my graduate career. Most importantly, I am grateful for my advisor, Dr. Brad Jolliff, who has provided tremendous support and understanding during my time at Washington University in St. Louis and has allowed me academic freedom in pursuit of my many and diverse research projects. It was a privilege to work under such a renowned lunar scientist. I thank Paul Carpenter for the endless advice and

conversations about quantitative compositional mapping, compositional data analysis, and image processing. I would also like to give thanks to my research colleagues, Ryan Watkins and Anna Schonwald, who have spent many hours discussing and testing the photometric methods developed in this dissertation. And, to my fellow graduates who have shared this journey with me, it was a pleasure to have worked with you and grow together. Finally, I would like to thank NASA for support of the Lunar Reconnaissance Orbiter mission and the LROC Operations Team for making the data used in this research available; the Department of Earth and Planetary Science, who provided financial support during my early years; and the LRO Project, through an LROC subcontract to Washington University, for financial support throughout my last two years.

Timothy M. Hahn Jr.

Washington University in St. Louis

August 2019

Abstract of the Dissertation

Applications of Big Data Analytics in Planetary Science: Novel Methods for Investigation and
Classification of Planetary Materials

by

Timothy M. Hahn Jr.

Doctor of Philosophy in Earth and Planetary Sciences

Washington University in St. Louis, 2019

Scott Rudolph Professor Bradley L. Jolliff, Chair

Our understanding of planetary bodies and their surfaces originates from measurements made by spacecraft instruments and laboratory analysis of extraterrestrial materials. Integration of these datasets can significantly advance the fields of planetary geology and geochemistry. The goal of my dissertation research has been to develop novel methods for interrogating extraterrestrial samples and planetary regoliths, with an emphasis on integrating these complementary datasets. Additionally, my research has focused on utilizing ‘big data’ within the geoscience and planetary science communities, whether that data be geospatial or geochemical in nature. My dissertation research involves two separate, but related projects: (1) coupling Apollo 17 sample analyses with orbital observations from the Lunar Reconnaissance Orbiter Camera (LROC); and (2) development of quantitative compositional mapping (QCM) and lithologic mapping (LM) techniques using the electron microprobe, with specific applications demonstrated using vestan and lunar meteorites.

For the Apollo 17 photometry research, the effects of composition, surface maturity, mineralogy, and glass content on the photometric properties of the lunar surface were investigated using Apollo 17 soil compositions as ground truth. A regional Hapke photometric parameter map of Taurus-Littrow Valley (TLV) on the Moon was produced and provides information about the photometric properties of the lunar regolith at a pixel scale of ~ 5 mpp. Finally, an empirical calibration was developed to relate the photometric properties (e.g., single scattering albedo) of the surface to the mafic content of Apollo 17 soils (wt.% MgO+FeO+TiO₂). This relationship was used to generate a regional, topography-corrected compositional map of the TLV at high-resolution (~ 5 meters per pixel; mpp). Specifically, LROC Narrow Angle Camera (NAC) images were combined with NAC-derived digital terrain models to solve for photometric parameters by taking local illumination geometry into account, and thus allowing photometric parameters to be determined at a pixel scale of NAC DTMs (~ 5 meters per pixel). Locations of the Apollo samples and Lunar Roving Vehicle (LRV) stations, along with physiochemical information of soils collected from those stations, were used to precisely locate each sample in NAC images, and to determine the correlation between the single scattering albedo and various measures of composition such as the alumina (Al₂O₃) content, which corresponds to high-albedo anorthositic components, or the mafic index (FeO+MgO+TiO₂), which corresponds to the low-albedo mafic mineral components. The strongest correlation was observed for the mature soils, presumably because the soil maturation process breaks rocks and minerals down to a similar fine grain size. Additionally, the photometric data are self-consistent for incidence angles less than ~ 60 degrees. Using Bear Mountain as a test case, we describe a very effective method for removing slope effects, except for the steepest slopes where immature regolith occurs, by using the photometric parameters determined from NAC DTM data to account for local illumination geometry. Finally,

we make inferences about the local geology, where for example, we examine the photometric characterization of Tycho impact melt at Apollo 17 and discuss the potential for Tycho impact melt in Station 2 soils.

For the project on vestan and lunar meteorites, my dissertation research involved developing data processing protocols, multivariate statistical classification routines, and data interpretation workflows for QCM and LM. These methods, along with standard geochemical analyses (e.g., electron probe microanalysis and instrumental neutron activation analysis), were used to quantitatively characterize the mineralogic and lithologic heterogeneity (modal abundance and mineral compositions) of vestan and lunar meteorite samples using non-destructive techniques. For example, six paired howardites, collected from the Dominion Range, Antarctica, during the 2010 ANSMET field season, were extensively characterized using petrography, electron probe microanalysis (EPMA), laser ablation ICP-MS, instrumental neutron activation analyses (INAA), and fused-bead (FB) analysis by EPMA. These howardites contain abundant lithic clasts of eucritic and diogenitic compositions, as well as atypical lithologies only recently recognized (dacite and Mg-rich harzburgite). Additionally, we identified secondary material (breccia-within-breccia and impact melt) derived from multiple impact events. We describe the characteristics of the howardites, and the lithic clasts they contain, to (1) establish the range and scale of petrologic diversity, (2) recognize inter- and intra-sample mineralogical and lithological heterogeneity, (3) confirm the initial pairing of these stones, and (4) demonstrate the magmatic complexity of Vesta, and by inference, early formed planetesimals. We identified a minimum of 21 individual lithologies represented by lithic clasts >1 mm, based on textural and geochemical analysis; however, more lithologies may be represented as comminuted mineral fragments. Large inter- and intra-sample variations exist between the howardites, with distinct diogenite:eucrite and

basaltic eucrite:cumulate eucrite ratios, which may be identifiable in Dawn data. We conclude that these meteorites are fragments of the megaregolith and have the potential to represent the largest sample of the vestan surface and are therefore ideal for remote sensing calibration studies.

In summary, the results from my dissertation projects are used to: (1) correlate the photometric properties of the lunar regolith to physiochemical characteristics of Apollo 17 soil samples and address outstanding science questions at the Apollo 17 landing site (e.g., characterization of impact melt from Tycho crater); and (2) assess the extent of magmatic differentiation in the vestan crust, and by inference early planetesimals. This dissertation offers new methods for investigating small-scale compositional variations on the Moon; and provides new, highly effective methods for petrologic investigations of complex samples for which only limited quantities exist (e.g., returned lunar and asteroid samples).

Chapter 1: Introduction to the Dissertation

The formation and geochemical evolution of planetary surfaces and their interiors has long been a fundamental component of planetary science and is crucial for answering multidisciplinary science questions regarding the origin and evolution of planets. Questions of interest include the following: How are planets formed and what is the range of diversity in the initial planetary building blocks?; how do the planetary building blocks differentiate and evolve geochemically?; how are planetary regoliths developed and what information can they tell us about the underlying geology?; and what information can be understood from sparse samples of planetary bodies? The advent of sophisticated spacecraft instruments and advances in microanalysis techniques has provided new methods for investigating planetary surfaces and samples originating from planetary surfaces and interiors. This dissertation explores these new datasets and methods, while giving specific attention to exploiting ‘big data’ and discussing the challenges of working with such datasets.

1.1 Big Data Analytics in Planetary Science

The rapid growth and availability of ‘big data’ in the geosciences and planetary sciences has created unique challenges and opportunities over the last decade. Recent technological developments have given rise to advanced data collection systems capable of generating complex, multi-dimensional datasets that require adopting new methods for managing, processing, and interpreting data products. For example, the objectives of the Lunar Reconnaissance Orbiter (LRO), launched in 2009, were to map the lunar surface at new spatial scales with a variety of detectors in order to: 1) identify and characterize safe landing sites; 2) locate and characterize potential resources; and 3) characterize the lunar space radiation environment (Chin et al., 2007).

To achieve the LRO objectives and the individual science goals for each instrument, the LRO spacecraft has been in science operations mode for ~95% of the mission, generating over 450 Gbits of data per day (Tooley et al., 2010); the bulk of these data, ~440 Gbits, are created by the three imaging systems of the Lunar Reconnaissance Orbiter Camera (LROC), the two Narrow Angle Cameras (NACs) and the Wide angle camera (WAC). The photometric processing and interpretation of the high-resolution NAC imagery collected by LROC is the first topic examined in this dissertation.

Another example of the growth and availability of ‘big data’ occurs in the fields of geochemistry and quantitative petrology. The latest advances in microanalysis have provided new methods for collecting geochemical data in ways that enhance petrologic studies. For example, quantitative compositional mapping is a recently developed method for creating fully quantitative elemental maps using the electron microprobe (Carpenter et al., 2013). Unlike typical EPMA elemental maps, quantitative compositional maps are calibrated using standard wavelength dispersive background subtraction and Probe for EPMA™ software. The calibration of qualitative elemental maps to quantitative compositional maps allows comparison to high-precision electron microprobe spot analysis and permits the geochemistry and mineral chemistry of a rock thin-section to be extensively characterized. The quantitative compositional maps can, in a sense, be regarded as big data in the field of geochemistry and quantitative petrology, where typical petrographic and EPMA studies consist of potentially a few hundred data points and the quantitative compositional maps are comprised of > 1 million complete chemical analyses. Therefore, this dissertation examines the use of quantitative compositional mapping for conducting extensive and thorough petrographic and geochemical investigations of vestan and lunar meteorite samples.

1.2 Challenges in Big Data Applications and Analysis

The emergence of big data science within the last century has given rise to geological big data and new fields within the geosciences (e.g., mathematical geology). As such, geological big data has created new ways of answering unresolved science questions and testing scientific hypotheses; however, geological big data has also generated challenges in the applications and analysis of such datasets. Specifically, issues related to the management and storage of big data, as well as manipulating, processing and analyzing these large datasets, have served as impediments to fully realizing the applications of geological big data. This dissertation explores the use of geological big data, mainly high-resolution NAC imagery of the lunar surface and geochemical data consisting of millions of data points, and will give specific attention to addressing the manipulation, processing, and analysis of big data in the geosciences and planetary science.

1.3 Topics of the Dissertation

This dissertation investigates new methods for investigating extraterrestrial samples and planetary regoliths and demonstrates specific applications by addressing outstanding science questions in the accompanying fields. Two principal datasets are used for the dissertation projects: 1) LROC high-resolution NAC imagery; and 2) geochemical data collected by a variety of analytical instruments. For clarity, each dataset is described in appropriate detail where it is first mentioned.

Chapter 2 focuses on using Hapke's photometric model to characterize the photometric properties of the regolith at the Apollo 17 landing site. Photometric processing routines are developed to capitalize on the large number of NAC images available for the Apollo 17 landing site and increase the confidence in the retrieval of physical properties from a theoretical, physics-

based, complex light-scattering model. To validate the photometric model and the retrieved photometric properties, the soil samples collected by the Apollo 17 astronauts are used as ground-truth. The ground-truth soils are then used to relate the photometric properties to geologically interpretable characteristics (e.g., composition) of the regolith that are useful for interpreting the local geology at the Apollo 17 landing site. We report a strong correlation between the single scattering albedo of the lunar regolith and the composition of soils collected at corresponding sites, which is best observed in mature soils.

Chapter 3 focuses on characterizing the petrologic diversity of the asteroid 4 Vesta by conducting a detailed study of nine meteorites from the Dominion Range 2010 howardite pairing group. Several methods and analytical instruments were used to fully characterize each sample, and include: petrographic analysis, electron probe microanalysis, laser ablation ICP-MS, and instrumental neutron activation analyses. These nine howardites contain abundant lithic clasts of eucritic and diogenitic composition, as well as atypical lithologies only recently recognized (dacite and Mg-rich harzburgite; Hahn et al., 2017; Hahn et al., 2018). Secondary material (breccia-within-breccia and impact melt) was identified and was likely derived from multiple impact events. Chapter 3 describes the characteristics of the howardites, and the lithic clasts they contain, to (1) establish the range and scale of petrologic diversity, (2) recognize inter- and intra-sample mineralogical and lithological heterogeneity, (3) confirm the initial pairing of these stones, and (4) demonstrate the magmatic complexity of Vesta, and by inference, early formed planetesimals. A minimum of 21 individual lithologies, identified based of textural and geochemical analysis and represented by lithic clasts >1 mm, are reported; however, additional lithologies may be represented as comminuted mineral fragments. Large inter- and intra-sample variations are reported between the howardites, with distinct diogenite:eucrite and basaltic eucrite:cumulate

eucrite ratios, which may be identifiable in Dawn data. The Dominion Range 2010 howardite pairing group is representative of the megaregolith and has the potential to represent the largest sample of the vestan surface and is therefore ideal for remote sensing calibration studies.

Chapter 4 demonstrates the applications of new, non-destructive microanalytical techniques for conducting extensive petrologic investigations and reports the first integration of fully quantitative EPMA compositional mapping with remote sensing software Environment for Visualizing of Images (ENVI) and IDL Workspace. Compositional, mineralogical, and lithological distribution maps of complex lunar meteorite breccia Northwest Africa (NWA) 2995 are used to demonstrate the manipulation, processing, analysis, and image classification procedures to relevant petrologic problems. Supervised classification procedures in ENVI (i.e., minimum distance classification in n-dimensional chemical space) are used to classify the mineralogy of NWA 2995 (e.g., bulk sample, matrix, and individual lithic clasts). The resulting classification images allow the extraction of processed wt. % element data by mineralogy, clast type, and mineral fragments derived from the matrix. Images can then be generated that contain information regarding stoichiometry, mineral end-member compositions, elemental ratios, phase distribution, and fracture porosity. Additionally, average mineral compositions are calculated; density-corrected bulk composition reconstructions are performed on lithic clasts, matrix components, and exsolved or zoned minerals. Our methods provide a powerful tool for petrologic investigations and alleviate current issues with similar techniques. We provide a new, easily accessible, tool for the interrogation of geologic materials.

1.4 Statement of Labor

The dissertation chair, Dr. Bradley L. Jolliff, and Dr. Ryan N. Watkins of the Planetary Science Institute provided the initial motivation for Chapter 2: *Local Geology and Regolith at the*

Apollo 17 Landing Site from the Perspective of LROC NAC Photometric Analysis. The LROC team at Arizona State University made available the NAC images, NAC-derived digital terrain models (DTM), and Apollo 17 photometric series used for Chapter 2. Timothy M. Hahn Jr. developed the photometric processing routine that utilizes the High Performance Computing facilities in the Department of Earth and Planetary Science at Washington University in St. Louis and the parallel computing capabilities of the MATLAB software package; the initial foundation for photometric processing was established by Ryan N. Watkins and Matt J. Watkins and modified by Timothy M. Hahn Jr. to accommodate the ‘big data’ issues and increase the complexity of the photometric model described in this dissertation. Anna R. Schonwald assisted in debugging and testing the photometric processing routine. All NAC images and NAC-derived DTMs were processed by Timothy M. Hahn Jr.; subsequent data analysis was conducted by Timothy M. Hahn Jr. Development of the photometric processing technique and data analysis was influenced by weekly discussions with the dissertation chair, Dr. Ryan N. Watkins, and Anna R. Schonwald. The data analysis methods for Chapter 2 and the associated Python programs for data manipulation, statistical analysis, and data visualization were developed and are maintained by Timothy M. Hahn Jr., and are hosted in a publicly available GitHub repository. Supplementary data for Apollo soil compositions were compiled and graciously provided by Dr. Randy L. Korotev and Ryan N. Watkins.

The primary motivation for Chapter 3, *Characterizing the Geochemical and Lithologic Diversity of the Vestan Megaregolith: Implications for Remote Sensing and Planetesimal Differentiation*, was developed while Timothy M. Hahn Jr. pursued his Master of Science degree in Geology from the University of Tennessee, Knoxville. A portion of the data presented in Chapter 3 was collected at the University of Tennessee; specifically, the initial characterization

and preliminary electron microprobe data for the howardite meteorites was collected at the University of Tennessee. The research foundation developed at the University of Tennessee was used to advance the initial research motivations and expand the scope of the petrologic investigation of the Dominion Range 2010 howardites discussed in Chapter 3. To expand the research project, additional howardite sections and sample chips were obtained to: 1) examine inter- and intra-sample variations in greater detail; 2) characterize the bulk major-element geochemistry through EPMA of fused glass beads; 3) characterize the minor- and trace-element geochemistry of the howardites using instrumental neutron activation analysis (INAA); and 4) explore the applications of non-destructive, quantitative compositional electron microprobe mapping. The development and motivation behind Chapter 3 was realized by Timothy M. Hahn Jr. and encouraged by the dissertation chair, EPMA and XRD Facility Specialist Paul Carpenter, and previous advisors and research colleagues Drs. Hap McSween, Larry Taylor, and Nicole Lunning. All of the sample preparation and analysis was conducted by Timothy M. Hahn Jr., with the invaluable assistance and guidance from the dissertation chair, research professor emeritus and INAA expert Randy Korotev, and EPMA and XRD Facility Specialist Paul Carpenter. The analysis and visualization of the compositional data collected for Chapter 3 was completed by Timothy M. Hahn Jr.

Finally, the motivation for Chapter 4 was provided by an initial petrologic investigation of lunar meteorite NWA 2995, which was carried out by EPMA and XRD Facility Specialist Paul Carpenter. The initial characterization revealed a clast-rich lunar meteorite breccia with a diversity of lithic clast compositions, some unique; these characteristics, and the availability of previously published bulk compositional data and mineral compositions, were recognized by Timothy M. Hahn Jr. as a prime target for demonstrating the useful applications of quantitative compositional

mapping. The methods of quantitative compositional mapping were developed by EPMA and XRD Facility Specialist Paul Carpenter and John J. Donovan, who is the developer of widely used “Probe for EPMA” control and data processing software. The compositional mapping of lunar meteorite NWA 2995 was carried out by Paul Carpenter, with assistance from Timothy M. Hahn Jr. All subsequent data analysis (e.g., image processing, statistical analysis of compositional data, and data visualization of quantitative element maps) was carried out by Timothy M. Hahn Jr.

Each chapter in this dissertation represents the original research carried out by Timothy M. Hahn Jr. and is intended to be submitted to a scholarly journal for publication following editorial review from the dissertation chair and co-authors. Where appropriate, the shared authorship and contribution of co-authors is stated; however, the following chapters in this dissertation represent the original manuscripts currently in preparation, with minimal input from co-authors; this approach is intended to demonstrate the independent research completed by Timothy M. Hahn Jr.

Chapter 2: Local Geology and Regolith at the Apollo 17 Landing Site from the Perspective of LROC NAC Photometric Analysis

Disclosure: The following chapter is pending submission to the Journal of Geophysical Research – Planets in September 2019, following co-author revisions and is a result of the primary author’s graduate research. Co-authorship is shared with Ryan N. Watkins, Anna R. Schonwald, Anna C. Martin, Mark. S. Robinson, and Bradley L. Jolliff. Timothy M. Hahn Jr. prepared the manuscript. The content of the chapter contains the original submission materials in an unaltered form prior to co-author revisions.

Abstract

High-resolution Lunar Reconnaissance Orbiter Camera (LROC) Narrow Angle Camera (NAC) images and NAC-derived digital terrain models (DTM) are used to model the photometric properties of the lunar regolith at the Apollo 17 landing site. Soils collected during the Apollo 17 mission are used as ground truth to relate the photometric properties to physical and chemical information, such as soil maturity, composition, and mineralogy. We report a strong and quantifiable relationship between the photometric properties of the regolith and the composition and surface maturity of soil samples at a spatial resolution of 5 meters per pixel. An empirical calibration is developed to relate the single scattering albedo of the surface to the mineralogic content of soils (e.g., wt.% MgO+FeO+TiO₂ as a measure of the mafic mineralogy). This relationship is used to generate a regional, topography-corrected compositional map of the Taurus-Littrow valley (TLV) at high-resolution (~5 meters per pixel). Repeat NAC coverage (i.e., images constituting a photometric set) is used to demonstrate the robust method developed for investigating the photometry of the lunar surface. Finally, we use the photometric and compositional datasets produced to discuss the local geology within the TLV and outstanding science questions, such as the origin of the light mantle deposit at the base of South Massif.

2.1 Introduction

Apollo era and orbital observations of the lunar surface have long been exploited to provide insight into the geology of the Moon. For example, Lucey et al. (1995,1998) used the near-global ultraviolet-visible (UVVIS) multispectral data set from the 1994 Clementine mission to derive compositional information about the lunar surface and investigate the origin of the lunar crust. More recent work to extract compositional information from UVVIS multispectral observations includes using data from the Lunar Reconnaissance Orbiter Camera (LROC) Wide Angle Camera (WAC) (e.g., Sato et al., 2017). Sato et al. (2017) used spectral variations (LROC WAC 321/415 reflectance ratio) to map the abundance and distribution of TiO_2 in areas of basaltic regolith. While most studies have relied on multispectral data and variations in the spectral response of the lunar surface, fewer studies have attempted to relate the photometric response of the surface to characteristics of geological importance (Domingue et al., 2018) using panchromatic images, especially using ground-truth observations such as soil compositions (e.g., Clegg-Watkins et al., 2017).

Understanding variations in surface reflectance, as a function of viewing and illumination geometry, provides information about the photometric response of a planetary surface. Although it is well known that the photometric properties of the lunar regolith can provide constraints on geologically important characteristics, e.g. composition, grain size, and glass content, investigations of such characteristics using orbital observations have been limited, probably due to the complexity of light scattering models, the requirement of multiple observations at different viewing and illumination geometries, and the difficulty in correcting for small-scale local topography (Domingue et al., 2018; Domingue & Vilas, 2007; Pommerol et al., 2013).

This paper is concerned with investigating the relationship(s) between the photometric properties of the lunar surface, determined from orbital observations, and the chemical/physical characteristics of soils collected at the Apollo 17 landing site. The Apollo 17 landing site, situated in Taurus-Littrow Valley (TLV; Figure 2.1), is an exceptional location on the Moon for photometric investigations for several reasons:

- 1) The LROC Narrow Angle Camera (NAC) provides extensive, high-resolution images (~0.5 mpp; meters per pixel) that have been used to construct a regional mosaic and associated high-resolution digital terrain model (DTM; 2-5 mpp; Figure 2.1).
- 2) Apollo 17 soils have highly variable compositions that almost completely span the compositional range observed in the Apollo soils (Figure 2.2).
- 3) The number and extensive documentation of the samples collected provides an exceptional ground-truth dataset (Figure 2.3) (Heiken & McKay, 1974; B. Jolliff, 1999; B. L. Jolliff et al., 1996; R. L. Korotev & Kremser, 1992; Rhodes et al., 1974; Robinson & Jolliff, 2002; Wolfe, 1981).
- 4) A recent and rigorous study to accurately locate surface features allows the precise location of individual samples to be determined (Haase et al., 2019).
- 5) The availability of a photometric sequence covering a portion of the landing site and sampling locations provides a robust dataset for validating photometric models.
- 6) The complex geology of the Taurus-Littrow Valley provides unique opportunities to validate any photometric model (e.g., Heiken and McKay 1974; Robinson & Jolliff, 2002).

In this study, we use local slope data derived from NAC DTMs to compute local incidence and emission (emergence) angles and use them with Hapke's photometric model (Hapke, 2012b) to extract the single-scattering albedo, and thus minimize illumination effects resulting from local topography. Soil samples collected during Apollo 17 are used as ground truth to explore the relationship between the photometric properties of the lunar surface at NAC scales. We use the relationships established to develop an empirical compositional calibration that enables compositional investigations of the lunar surface at NAC pixel scales (~5 mpp). Finally, we use

the knowledge gained to address science questions related to the geology of the Taurus-Littrow Valley and surrounding region.

2.2 Methods

In this section, we briefly describe our implementation of the Hapke photometric model (e.g., Hapke, 2012b) and then discuss how the photometric properties of the regolith are retrieved using LROC NAC images and NAC-derived DTMs. Finally, we describe how Apollo 17 soils are incorporated as ground truth.

2.2.1 Hapke photometric modeling

The measured reflectance of a planetary surface is controlled by the physical characteristics (e.g., particle size, shape, mineralogy, and chemical composition), as well as the viewing and illumination conditions; therefore, precise knowledge of the latter can be used to invert light scattering models to extract quantities that describe the photometric behavior of the surface (e.g., Hapke parameters). For this study, we used the most recent formulation of the Hapke model (Hapke, 2012b), which has been used extensively within the community for lunar photometric studies (Clegg-Watkins et al., 2017; Helfenstein & Shepard, 2011; Sato et al., 2014; Shepard & Helfenstein, 2007). The radiance factor (I/F) of a planetary surface can be described by the following set of equations:

$$I/F = LS(i, e) \times \frac{\omega}{4} \{p(g)[1 + B_{SO}B_S(g, h_s)] + M(i, e, \omega)\} \{1 + B_{CO}B_C(g, h_c)\} \times S(i, e, \theta, \psi) \quad (2.1)$$

where the radiance factor is the ratio of the bidirectional reflectance of a surface relative to a perfectly diffuse, normally illuminated surface (i.e., incidence = 0). We follow similar

mathematical expressions and notations described in Sato et al. (2014), and briefly describe each below:

Lommel-Seeliger function (LS) is a first approximation of diffuse reflection resulting from single scattering events, and is given by

$$LS = \frac{\mu_0}{(\mu_0 + \mu)} \tag{2.2}$$

where μ_0 and μ are the $\cos(i)$ and $\cos(e)$, respectively; the local incidence and emission angles are expressed as i and e , respectively.

The single particle phase function (SPPF), $p(g)$, describes the angular dependence of light scattering for an incident photon and is given here as the two-parameter, double Henyey–Greenstein (2PHG) function:

$$p(g) = \frac{(1 - b^2)}{2} \left(\frac{(1 + c)}{(1 - 2b \cos g + b^2)^{\frac{3}{2}}} + \frac{(1 - c)}{(1 + 2b \cos g + b^2)^{\frac{3}{2}}} \right) \tag{2.3}$$

where b ($0 \leq b \leq 1$) and c ($-1 \leq c \leq 1$) are the parameters that describe the shape and strength of the backward and forward scattering lobes, respectively. An empirical relationship exists between the b - and c -parameters (e.g., Hapke, 2012a; "hockey stick function"); the general expression is given by

$$c(b) = 3.29 \times e^{-17.4 \times b^2} - 0.908 \quad (2.4)$$

The Shadow Hiding Opposition Effect (SHOE), B_S , attempts to account for increased reflectance at small phase angles, and is given by

$$B_S(g, h_s) = \frac{1}{[1 + \tan\left(\frac{g}{2}\right) \times h_s^{-1}]}$$

(2.5)

where h_s is the angular width of the SHOE; the amplitude of the SHOE is a multiplicative factor and given by B_{SO} . Here, we approximate B_{SO} using Equation 4 and the regression parameters reported for 643 nm in Table 2 of Sato et al. (2014), where B_{SO} is the empirical approximation described by

$$B_{SO} = \frac{\alpha\omega + \beta}{\omega p(0)}$$

(2.6)

where $p(0)$ is the SPPF at zero phase and the α (2.459) and β (0.078) parameters are the regression parameters determined by Sato et al. (2014), which are apparently wavelength dependent. The ω term (also noted as w elsewhere) is the single scattering albedo.

The Isotropic Multiple-Scattering Approximation, M , is given by

$$M(i, e, \omega) = H(\cos i, \omega) \times H(\cos e, \omega) - 1$$

(2.7)

where $H(x, \omega)$ is given by Chandrasekhar (1960) and defined as

$$H(x, \omega) = \frac{(1 + 2x)}{(1 + 2x\sqrt{(1 - \omega)})}$$

(2.8)

The Coherent Backscattering Opposition Effect (CBOE), B_S , accounts for an increase in measured reflectance due to positive interference between light waves and is described by

$$B_C(g, h_c) = \frac{1 + \left[1 - e^{-\tan\left(\frac{g}{2}\right) \times h_c^{-1}}\right] \times \left[\tan\left(\frac{g}{2}\right) \times h_c^{-1}\right]^{-1}}{2 \times \left[1 + \tan\left(\frac{g}{2}\right) \times h_c^{-1}\right]^2}$$

(2.9)

where h_c is the angular width of the CBOE; the amplitude of the CBOE is given by B_{CO} . The CBOE is only important at small phase angles; however, we have chosen to include it here for the sake of completeness.

The Shadowing function, S , accounts for large-scale roughness (i.e., surface roughness larger than the particle size, but smaller than the detector footprint; Hapke, 2012b). The shadowing function depends upon the viewing and illumination geometry, where ψ is the azimuth, and the mean slope angle θ . The reader is referred to Sato et al. (2014) for the exact mathematical expression and derivation of the shadowing function. The azimuth angle, ψ , can be derived from the follow relationship:

$$\psi = \arccos \frac{\cos g - \cos e \cos i}{\sin e \sin i} \quad (2.10)$$

Inversion of the Hapke model (Equation 2.1) to solve for photometric parameters is difficult and computationally intensive owing to the nonlinear behavior and number of free parameters. Likewise, solving Equation 1 for each pixel in a NAC image makes the problem computationally intensive. In an effort to alleviate complications, we made fundamental simplifying assumptions regarding the behavior of light scattering in the lunar regolith that are grounded both theoretically and experimentally. For example, we fixed several parameters using average values determined from experimental and empirical studies (e.g., Hapke et al., 2012; Johnson et al., 2013; Sato et al., 2014). Additionally, Hapke (2012a) demonstrated the empirical relationship between the b - and c -parameters of the SPPF; therefore, we further reduced the number of free parameters by forcing the relationship in Equation 2.4.

The two photometric quantities, or “Hapke parameters”, that are of interest to this study are the single scattering albedo (ω) and the b -parameter of the SPPF. These Hapke parameters are most likely to provide information about the composition and maturity/grain size of the lunar regolith, as has been demonstrated in laboratory studies (Johnson et al., 2013).

2.2.2 Model Implementation

In addition to the complexities of the Hapke model described above, the pixel scale of LROC NAC images made the photometric correction computationally intensive. Therefore, we used the high performance computing facilities at Washington University in St. Louis and the

parallel computing capabilities of MATLAB to photometrically process NAC images within a reasonable time frame ($\sim 2\text{-}4$ days/NAC). All initial pre-processing was done using USGS ISIS3 image processing software (see § 2.2.3), where the final outputs are 4-band photometric image cubes containing the radiance factor and illumination and viewing angles.

A constrained, nonlinear global optimization algorithm (Branch et al., 1999; Byrd et al., 1988) was used to generate Hapke parameter maps for the TLV. Specifically, the Trust-Reflective algorithm in MATLAB was used to minimize a simplified form of the Hapke model and determine optimum values for ω and the b -parameter of the SPPF; the Global Optimization, Symbolic Math, and Parallel Computing tool boxes in MATLAB were used to optimize accuracy and efficiency of the algorithm (Mathworks, 2017a, 2017b, 2018a, 2018b). All NAC images were first resampled from ~ 0.5 m to 5 m, which is concordant with the NAC DTM and helps to further reduce the computation time. Using the NAC DTM as a shape model and spacecraft pointing data, backplanes were computed for the local incidence (i), local emission (e), and phase angle (g), which allows the effects of local topography on the computed albedo value to be taken into account. Box constraints for the Hapke parameters of interest, informed by previous experimental and empirical studies of the lunar regolith and regolith simulants, were applied to limit the numerical space over which the algorithm searched (Hapke, 2012a; P. Helfenstein & Veverka, 1987; Sato et al., 2014; Shepard & Helfenstein, 2011). In other words,

$$\min h(\omega, b) \text{ such that } \begin{cases} \omega, & 0 \leq \omega \leq 1 \\ b, & 0.1 \leq b \leq 0.4 \end{cases}$$

where $h(\omega, b)$ is the set of Hapke parameters of interest, and is defined by:

$$h(\omega, b) = \left\{ \frac{w}{4} [p(g) + H(\mu_0, w)H(\mu, w) - 1][1 + B_{CO}B_C(g, h_c)S(i, e, \theta)] - \frac{IoF}{LS} \right\}^2 \quad (2.11)$$

Analytical gradient and Hessian functions were derived using the Symbolic Math toolbox, which improves the accuracy of the algorithm and reduces the computation time. (Mathworks, 2018a). Because the algorithm selects twenty ω_o - and b_o -values, the solutions, and hence the Hapke parameter maps, can be regarded as numerically global solutions to the Hapke model (i.e., the effects of initial starting values on the modeled ω - and b -values are reduced and solutions are global, rather than numerically local, minimums).

The program used to photometrically process the NAC images and DTMs, and then derive the best-fit Hapke parameters (i.e., Equation 2.11) is hosted in a public GitHub repository and is openly available. All necessary documentation required to use the program and the appropriate references are provided as well. The ease of use and access to the photometric processing routine detailed here is intended to encourage new photometric studies of additional lunar sites using data from LROC NAC images.

2.2.3 Data preparation

The LROC NAC data coverage of the Taurus-Littrow Valley at Apollo 17 is extensive. For this study, we processed 44 NAC images that were used to assemble the latest Apollo 17 regional mosaic and the associated DTMs (Table 2.1). Additionally, an LROC team product photometric series is available for the Apollo 17 site and consists of 47 NAC images (Table 2.2). The photometric sequence NAC images cover 17 of the 37 sample collection sites investigated during this study (Table 2.3). Each NAC image in the photometric series was acquired under

different viewing and illumination geometries, covers approximately the same area on the surface, and has been co-registered to a single NAC DTM orthomosaic (Figure 2.4); these characteristics make the photometric series ideal for evaluating the effects of geometry on the photometric response of the lunar regolith.

Below, we briefly describe the methods used to pre-process NAC images prior to application of the photometric model. The Integrated Software for Imagers and Spectrometers 3 (ISIS3) software was used for all pre-processing; below ISIS3 commands are italicized. For simplification and clarity, a schematic diagram of our methods and input datasets is shown in Figures 2.5 and 2.6, respectively. First, each NAC DTM was first converted to a shape model using *demprep*. Next, *Ironacal* was used to perform a radiometric correction to the NAC images. *Spiceinit* was used to apply the Spacecraft & Planetary ephemerides, Instrument C-matrix and Event kernels (SPICE) data that contains information on the LRO spacecraft position, pointing, body shape and orientation, sun position that is used in conjunction with NAC DTMs to compute ground positions (latitude/longitude) and photometric angles (e.g., local incidence and emission). The echo effect was then removed from the LROC NACs using *Ironacecho*. The *reduce* command was used to decrease the pixel scale of the NAC images to $\sim 2x$ the corresponding NAC DTM, and was applied to be conservative in our estimate of the relative accuracy of the NAC DTMs and when computing photometric angles from the NAC DTMs (Henriksen et al., 2017). *Phocube* was used to generate the photometric backplanes for the phase, local emission, and local incidence angles, which are calculated using the associated NAC DTMs and SPICE data. The use of NAC DTMs provides a significant advancement over previous methods that used the assumption of a spherical Moon and reduces the error associated with uncorrected topography (Sato et al., 2014).

Finally, the NAC images were map-projected to an equirectangular projection and the NAC DTM was used to calculate a local slope map.

2.2.4 Photometric series

Photometric sites consist of numerous NAC images with overlapping surface coverage that were collected at various illumination and viewing geometries and allow reflectance variations to be investigated. Martin et al. (2018) produced a photometric series for a portion of the Apollo 17 landing site, which consists of 47 NAC images and covers 17 of the 37 samples investigated during this study. Each NAC image in the photometric sequence has undergone extensive geometric corrections, which minimizes topographic distortions (e.g., Martin et al., 2018). For Apollo 17, the NAC images in the photometric sequence were registered to the APOLLO_17_1 NAC DTM orthophoto, which then allows precise computation of photometric angles (e.g., Martin et al., 2018). For the purpose of this study, the photometric sequence allows us to 1) test whether our implementation of Hapke's photometric model adequately accounts for local topography and associated variations in illumination and viewing angles over a range of phase angles, 2) determine the reproducibility of derived Hapke parameters under different viewing and illumination geometries, and 3) independently determine photometric parameters through analysis of the phase curve. If our implementation of Hapke's model is a valid approach that generates reproducible results, we would expect to be able to determine the photometric properties of the surface, regardless of viewing and illumination geometry, and these results should be reproducible and self-consistent.

The Apollo 17 photometric series is a substantial dataset of 47 NAC images (1-5 Gigabytes per processed NAC), each with four bands (i.e., I/F , g , e , i) with even the smallest NAC image

containing >50 million pixels per band and the largest containing >150 million pixels per band; such an extensive dataset requires a customized data manipulation and analysis approach. To extract photometric data, an ArcPy script was created that works in conjunction with ArcPro to extract phase curves for individual pixels, transects, or defined ROIs. The script extracts data along with average phase curves and computes 1-sigma. Photometric data and phase curves were extracted for each Apollo 17 soil sample location that occurs within the photometric series coverage. These data were used to assess the reproducibility of derived Hapke parameters, estimate the standard error for model outputs, and further assess photometric variations between sampling stations.

2.2.5 Compositional Calibration

Numerous and extensive geochemical and petrologic studies have been conducted on Apollo soil samples, and these studies provide a wealth of information on bulk compositions, modal mineralogy, lithic and glass contents, and maturity (degree of exposure to space weathering processes; Heinken and McKay, 1974; Taylor et al, 2010). These data provide the ground-truth analyses needed to correlate photometric properties to geologically interpretable properties, such as composition. Bulk compositional data for surface soils collected during the Apollo 17 mission are listed in Table 2.3, along with additional information such as sample maturity; these data were compiled from several different sources but are for individual collection sites (Jolliff, 1999; Korotev & Kremser, 1992; Wolfe, 1981; Heinken and McKay, 1974; and references therein). Although individual samples exhibit variations in sub-sample compositions, the variations are small compared to compositional variations between soils from different sample stations (Korotev & Kremser, 1992).

A major goal of this paper is to establish the relationship(s) between the photometric properties of the lunar surface and the physiochemical characteristics of the soils. Therefore, we extracted data for the reflectance, photometric angles, and derived Hapke parameters at sites where soils were collected by the Apollo 17 astronauts, and for which we have complementary sample data. The high spatial resolution of NAC images and the recent, extensive effort by Haase et al. (2019) to accurately (± 1 m) determine and map the locations of Apollo 17 equipment and lunar landmarks allow individual sample collection sites to be located. The use of surface photography and astronaut transcripts further aids in locating sampling sites. Figure 2.7 illustrates the locations determined for individual samples. We identified and extracted data for 37 sampling sites (Figure 2.7; Table 2.3).

As shown in Figure 2.2, the Apollo 17 soils span a broad range in Al_2O_3 wt.% and mafic content ($\text{MgO}+\text{FeO}+\text{TiO}_2$), but do not necessarily capture the more feldspathic component of the lunar crust (i.e., highlands material). To address this, we included an additional, more feldspathic, area of study in our analyses in order to extend the range of compositions and mineralogy under examination. Particularly, a large region of relatively uniform feldspathic highlands near the Apollo 16 landing site was selected (Figure 2.8). We are aware, however, that this area of the Cayley plains is not typical feldspathic highlands, owing to the contribution of Imbrium ejecta, it is more mafic than typical highlands (Korotev, 1997). Soils collected by the Apollo 16 astronauts provide excellent compositional calibrations for undisturbed mature feldspathic terrains with low mafic content (McCord et al., 1981; Pieters et al., 1994) and have been used as a Lunar International Standard Calibration Target (LISCT; Pieters et al., 2008). Additionally, the Apollo 16 area is an excellent test site for further calibration and deconvolution of complex highland

stratigraphy (Stöffler et al., 1985) and the presence of fresh craters of various sizes in this area provides contrasting material to investigate the effects of maturity on the photometric analyses.

2.3 Results

In this section, we first illustrate the validity of our methods and the reproducibility of derived Hapke parameters using the Apollo 17 photometric sequence and by examining results from photometric modeling in areas of local, symmetrical topographic variations (e.g., craters and hills). Below, we do not attempt to test the Hapke model; instead, we focus on relating modeled Hapke parameters to ground-truth observations with the goal of helping to improve understanding of how the photometric properties of the lunar regolith relate to the physical sample characteristics. Although it is not our intention to test the Hapke model, we note that the relationships developed in the subsequent sections are consistent with the physical interpretation of Hapke's photometric parameters.

2.3.1 Validation, Topography removal, and analysis of uncertainty

Validation and removal of topography:

The photometric processing of NAC images minimize the effects of topography on retrieval of single scattering albedo. Our implementation of the Hapke photometric model can be validated using repeat NAC observations at various illumination and viewing geometries (i.e., photometric sequences), with the assumption that the photometric parameters of the regolith should be independent of the photometric angles during observation. In other words, the single scattering albedo determined at $\delta=10^\circ$ (phase angle) should be the same as that determined at $\delta=60^\circ$. To assess the effectiveness of our photometric corrections, we have examined two areas in the TLV that are expected to have large topographic effects (i.e., areas of high slope), the slopes

of massifs and craters. For illustrative purpose, we selected Camelot Crater and Bear Mountain. Profiles were taken across each topographic feature to extract data for the elevation, slope, I/F, photometric angles, and single scattering albedo data.

A N-S transect across Camelot crater from four NAC images collected at different viewing and illumination geometries serves to illustrate how well the effects of topography and local illumination effects are minimized in the determination of single scattering albedo (Figure 2.9). For all of the NAC images, the detector view is near nadir ($<5^\circ$ emission angle for a flat surface). Our results indicate that the photometric model is capable of reproducing the single scattering albedo of the regolith for a range of incidence angles, but with some limitations. Areas of high slope, which can cause locally high incidence angles, tend to result in increased scatter in the data. Additionally, at higher incidence angles (>60 degrees) the single scattering albedo has a larger associated error, especially in areas that are partially shadowed. The same observations are apparent in the E-W transect across Camelot crater (Figure 2.10); however, Figure 2.10 more clearly conveys the difficulty of correcting for topography in areas of high slope, which are also areas of high local incidence and likely more immature surfaces.

Because Camelot crater is a small surface feature relative to the adjacent high-standing massifs, we chose to also examine transects across Bear Mountain. The topographic relief of Bear Mountain is on the order of several hundred meters, rather than the 10s of meters of Camelot crater. However, because Bear Mountain is a much larger surface feature, the changes in local slope are much more gradual (Figures 2.11 and 2.12). As with Camelot crater, the NAC images collected at lower incidence angles, and hence lower phase angles, appear to provide better results. Analysis of photometric modeling results indicates that our implementation of Hapke's photometric model does diminish or remove the effects of small-scale topography, with the limitation that slopes steep

enough to be immature are not necessarily well corrected. For example, when incidence exceeds ~ 60 degrees, the topographic effects are still apparent in the retrieval of albedo values, probably due to steep slopes and immature surfaces

Analysis of uncertainty:

The accuracy and precision of modeled Hapke parameters is important for any interpretation of variations in photometric properties, especially when it comes to the small surface area of each individual sampling site. For example, ω -values range between 0 and 1, therefore, if modeled values cannot be reproduced to within ~ 0.05 of the average, then the significance of our interpretations would be diminished. Photometric data were extracted from the processed NAC images in the photometric series for each sampling site, for which surface coverage exists. The variations in observed reflectance and modelled single scattering albedo were then examined as a function of changes in the phase angle. For example, data for the lunar roving vehicle Stop 9, sample 76121, demonstrates the variation in surface reflectance as a function of viewing geometry (e.g., phase angle), and highlights the increase in reflectance at lower phase angles (Figure 2.13). In photometric studies, it is typical to normalize reflectance data to a common phase angle or to a simple scattering model to make variations related to topography more subtle; Figure 2.13 illustrates this, where I/F values have been normalized to the Lommel-Seeliger function, i.e., reduced reflectance. Although normalization does reduce the overall variations observed, significant variations still exist in reduced reflectance that make comparison of images collected at different phase angles difficult. However, when the phase angle is plotted against the modelled single scattering albedo (Figure 2.13), minimal variations exist such that comparison of Hapke parameters is not hindered by viewing geometry; this is further evidence that suggests our approach adequately removes the effects of topography and local illumination angles. Moreover,

if we examine the scatter in the modelled single scattering albedo, we find that the average (0.20) has a 1σ at our threshold for usability (± 0.05).

In our dataset, local incidence and emission angles cover a broad range. We observed that filtering by local incidence and emission angles ($\leq 60^\circ$ incidence and $\leq 30^\circ$ emission) greatly improves the 1σ estimate. Although this filtering could be considered selectively filtering out data that weakens our conclusions, there are valid reasons as to why such filtering may be appropriate. The main reason is that reflectance data associated with high incidence and emission angles should be interpreted with caution, given that at these photometric angles, small objects cast large shadows. The angles associated with objects smaller than the DTM spatial resolution are averages of angles at smaller length scales, and may include shadows as well as highly reflective facets, and these effects on reflectance do not combine linearly. This situation reflects a limitation of the data and our method of modeling the single scattering albedo. Therefore, using the photometric series dataset and modelled single scattering albedo of each sampling site should be done with caution. Specifically, we propose that any interpretation or compositional calibration be done with filtered data.

2.3.2 Hapke parameter maps

Each NAC image was photometrically processed and then assembled into a regional ω -parameter map (Figure 2.14). Modelled ω -values range 0 to 1 and have been filtered according to the criteria described previously. Topographic effects are visually less apparent in the regional ω -parameter map than in the NAC reflectance (IoF) images. In general, highlands areas have among the highest ω -values (~ 0.35 to 0.40), indicating they are among the most reflective materials in the

TLV, whereas the mare basalts have much lower ω -values (average ~ 0.15 to 0.20). Only the areas immediately surrounding fresh impact craters have higher ω -values (~ 0.5 to 0.7).

A summary of the distribution of ω -values for specific geologic and geographic units within the TLV is given in Figure 2.15. As expected, the regolith associated with the TLV appears to be generally a 2-component mixture of feldspathic highlands and mare basalts; however, a more detailed investigation reveals important subtleties. For instance, mare basalt units have small variations in ω -values that are statistically different, indicating discrete photometric properties between spatially separated units (Figure 2.16). Moreover, the Sculptured Hills geologic unit shows variations in ω -values when comparing the unit as a whole (i.e., undifferentiated) vs. individual knobs (Figure 2.15). The single scattering albedo map highlights subtle variations in the photometric properties of various geologic and geographic units at Apollo 17 and can be used to understand what controls the photometric response of the regolith.

2.3.3 Compositional calibration

To examine the relationship(s) between the photometric properties and composition of lunar soils, we compared the mafic content of the soils to the ω -values extracted for each sample collection site. Below, we combine results from this study for Apollo 17 soils and 62231 Apollo 16 LISCT with previous photometric studies of the Moon (Clegg et al., 2014; Clegg-Watkins et al., 2016; Clegg-Watkins et al., 2017; Robinson & Jolliff, 2002; Sato et al., 2014). Additionally, we supplement our data with preliminary work on locales of “pure” anorthosite (Jolliff et al., 2018).

Photometric properties of Apollo 17 Soils

The ω -values determined for the locations at the Apollo 17 landing site where individual soil samples were collected are given in Table 2.3. Sample sites that occur within the photometric sequence coverage are also reported in Table 2.3 and are denoted by $n > 6$. In Table 2.4 we report the values from external data sources used for the remaining Apollo landing sites and pure lunar anorthosite soil (Clegg-Watkins et al., 2016; Clegg-Watkins et al., 2017; Schonwald et al., 2018). The SSA albedo of mature soils correlates inversely with the mafic content (i.e., more mafic compositions have lower ω -values; Figure 2.17). Mature soils are defined using the I_s/FeO values determined in the laboratory, where I_s is the intensity of the FMR signal for nanophase iron and FeO is the wt.% determined from bulk compositional analysis (Morris, 1978). We use only mature soils to establish the compositional relationship owing to the fact that the ejecta of fresh impact craters exhibit higher ω -values. This relationship is particularly true where fresh impact craters occur in compositionally uniform targets. Variations in the ω -values are attributed to the immature surfaces created as a result of the excavation of fresh material by the impact. This point becomes clear when the submature and immature soil samples are included in the data analysis, which results in more scatter in the data points. An important point regarding the submature and immature samples is that the additional scatter in the data does not seem to be random, but rather systematic. That is, more immature samples deviate farther from the trend than submature samples; this observation suggests that the influence of maturity on the SSA may be quantifiable.

Apollo 16 calibration target

To extend the compositional relationship developed in the previous section, NAC images covering the Apollo 16 LISCT were photometrically processed using the same methodology. A region corresponding to the calibration target was extracted and used to determine an average for

the site (Figure 2.8). The ω -value determined for the calibration target, 0.44 ± 0.02 , is consistent with the more feldspathic nature of Apollo 16 soils and most similar to the massifs at Apollo 17 (Table 2.4).

Apollo 17 compositional map

The compositional relationship established in this section was used to convert the filtered, regional ω -parameter map to mafic content (Figure 2.18). The compositional map has not been corrected for maturity and areas of exceptionally low mafic contents may in fact be fresh surfaces. Therefore, we used Kaguya Optical Maturity indices (e.g., Lemelin et al., 2016; Trang & Lucey, 2019) to filter the data by maturity and only included mature areas in our data analyses and interpretation, and recommend caution be taken when interpreting the compositional maps derived from the photometric data.

2.3.4 Maturity effects

Different surface maturities can cause variations in reflectance spectra, and this effect has been documented previously (Jolliff, 1999). Methods have been developed to estimate surface maturity from orbital datasets and these methods have proven valuable for investigating the range of lunar surface maturities (Fisher and Pieters 1994, 1996; Lucey et al., 1998, 2000). Similar methods for estimating maturity were developed for the Kaguya 60 mpp datasets (Lemelin et al., 2016; Trang & Lucey, 2019); however, no obvious relationship exists between such maturity indices and the I_s/FeO of individual samples. This lack of correlation may be a consequence of the complex geology and surface maturities at the Apollo 17 landing site, as well as the small surface area represented by the I_s/FeO values.

To investigate the variation in surface maturity at NAC scales, we examined the relationship between sample-derived maturity values (e.g., I_s/FeO) and the deviation of submature and immature samples from the mature soils compositional correlation developed in Figure 2.17; Figure 2.19 shows such deviations and the correspondence with I_s/FeO values, which displays a reasonably strong inverse correlation. For example, samples with low I_s/FeO values generally deviate farther from the mature soils compositional correlation (e.g., Figure 2.17b). Upon closer examination of ω vs. the mafic content, with respect to sample maturity, an apparent relationship exists that suggests variations in surface maturity at the Apollo 17 landing site may be reflected in the ~5 mpp NAC-derived Hapke parameter maps, which would suggest that both composition and surface maturity contribute to variations in single scattering albedo. Quantification of the “maturity effect” could be possible and means an empirical correction for surface maturity might also be possible. Further analysis is needed to test this working hypothesis; however, the preliminary results are promising. North and South Ray craters at Apollo 16 provide a means to test this hypothesis because they occur in a relatively homogenous feldspathic highlands terrain and include fresh impact crater ejecta, as well as more mature surface materials, which provide another exceptional ground-truth data set.

2.4 Discussion

The variation in the local geology in Taurus-Littrow Valley, as reflected in the ω -parameter and mafic-content maps, reflects the mixing relationship between mare and nonmare materials (e.g., Figures 2.14 and 2.15). That is, mixing between a feldspathic (highlands) and mafic component (mare materials). However, as demonstrated previously, maturity and glass content may also affect the photometric properties of the lunar surface. In the following sections, we

examine outstanding science questions related to the geology of the Taurus-Littrow Valley, and use these questions as further tests of our photometric analysis.

2.4.1 South Massif Light-Mantle Deposit(s) and Identification of Tycho Impact Melts

The light-mantle deposit located at the base of South Massif may have originated from the delivery of Tycho impact ejecta to the Apollo 17 landing site, triggering a debris flow (Figure 2.20; Lucchitta, 1977). Recently, Schmitt et al. (2017) and van der Bogert et al. (2019) proposed an alternative formation mechanism that invokes seismic shaking from the continued re-activation of the nearby Lee-Lincoln scarp. The South Massif light-mantle deposit and the two possible formation scenarios can be tested using photometric analyses.

We observed ω variations and geomorphic evidence that is consistent with a debris flow origin (Figures 2.21, 2.22, and 2.23); however, small variations in ω -values may support the interpretation of multiple debris flows that would not be consistent with an impact formation mechanism (Schmitt et al., 2017). Additionally, we identified low albedo materials that occur on the back slope of South Massif and near the summit; these materials have among the lowest single scattering albedos within the TLV and are most similar to Shorty Crater. The low-albedo materials that occur on the slope of South Massif exhibit an increase in single scattering albedo, which we hypothesize could be a result of mixing with local highland materials during mass wasting. A simple mixing calculation suggests that approximately 20% typical massif material could account for the increased single scattering albedo. Alternatively, fresh surfaces can cause an increase in w -values; therefore, we cannot discern whether the w -values are a consequence of mixing or immature surfaces resulting from mass wasting. We propose these low albedo materials are the result

of impact melt that lowers the regolith single scattering albedo owing to an increase in a glassy component.

To further investigate the Tycho impact origin of the light mantle deposit, additional sites of suspected Tycho impact materials were investigated (Figure 2.24 and 2.25). On the basis of photometric properties and photogeologic interpretations, we identified regions on massifs that are consistent with an impact melt origin (e.g., smooth regions of ponded melt with block-rich material at the margins indicating flow). Areas of suspected impact melt occur at the summit of neighboring massifs (e.g., Mons Vitruvius) and have albedo values similar to the low albedo material at the summit of South Massif. Moreover, the location of Tycho secondaries corresponds to the areas of low single scattering albedo.

The absence of debris flows at the location of Tycho secondary impacts (Figure 2.25) is consistent with the interpretation that while the delivery of Tycho impact materials may have aided in the formation of the light mantle deposit, it may not have been the sole contributor and that the proximity of the Lee-Lincoln scarp might have played a role. Additionally, our findings support current hypotheses and imply that the transport of impact melt across the lunar surface is pervasive. The interpretation of basin chronology based on impact glasses may be problematic, as such samples may have been transported from nearly any basin on the Moon. Additionally, our observations indicate that Tycho impact melts should be present in the Apollo 17 soils but would most likely be present in the soils at Station 2 because of mass wasting down the South Massif slope. Such mass wasting could have acted to concentrate Tycho impact material at the base South Massif and near Station 2 (Figure 2.20).

2.4.2 Ballistic Mixing of Lithologies on Massif Slopes

Compositional gradients observed at the contact between the valley floor and highland massifs are consistent with lateral transport of material by ballistic mixing. Previous studies have identified similar mixing profiles, albeit on a much broader scale (several kilometers; Li & Mustard, 2000; Mustard et al., 1998). Although mass wasting has clearly occurred, especially in areas of high slope, the effects likely cannot be distinguished from ballistic mixing unless there is enough compositional contrast between the mixing components and mixing substrate.

The linear mixing relationship expected between constituent end-members (mare floor and highland massifs) can be used to estimate the percentage of mare material contaminating highland soils. To quantify the extent of mixing, ω -values of 0.20 and 0.40 are used as representative of the valley floor basalts and massif soils, respectively. Approximately 10-20% mare material is expected near the base of the massifs, which is consistent with the percentages estimated from petrographic analyses at Stations 6 and 7, which were collected at base of North Massif (Heiken & McKay, 1974; Muehlberger et al., 1973).

2.4.3 Pyroclastic Deposits at Apollo 17

On the basis of photometric properties, we identified an extensive pyroclastic deposit to the Northwest of Family Mountain that corresponds to an area of low single scattering albedo (Figure 2.14) and increased mafic content (Figure 2.18). The existence of a regional pyroclastic deposit at Apollo 17 is well known due to the abundance of pyroclastic beads documented in the soils collected at the landing site (Adams et al., 1974; Heiken & McKay, 1974; Muehlberger et al., 1973). The regional pyroclastic glass deposits that have been observed to the northwest of Apollo 17 are more easily identifiable in the mafic content map. While this could reflect the high mafic

contents of the unit, it may also be exaggerated by the abundance of glass beads in the soil. As noted by Clegg-Watkins et al. (2017), high glass contents tend to decrease the single scattering albedo of the soils. Indeed, we see a subtle link between soils that contain abundant pyroclastic glasses and soils that plot below the trend for mature soils (e.g., Figures 2.17b and 2.19). Composition is the dominant control on the single scattering albedo of the lunar regolith; however, fresh surfaces and areas of high glass content (i.e., pyroclastic deposits) affect the photometric response to a certain extent. This weak observation may indicate that the single scattering albedo of the lunar regolith is mainly controlled by composition and maturity, but the glass may play a secondary role. Therefore, our photometric processing method could allow for the identification of previously unidentified pyroclastic deposits, such as might be expected at the sites of the Marian Domes and Compton-Belkovich silicic volcanism (Wilson et al., 2015), though further analysis is needed.

2.5 Summary and Conclusions

Apollo 17 landing site and the Apollo 16 LISCT were used to examine the relationship between regolith composition and the photometric response of the surface using Apollo 16 and 17 soils as ground-truth calibration. A regional Hapke parameter map of the Taurus-Littrow Valley was produced to examine the variation in photometric properties at the Apollo 17 landing site. The single scattering albedo of the lunar regolith is strongly controlled by composition but is also influenced by the physical properties of the soil (i.e., maturity and glass content). The single scattering albedo of the lunar regolith is inversely related to the mafic composition of the soils and this relationship was exploited to develop a regional mafic content map of the Apollo 17 landing site. Lastly, we used the photometric relationship to examine the local geology of the Taurus-Littrow Valley.

Our observations suggest that while the delivery of Tycho impact materials may play a role in formation of the light mantle deposit, the proximity of the Lee-Lincoln scarp was likely also a contributing factor. The identification and characterization of putative Tycho impact melt material implies that the transport of impact melt across the lunar surface is pervasive. Therefore, the interpretation of impact chronology based on impact glasses may be problematic, as such samples may have been transported from many possible large craters on the Moon. Additionally, our observations indicate that Tycho impact melts should be present in the Station 2 Apollo 17 soils due to concentration during mass wasting.

Figures

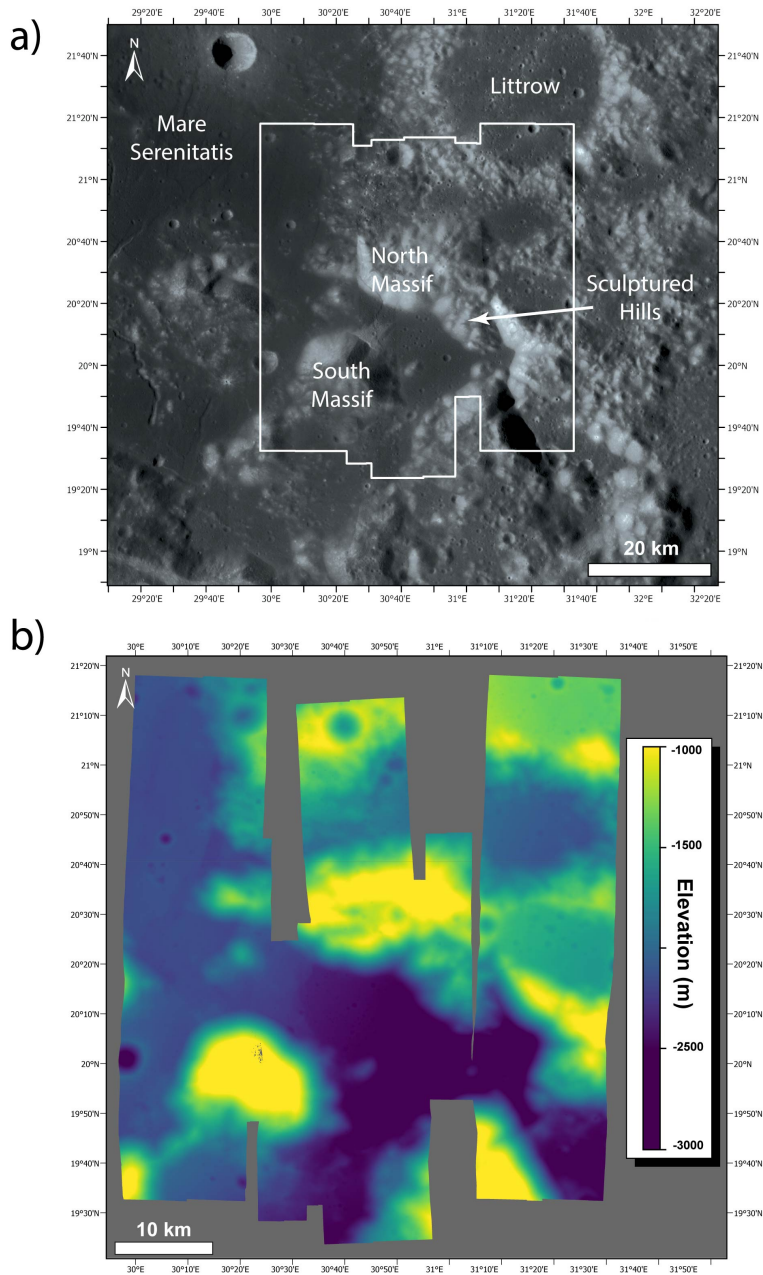


Figure 2.1. a) Taurus Littrow Valley, WAC global mosaic [image credit: NASA/GSFC/ASU]. Key surface features are annotated, and the boundary for the NAC regional mosaic and DTM is indicated by the white polygon. B) Regional 5 mpp DTM of the Taurus-Littrow Valley.

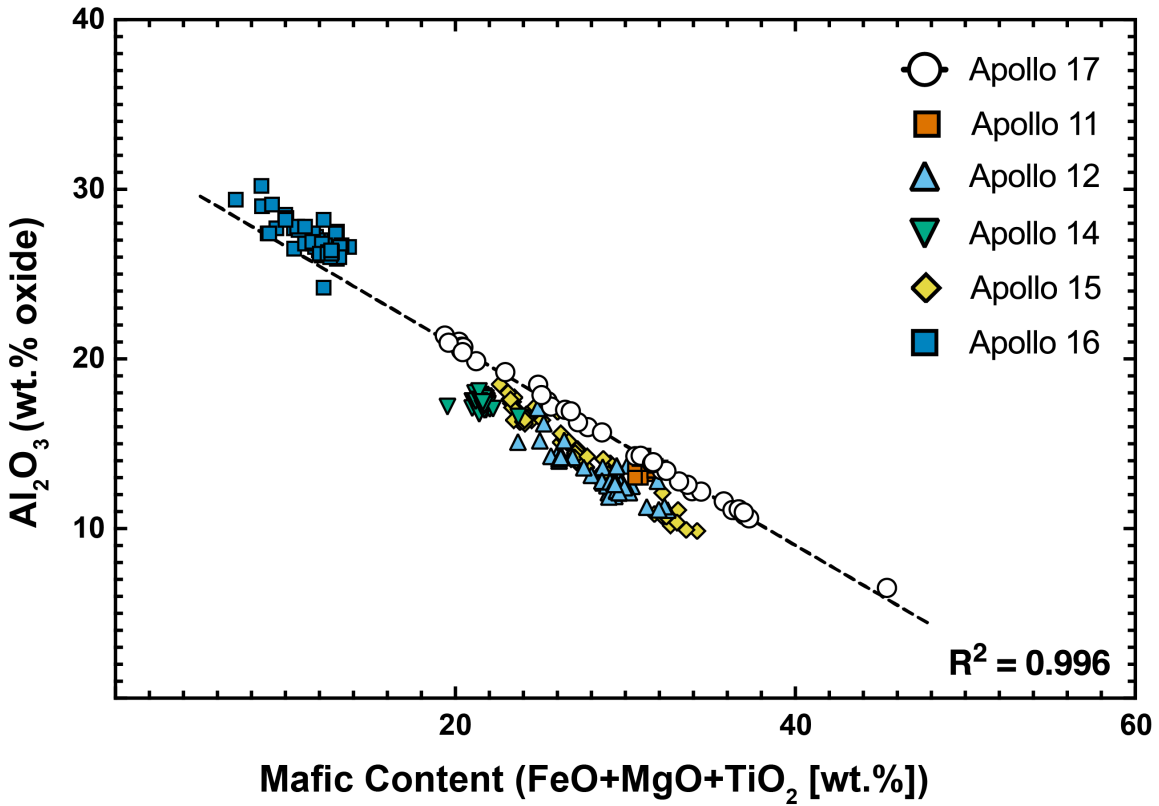


Figure 2.2. Variation diagram of Al₂O₃ vs. mafic content (FeO+MgO+TiO₂) for soils collected during the Apollo missions. The soils collected during Apollo 17 exhibit a wide range of compositions, and the soils form a strong, inverse linear association between the mafic component (high MgO+FeO+TiO₂) and feldspathic component (high Al₂O₃). The relationship shown essentially represents a two-component mixture between mare basalts and highlands material. The compositional range and near perfect linear correlation exhibited by the Apollo 17 soils make Apollo 17 an ideal site for a photometric investigation.

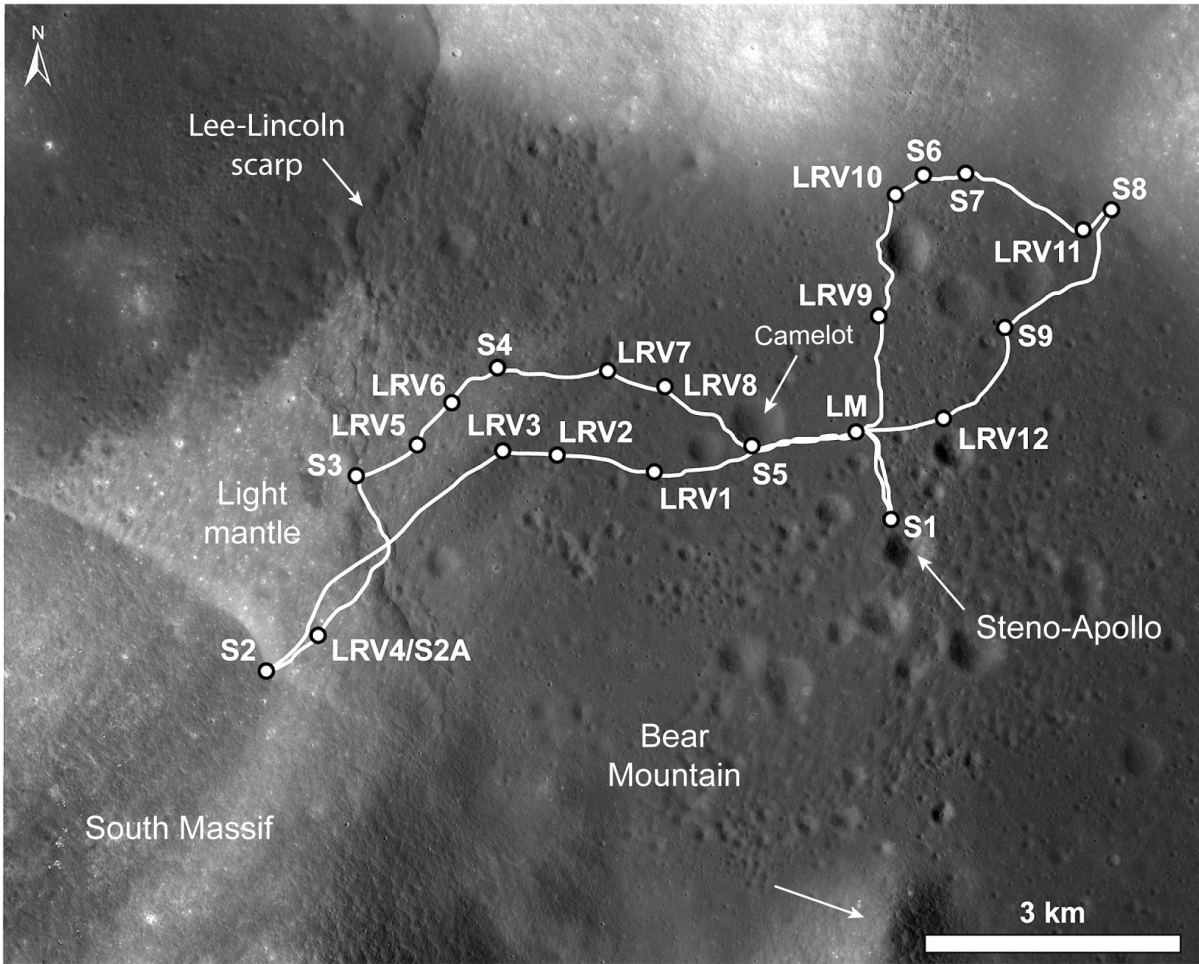


Figure 2.3. Location of Apollo 17 sample stations and Lunar Roving Vehicle (LRV) traverses. Sample station and traverse locations from Haase et al. (2019). Base map shown is the LROC NAC-based, controlled orthomosaic for the Apollo 17 landing site (Haase et al. 2019).

Apollo 17 Photometric Series

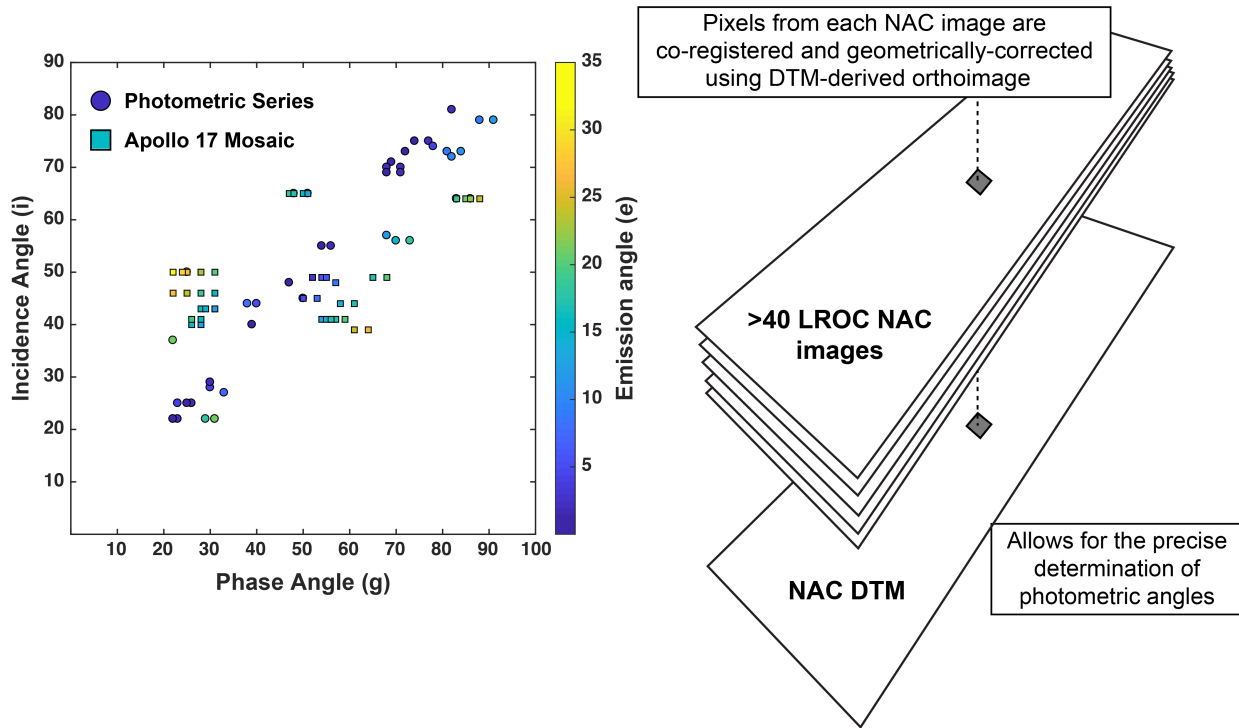


Figure 2.4. (*left*) Scatter plot showing the photometric angles (phase, incidence, and emission) of NAC images used to construct the Apollo 17 regional mosaic (squares) and photometric series (circles). Data points are colored by the emission angle. Images that fall near the 1:1 shown are near-nadir images, while those that lie to left and right of the 1:1 line have viewing and illumination geometries that are back scattering and forward scattering, respectively. The NAC images that comprise the photometric series span a greater range in phase angle and are mainly near-nadir images. Therefore, the photometric series at Apollo 17 can be used to investigate the dependence of surface reflectance on the viewing and illumination conditions and characterize the photometric properties of the regolith. (*right*) Schematic showing the data structure of the Apollo 17 photometric series. Each NAC image in the photometric sequence is geometrically corrected and co-registered to a single NAC DTM, which allow the precise determination of photometric angles.

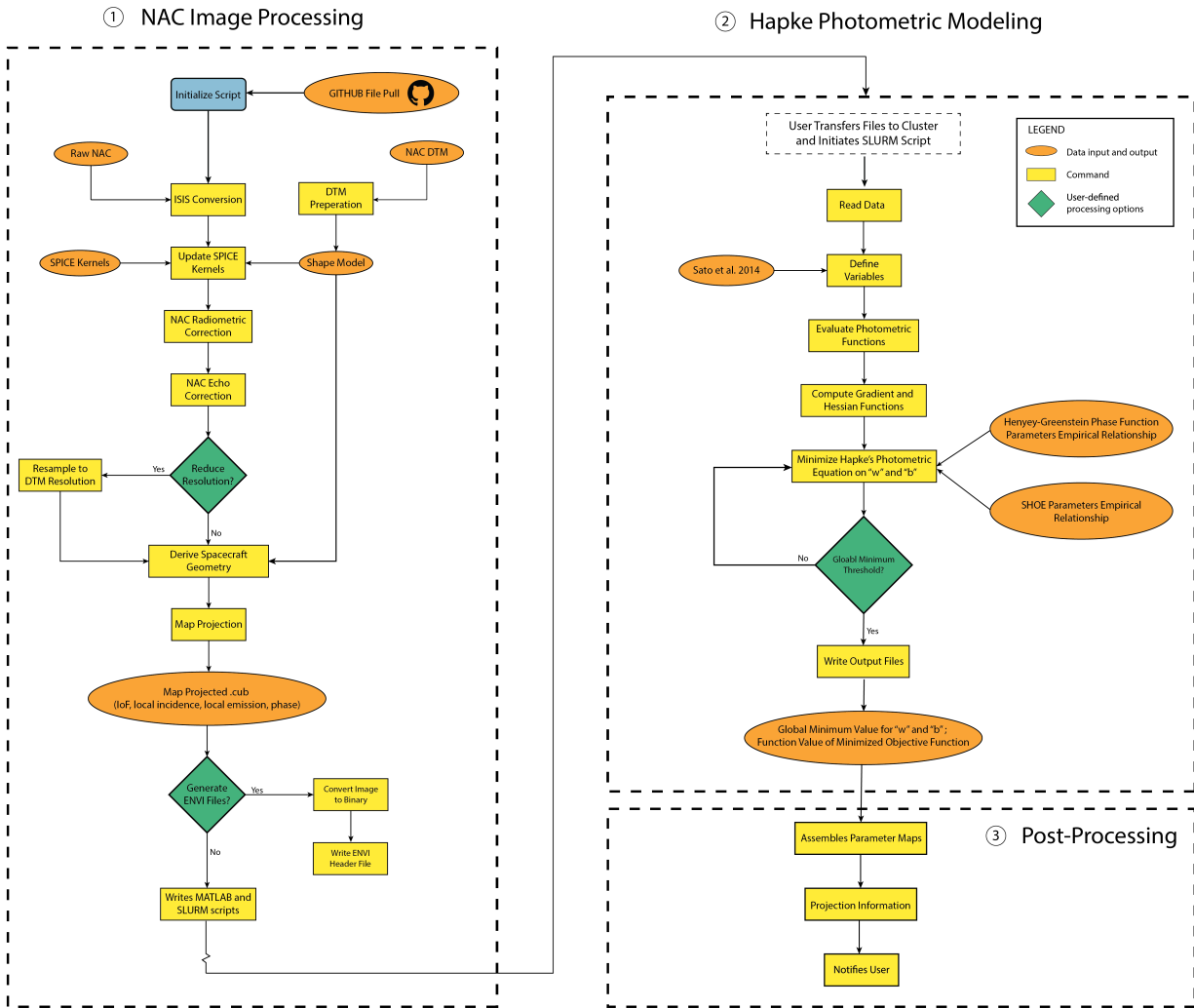


Figure 2.5. Photometric processing routine for NAC images and DTMs. The processing is divided into three discrete steps: 1) NAC pre-processing; 2) Hapke photometric modeling; and 3) post-processing.

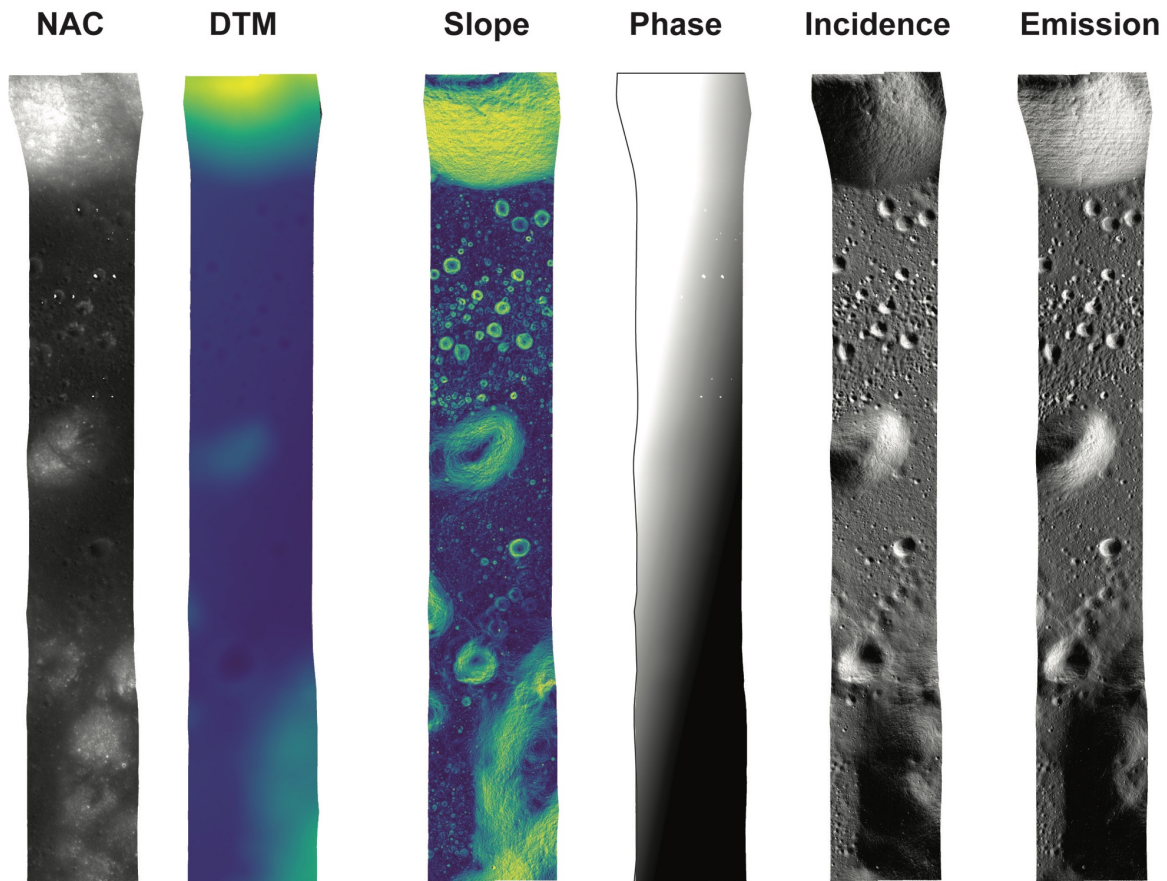


Figure 2.6. Input datasets produced during pre-processing and required to photometrically process NAC images. The NAC DTMs are used as shape models, in conjunction with spacecraft pointing data, to calculate the phase, local incidence, and local emission. The use of high-resolution NAC DTMs to determine photometric angles represents a significant improvement over previous methods that assume a spherical Moon and uses small-scale topographic variations to compute slopes and local illumination geometry at the NAC DTM scale.

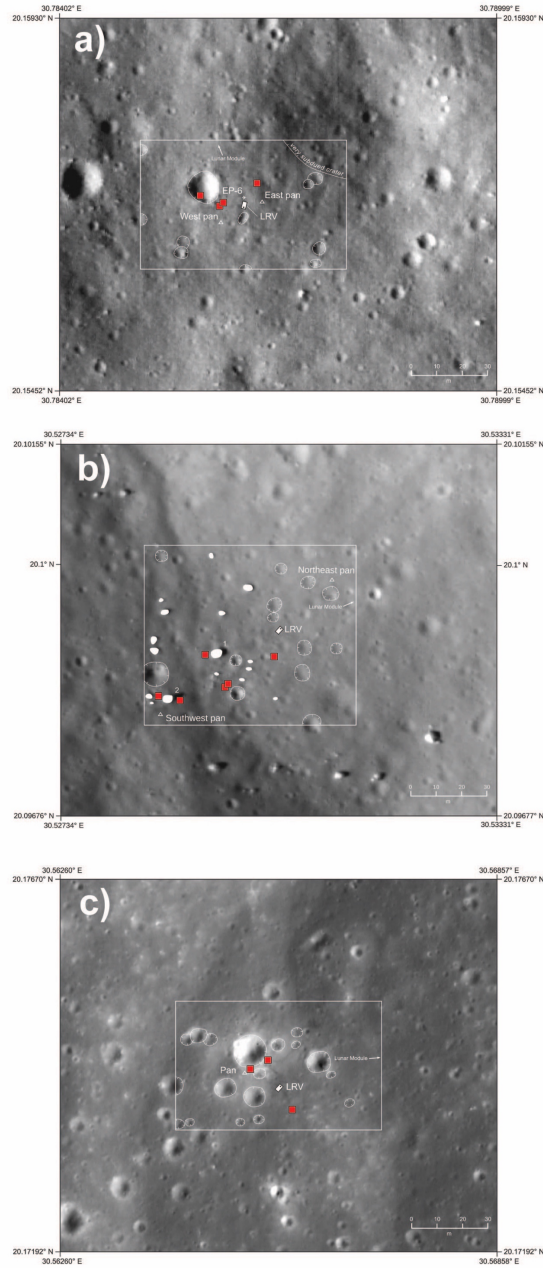


Figure 2.7. a-i) Detailed locations of individual sampling sites at sample stations 1-9, respectively. Base image and location of surface features from Haase et al. (2019). The locations of individual samples were determined using Apollo era Hasselblad surface imagery, Apollo 17 transcripts, sample locations from the preliminary Apollo 17 science report (Muehlberger et al., 1973), and recent cartographic analysis by Haase et al. (2019). The use of individual soil samples from each station, rather than an average from each station, increases the number of ground-truth observations available and permits a more rigorous photometric investigation.

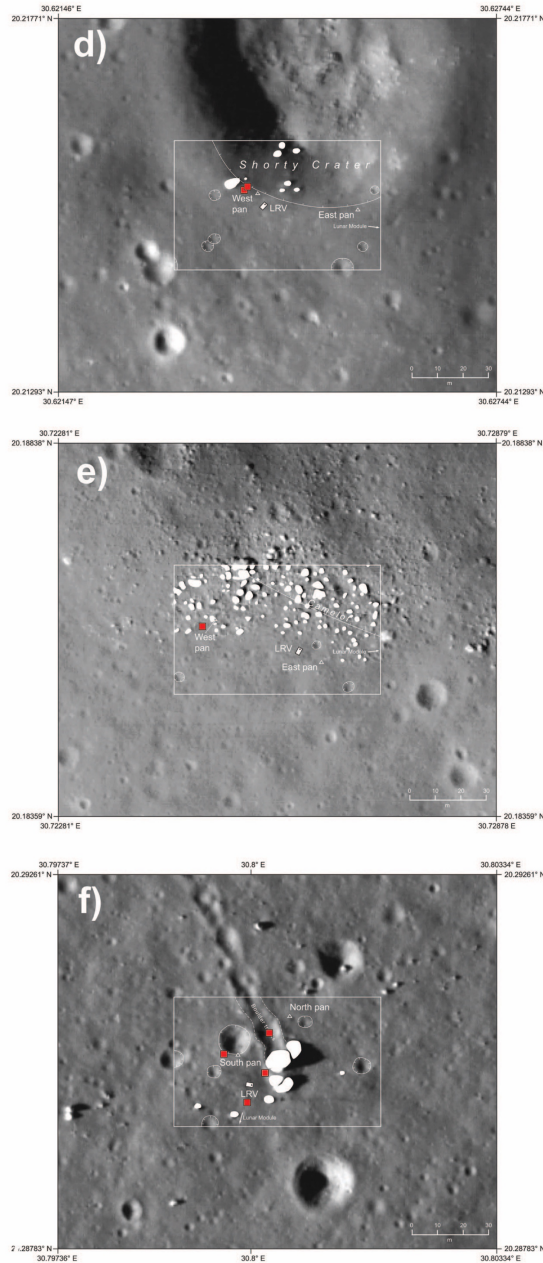


Figure 2.7 (continued). a-i) Detailed locations of individual sampling sites at sample stations 1-9, respectively. Base image and location of surface features from Haase et al. (2019). The locations of individual samples were determined using Apollo era Hasselblad surface imagery, Apollo 17 transcripts, sample locations from the preliminary Apollo 17 science report (Muehlberger et al., 1973), and recent cartographic analysis by Haase et al. (2019). The use of individual soil samples from each station, rather than an average from each station, increases the number of ground-truth observations available and permits a more rigorous photometric investigation.

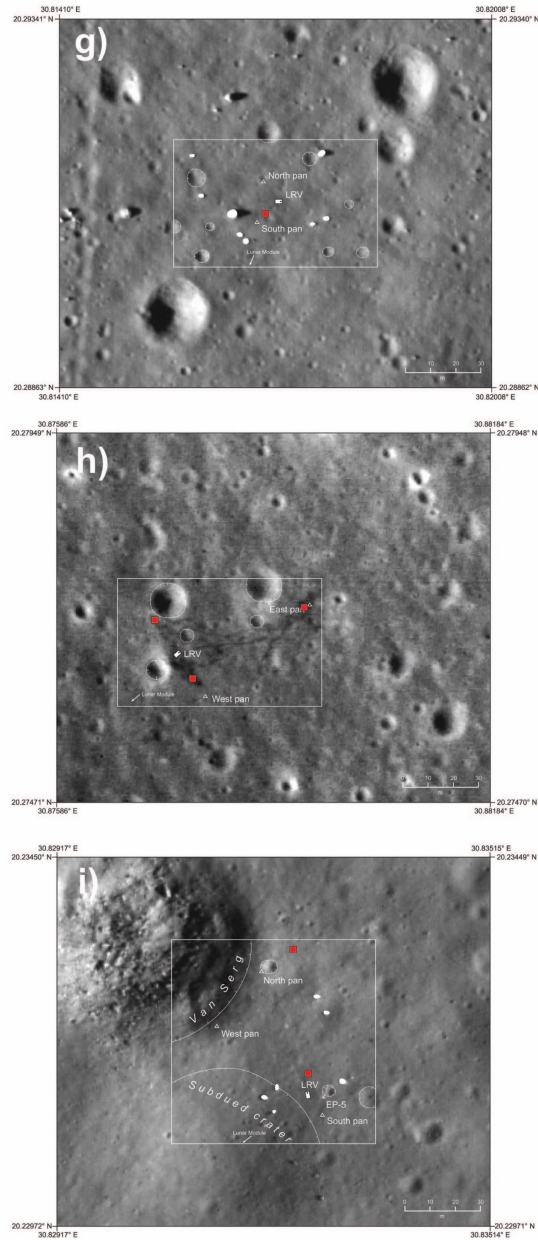


Figure 2.7 (continued). a-i) Detailed locations of individual sampling sites at sample stations 1-9, respectively. Base image and location of surface features from Haase et al. (2019). The locations of individual samples were determined using Apollo era Hasselblad surface imagery, Apollo 17 transcripts, sample locations from the preliminary Apollo 17 science report (Muehlberger et al., 1973), and recent cartographic analysis by Haase et al. (2019). The use of individual soil samples from each station, rather than an average from each station, increases the number of ground-truth observations available and permits a more rigorous photometric investigation.

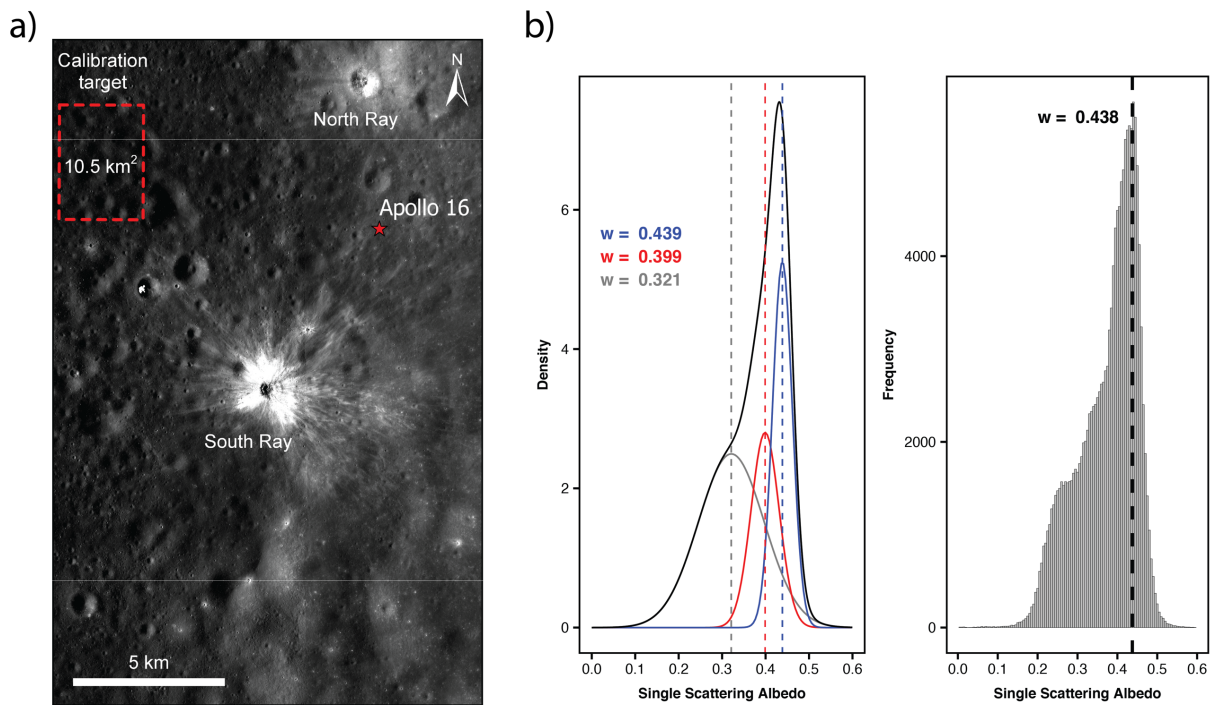


Figure 2.8. Apollo 16 Lunar International Standard Calibration Target (LISCT) used to expand the compositional range of samples investigated. a) Apollo 16 NAC regional mosaic showing the approximate location of the calibration target (dashed, red polygon), which occurs in an area of undisturbed, mature highland soil. Soil sample 62231 is considered representative of the calibration target, has been extensively characterized, and is commonly used for spectral calibration (e.g., Blewett et al., 1997; Pieters et al., 2008; Taylor et al., 2010). b) Probability density and frequency distribution plots for the single scattering albedo determined for the calibration target. A 3-component, mixture-based gaussian peak distribution was used to determine an average single scattering albedo for the calibration target of ~ 0.44 .

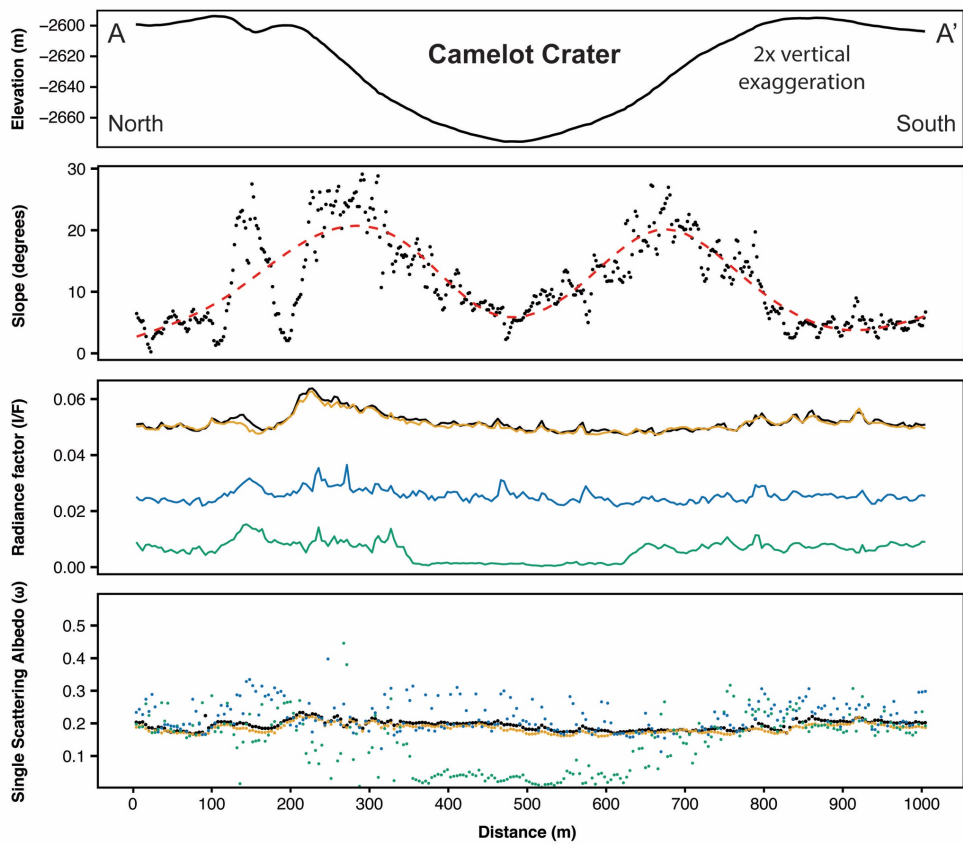
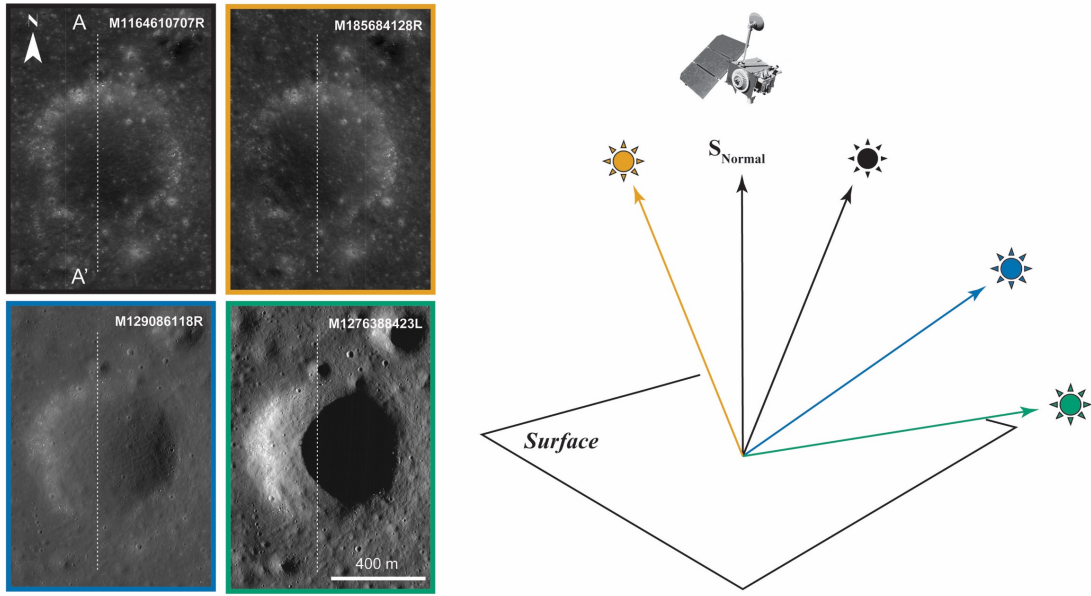


Figure 2.9. N-S transect across Camelot crater illustrating the variation in surface reflectance as a function of illumination and viewing geometry, the importance of incidence angle in photometric studies, and the

ability of our methodology to correct for local topographic variations. (top left) Four, near-nadir NAC images are shown with: 1) opposite sun direction (i.e., east vs. west), but similar incidence angles and 2) consistent sun direction, but variable incidence angles. The NAC images with higher incidence angles exhibit lower reflectance values, relative to a normally illuminated surface. The variation in apparent surface reflectance between the images highlights the difficulty when comparing NAC images collected with differing illumination and viewing conditions. However, ω -values display more limited variations, suggesting ω -values determined using our methodology can be used for image comparisons. Locally, ω -values can deviate from the average; however, our observations indicate these are likely either the result 1) surface features with different photometric properties (e.g., fresh surfaces) or 2) areas heavily shadowed due to high incidence angles. For example, at high incidence angles even small boulders (~a few meters) can cast large shadows, which are difficult to correct for. Additionally, we note that areas of high slope ($>20^\circ$) often correspond to a broader range in ω -values, suggesting that some effects from topography remain; however, as discussed in the text, these may in fact be the result of more immature surfaces that develop on areas of high slope.

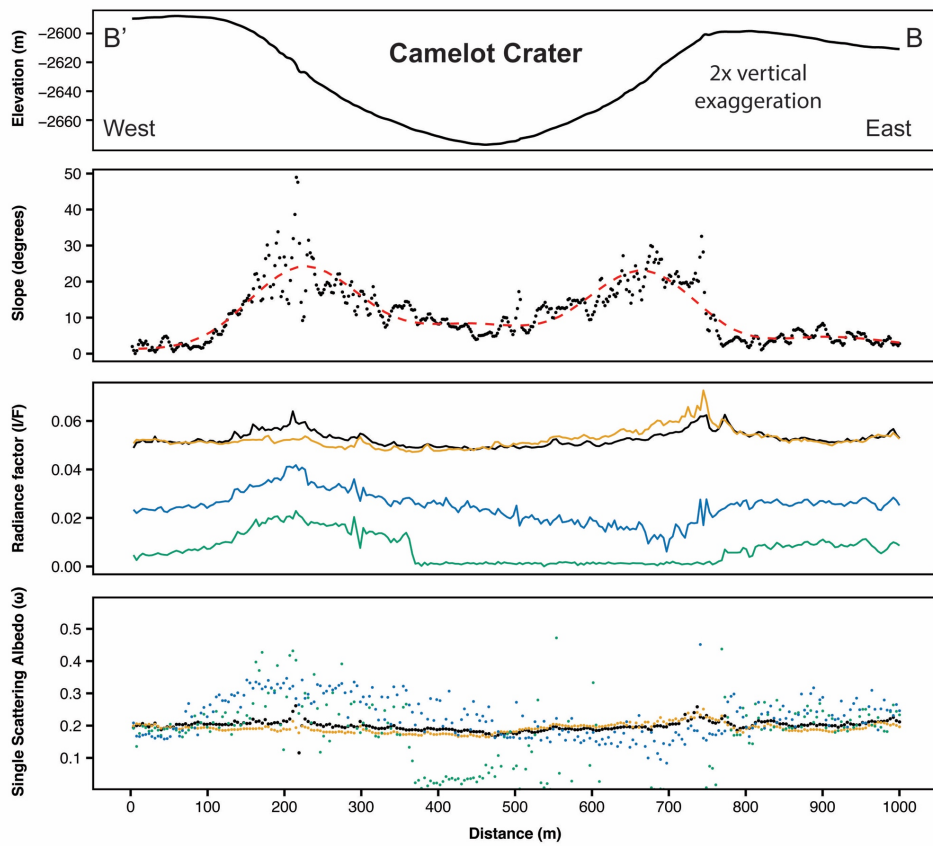
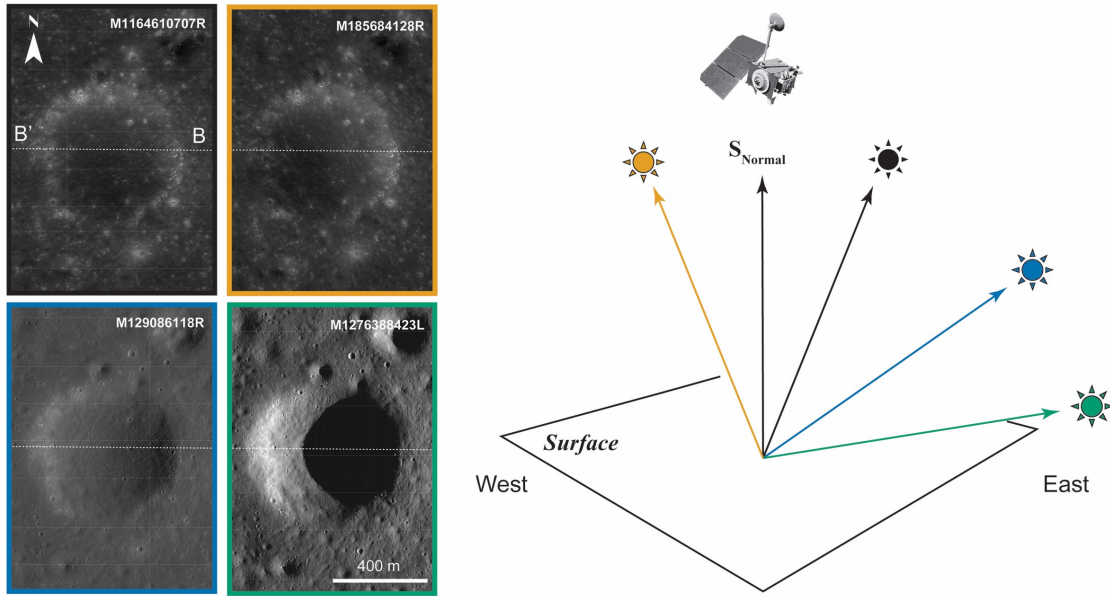


Figure 2.10. E-W transect across Camelot crater illustrating the variation in surface reflectance as a function of illumination and viewing geometry, the importance of incidence angle in photometric studies, and the

ability of our methodology to correct for local topographic variations. (top left) Four, near-nadir NAC images are the same as shown in Figure 9. The E-W transect shown here highlights the effects of slope and local incidence on the derived ω -values. For example, in the high incidence NAC the western wall of Camelot crater appears to exhibit higher ω -values, relative to the surrounding terrain; however, the actual ω -values are likely lower, and the higher values probably result from the near normal illumination geometry (i.e., low, near zero, incidence angles). This is only apparent in the E-W transect due to the direction of the Sun, relative to the walls of Camelot crater.

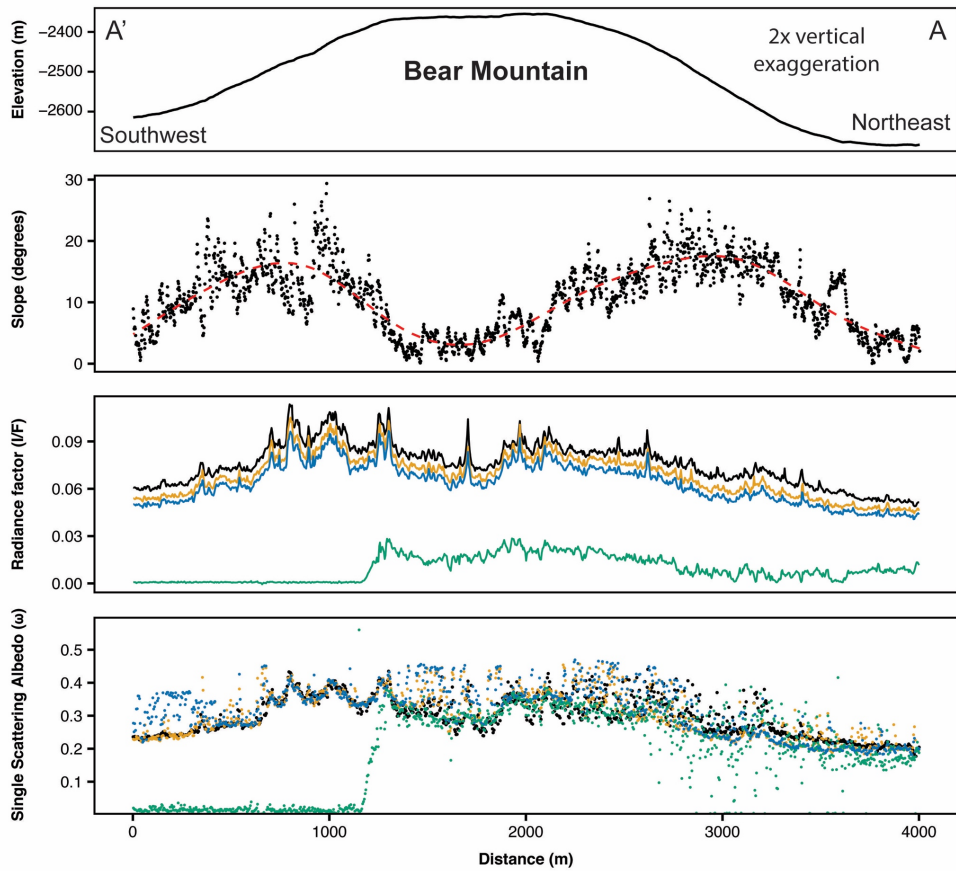
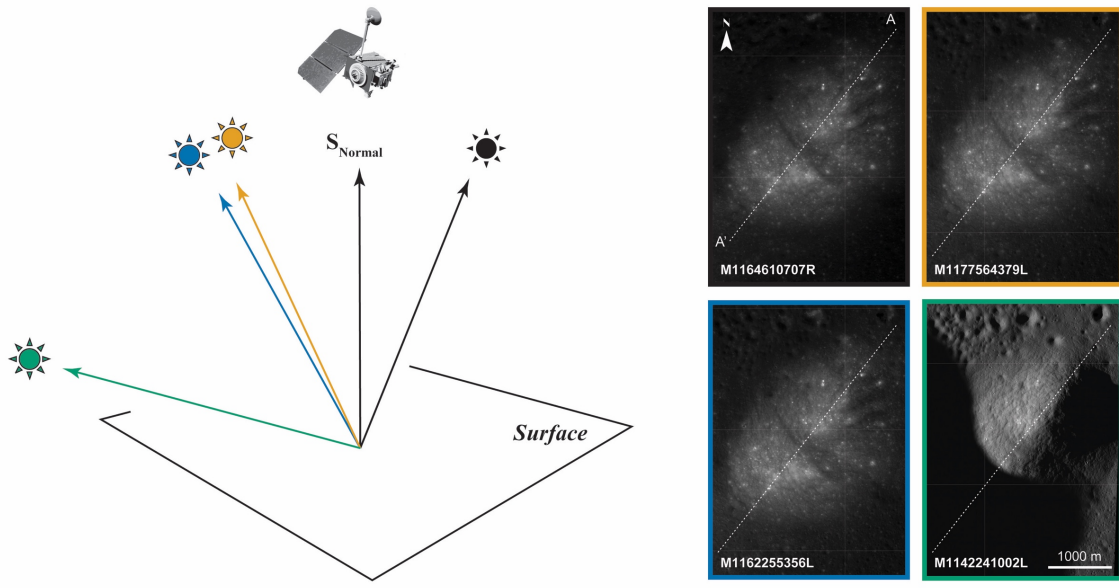


Figure 2.11. NE-SW transect across Bear Mountain illustrating the ability of our methodology to correct for large-scale topographic features (e.g., massifs). (top right) Four, near-nadir NAC images of Bear

Mountain are shown with: 1) opposite sun direction (i.e., east vs. west), but similar incidence angles and 2) consistent sun direction, but variable incidence angles. The NAC images with higher incidence angles exhibit lower reflectance values, relative to a normally illuminated surface. Again, the calculated ω -values show the least amount of variability among the NACs collected at lower incidence angles; however, even at higher incidence the photometric model appears to do a sufficient job at removing the effects of topography and local illumination, especially in areas of low slope (e.g., the crest of Bear Mountain).

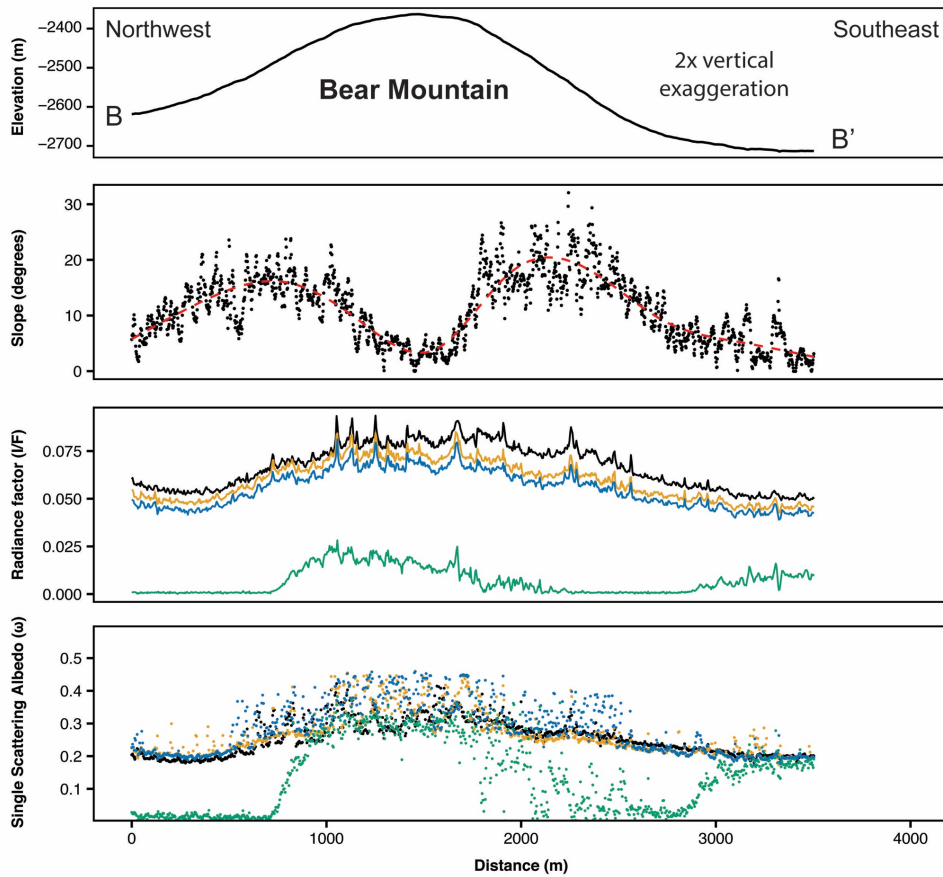
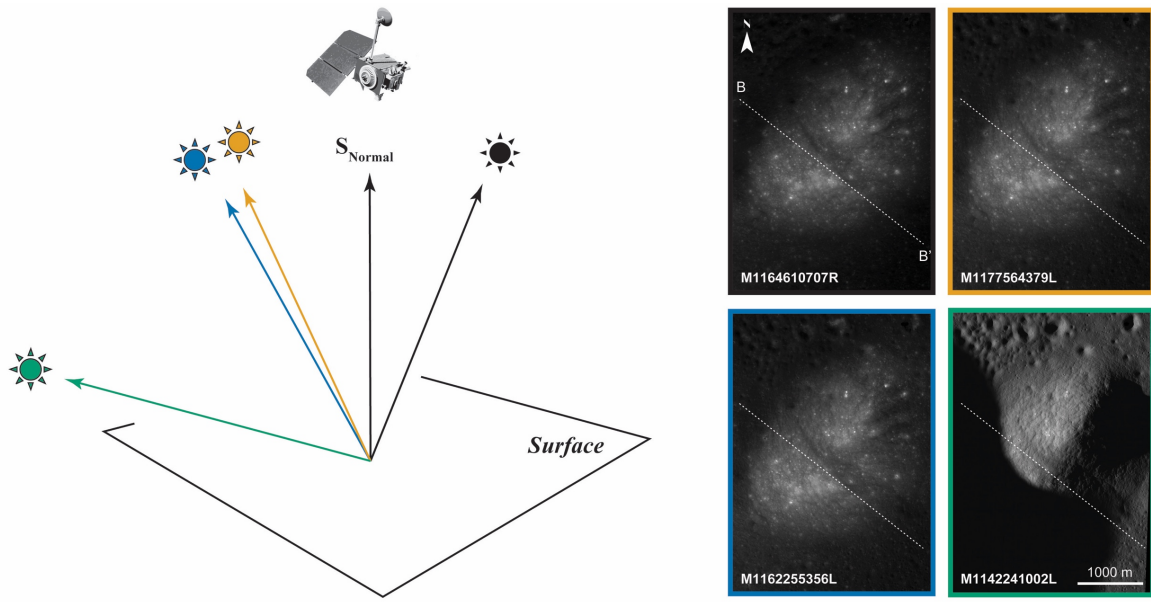


Figure 2.12. NW-SE transect across Bear Mountain illustrating the ability of our methodology to correct for large-scale topographic features (e.g., massifs). (top right) Four, near-nadir NAC images of Bear

Mountain are shown with: 1) opposite sun direction (i.e., east vs. west), but similar incidence angles and 2) consistent sun direction, but variable incidence angles. The NAC images with higher incidence angles exhibit lower reflectance values, relative to a normally illuminated surface.

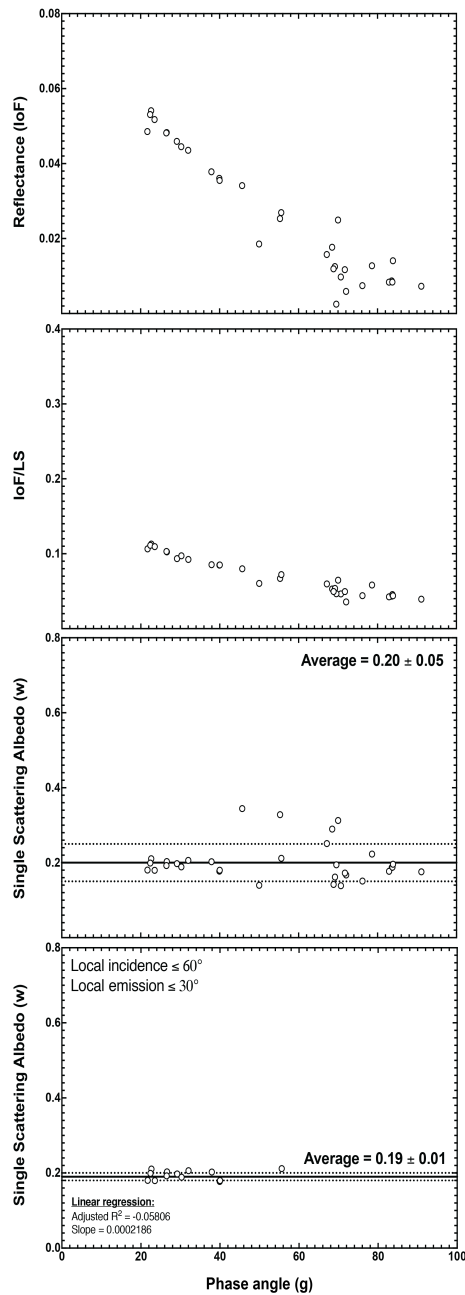


Figure 2.13. Effects of viewing and illumination geometry (phase angle) on the apparent surface reflectance and single scattering albedo, using LRV Stop 9 as an example. Data shown here were extracted from the photometric series at Apollo 17; therefore, each data point corresponds to quantities for sampling location of LRV Stop 9, in each co-registered NAC image that was collected under differing photometric angles. a) Plot of reflectance vs. phase angle (g). At lower phase angles the apparent reflectance values that would be determined for the sample is much higher due to increased brightness resulting from opposition surge. b)

Plot of reflectance normalized to a simple scattering model (Lommel-Seeliger) vs. phase angle. This approach is commonly taken in an attempt to reduce the effects of topography when comparing NAC images. Although normalization to the Lommel-Seeliger function does reduce the overall variation in reduced reflectance (IoF/LS), an increase at low phase angles is still evident. c) Plot of ω -values determined for each NAC image vs. phase angle. The average albedo value determined for LRV Stop 9 is $\sim 0.20 \pm 0.05$ 1σ . If the data are filtered by local incidence and emission angle, the 1σ error is decrease by a factor of 5, with a near-zero slope. This observation indicates that the photometric model and implementation described in this paper adequately corrects for topography, with a precision suitable for testing detailed science hypotheses. We note, however, that filtering the data provides the best data for interpretation. Our approach to filtering the data is justified; we have already demonstrated that high local incidence angles result in small objects causing large shadows for which the photometric model cannot sufficiently correct.

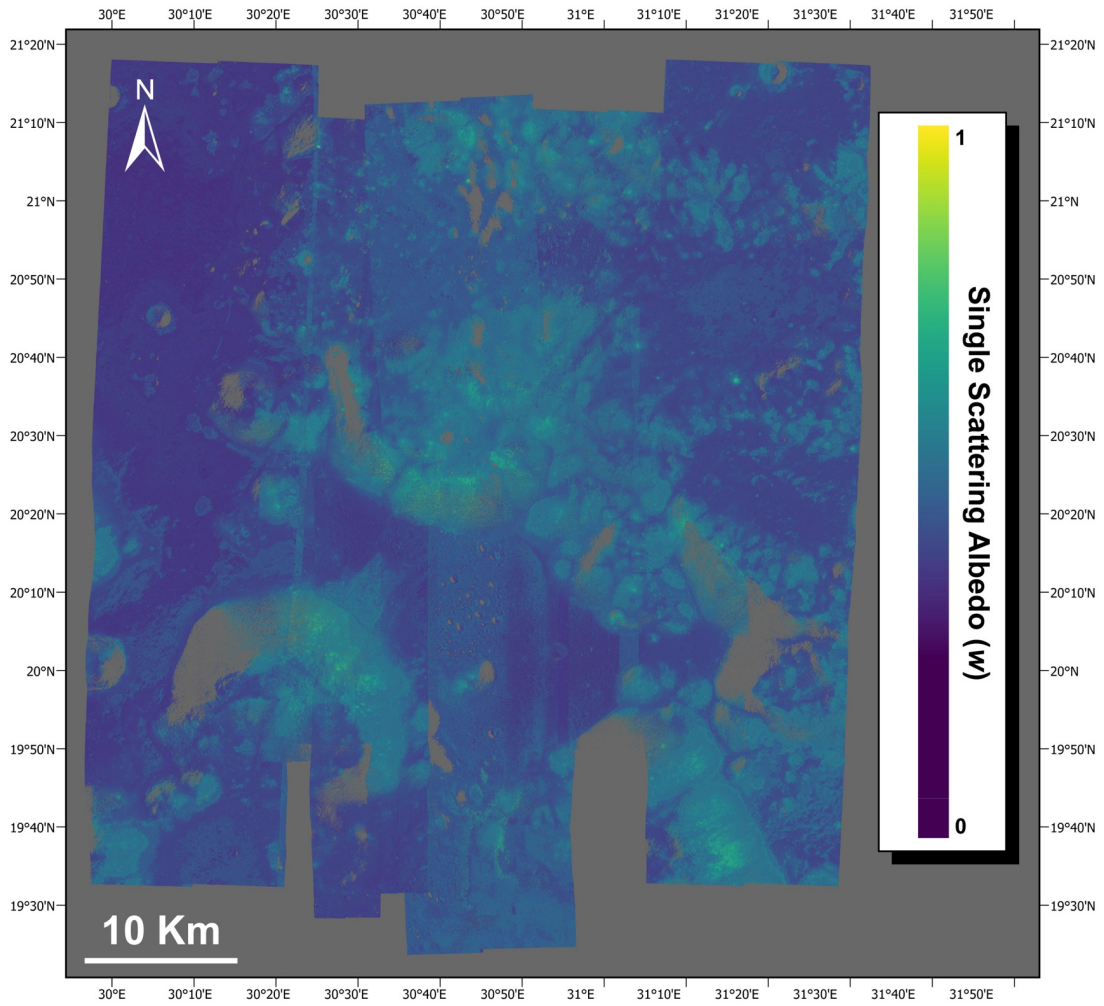


Figure 2.14. Regional scale single scattering albedo map of the valley of Taurus-Littrow. The highlands terrain and surrounding massifs have ω -values that are higher than the mare basalts.

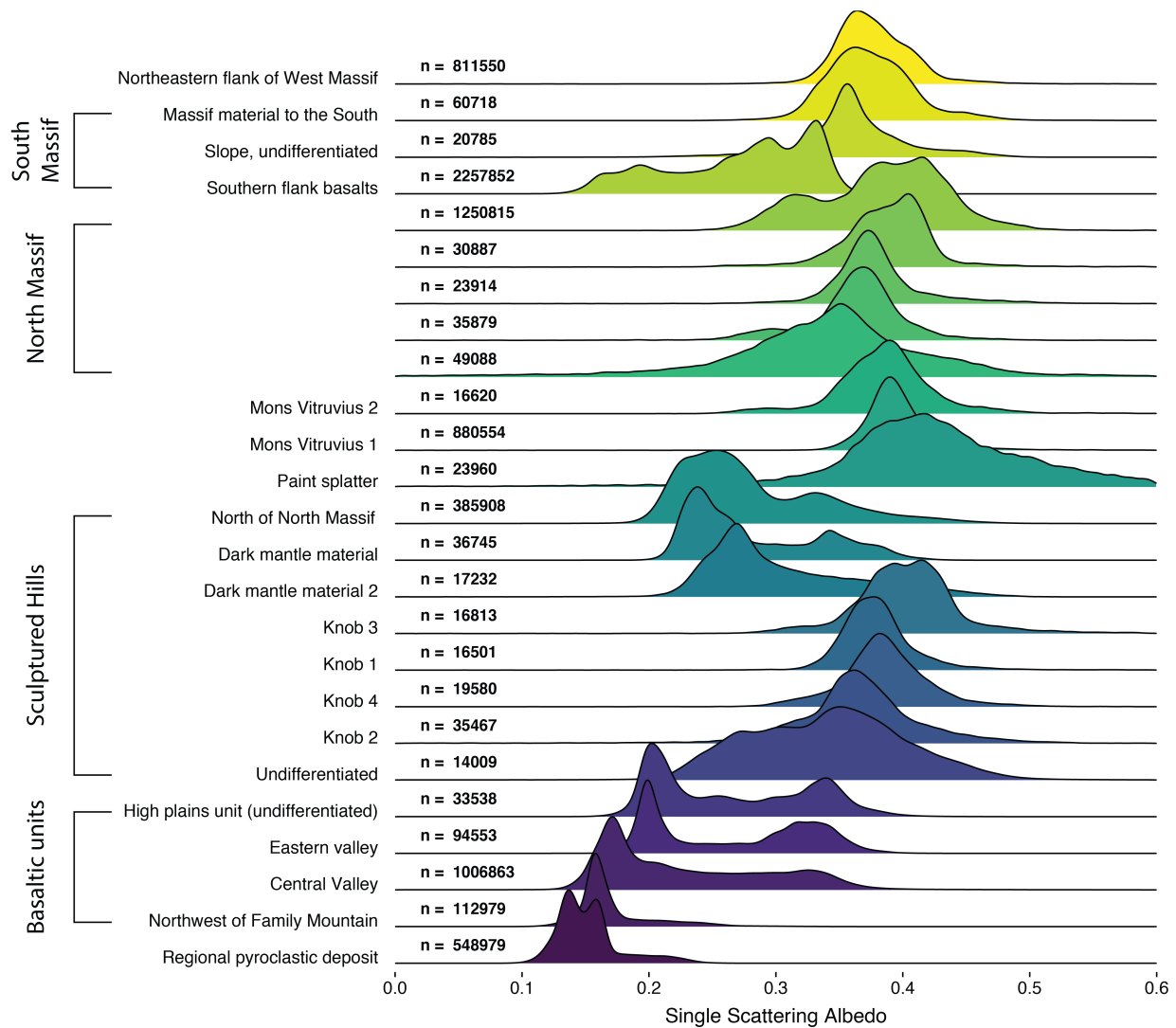


Figure 2.15. Probability density plot of select regions of interest within the TLV. Different surface units display a wide range of ω -values, ranging for ~ 0.17 for the Mare basalts to ~ 0.38 for highland terrains, as well as even higher of ω -values surrounding fresh impact craters (~ 0.5 to 0.7). Additionally, the ROIs also vary in terms of the within unit distributions. For example, the basalts that occur to the Northwest of Family Mountain display a unimodal distribution, with a prominent peak at ~ 0.15 , while the basaltic material that occurs within the high plains units has a bimodal distribution with a prominent peak at ~ 0.20 corresponding to a basaltic component and a more subdued peak at ~ 0.34 . The less prominent peak at ~ 0.34 suggests the presence of a highland component, which is intuitive given that the high plains unit occurs within the feldspathic highlands terrane.

Apollo 17 Basalts (scaled density)

Legend (Basalts) ■ Central Valley ■ Eastern Valley ■ Northwest of Family M

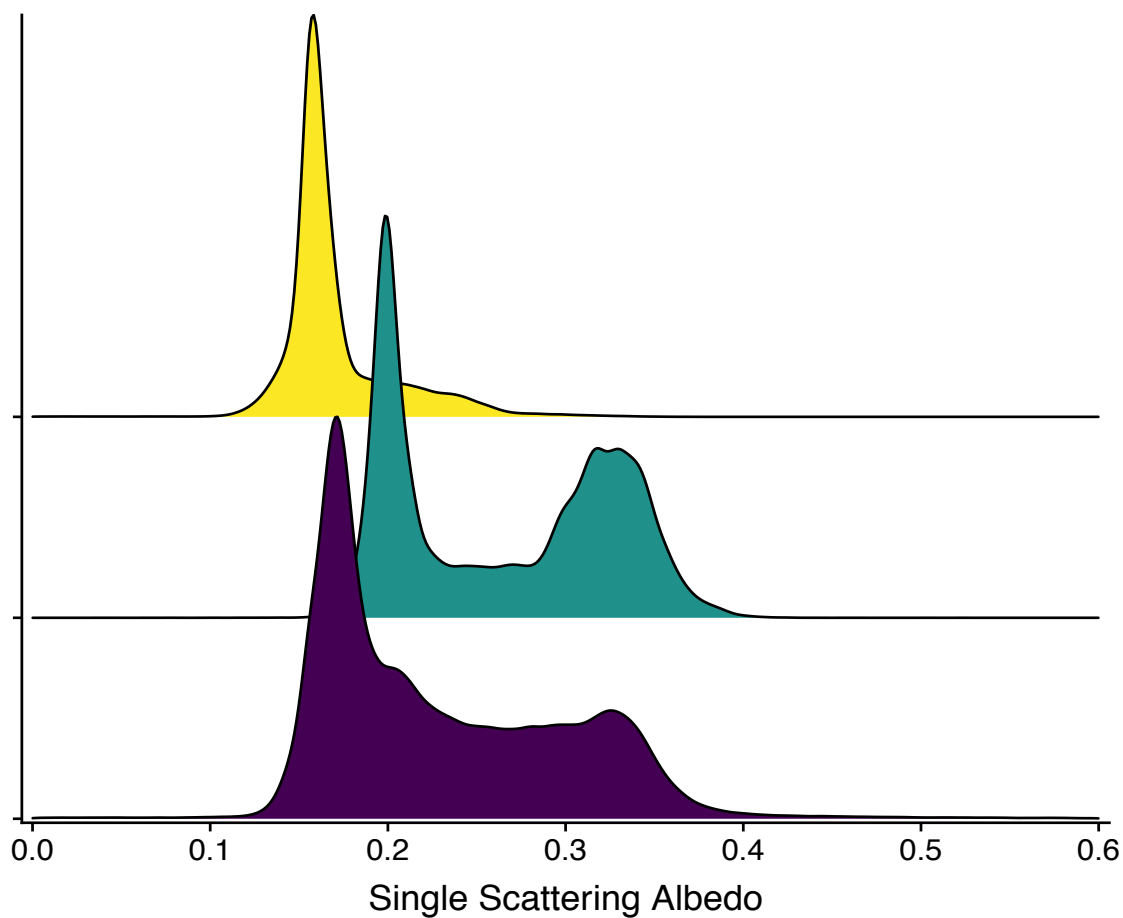


Figure 2.16. Variations in the single scattering albedo of three mare basalt regions. The basalts that occur to the northwest of Family Mountain exhibit a strong, single peak in the single scattering albedo values, whereas the eastern valley basalts exhibit a bimodal distribution that likely results from an increase in the proportion of adjacent massif material.

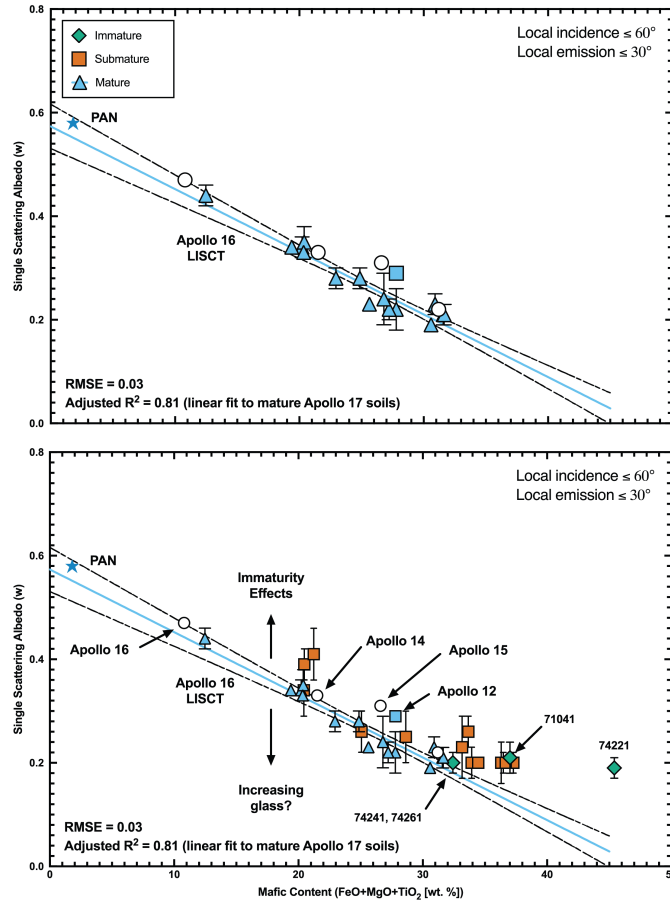


Figure 2.17. Compositional correlation between the mafic content of Apollo 17 soils and the calculated ω -values determined for each sample. Data for individual Apollo 17 soils are shown as black circles. To extend the dataset to more feldspathic compositions, the average ω -value determined for the Apollo 16 LISCT is shown, as well as preliminary results from our ongoing analysis of site of pure anorthosite. Additionally, ω -values determined previously for the areas surrounding the lunar modules at each Apollo site were included for completeness (e.g., Clegg et al., 2014). Compositional data are from a variety of sources and were compiled by Korotev et al. a) A strong, inverse correlation is evident between the mature soils; maturity is defined using the samples and is given as I_S/FeO , where I_S is the intensity of the FMR signal and FeO is the weight percent iron in the sample. The relationship observed indicates the photometric properties (i.e., single scattering albedo) of the lunar regolith are strongly dependent upon composition, as expected. Additionally, this relationship can now be used to investigate the regolith composition at science targets that have not yet been sampled in-situ. b) Plot of mafic content vs. SSA, where the data for Apollo 17 soils now include mature, as well as submature and immature soils. When the less mature soils are included in the regression, the strength of the correlation decreases because the samples exhibit a much wider range in average ω -values for a given composition; we propose that the variations observed are directly related to the maturity of the surface and that immature surfaces tend to increase the observed SSA values. Our hypothesis is consistent with the observation of the highest ω -values occurring around the rim of fresh craters within the feldspathic highlands terrane. Moreover, we propose that the observed variation is quantifiable, and could be used to map regolith maturity at NAC scales.

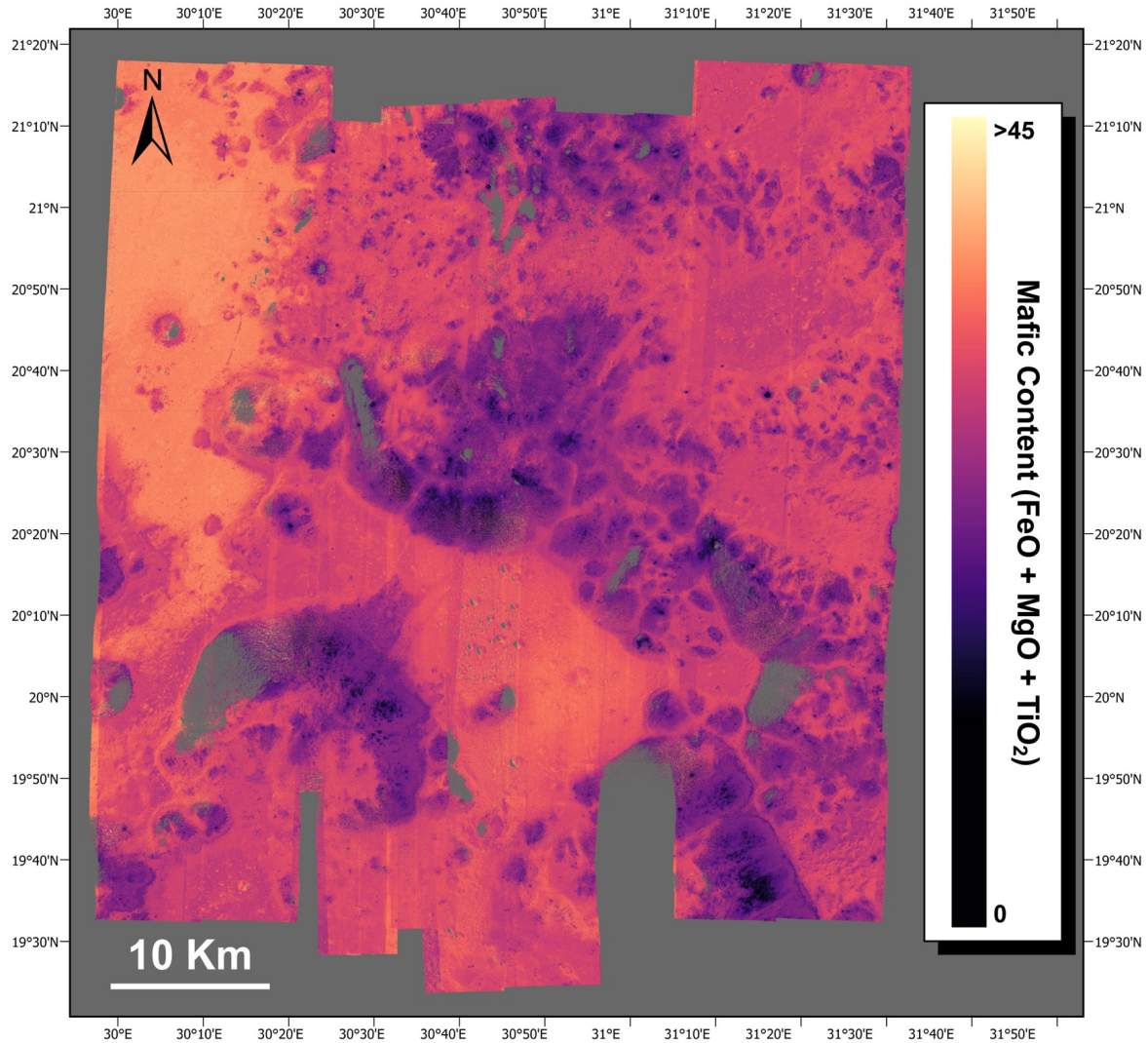


Figure 2.18. Regional map of the mafic content within the Taurus-Littrow Valley. The map was generated using the compositional relationship established using the individual soils as ground-truth observations. However, as noted in the text, immature surfaces can result in higher SSA values, which would result in an underestimate of the mafic content. Therefore, the mafic content map should be considered a lower bound (not corrected for surface maturity).

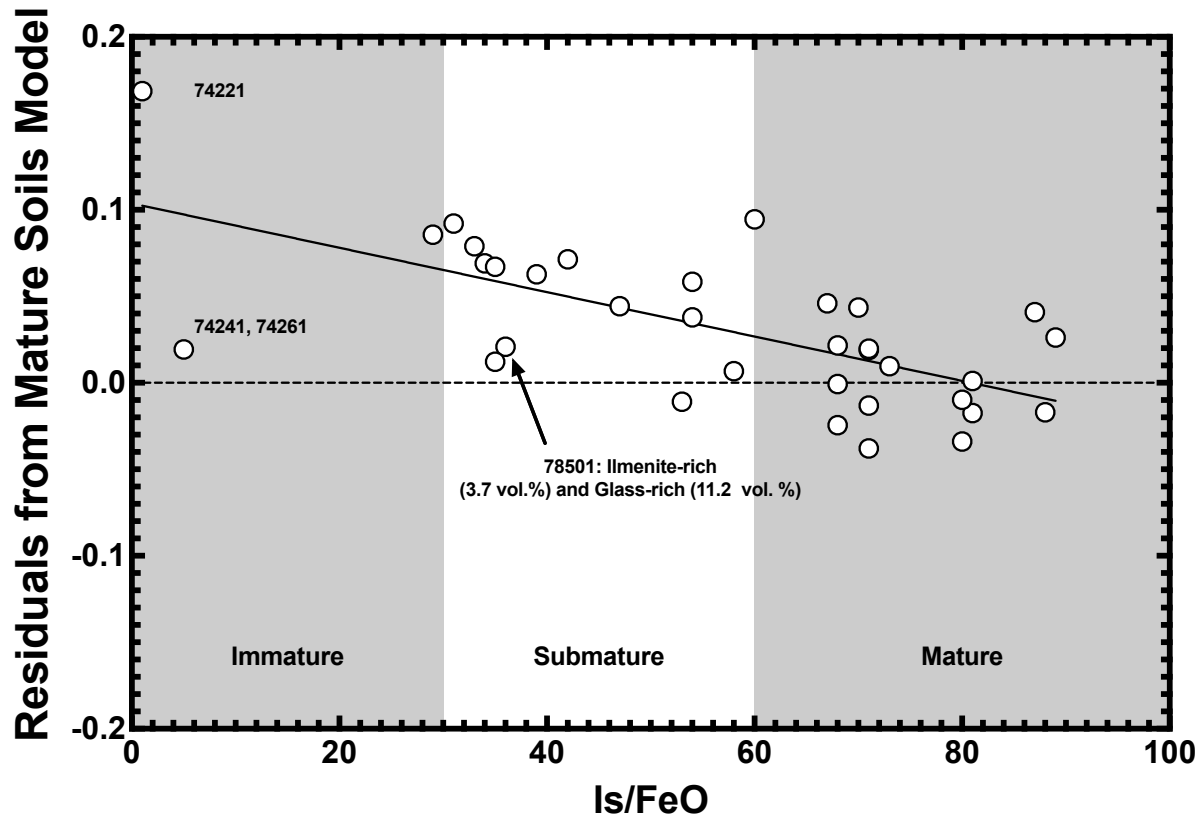


Figure 2.19. Maturity index of each sample plotted against the residual or deviation from the mature soils correlation in Figure 2.17a. For example, soils that plot above the zero reference line lie above the mature correlation in Figure 2.17a and vice versa. Samples that plot farther from the mature soils compositional correlation appear to be more immature, suggesting that the effects of sample maturity on the derived single scattering albedo may be quantifiable.

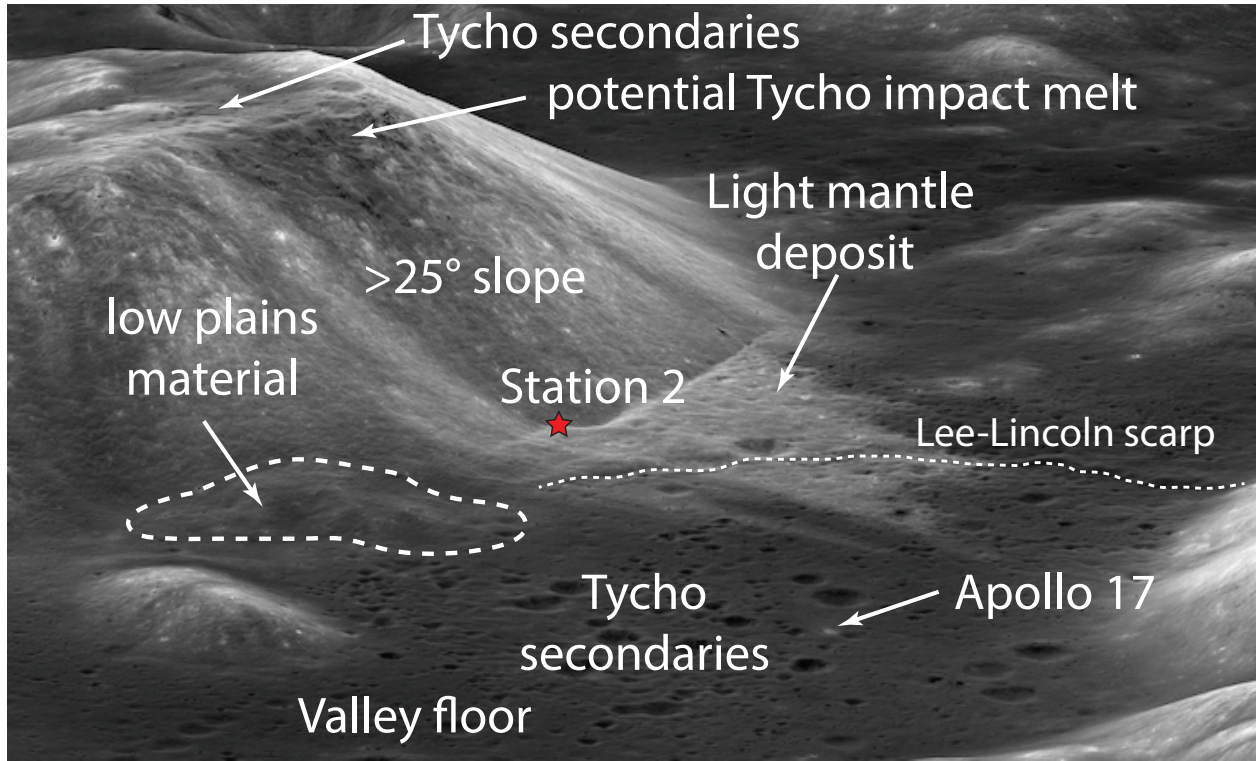


Figure 2.20. Oblique view of the light mantle deposit (LMD) at the base of South Massif and the relationship to geologic features, such as the Lee-Lincoln scarp.

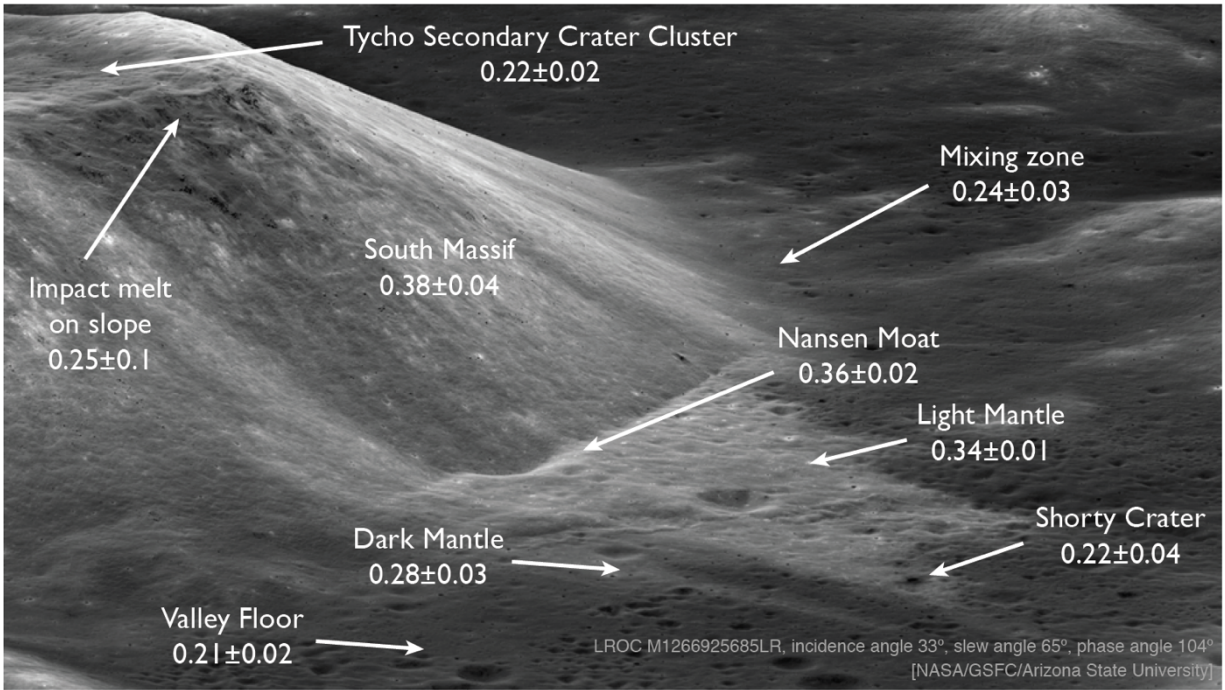


Figure 2.21. Oblique view of South Massif showing the average single scattering albedo values determined for surface units. The lowest albedo materials are associated with the Tycho secondary crater cluster at the summit of South Massif and Shorty Crater near the edge of the LMD.

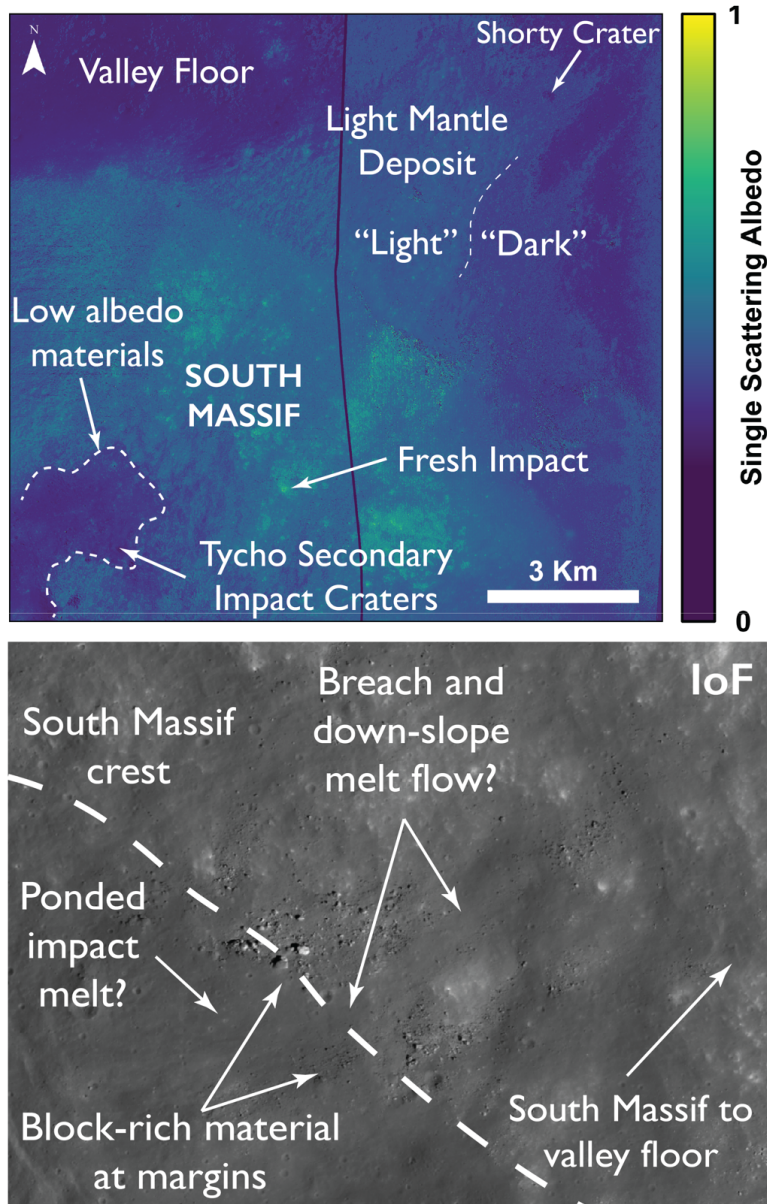


Figure 2.22. Hapke parameter map (top; e.g., single scattering albedo) of the South Massif summit showing the concentration of low albedo material on the back slope of South Massif and NAC image (bottom; M1212883755) of impact melt textures associated with the low albedo materials. The low albedo materials appear to be ponded melt that flowed down the South Massif slope and concentrated boulders at the margins of the flow. The association of the low albedo materials with Tycho secondaries and the presences of preserved flow textures strongly suggests the low albedo materials are impact melt that originated from Tycho crater.

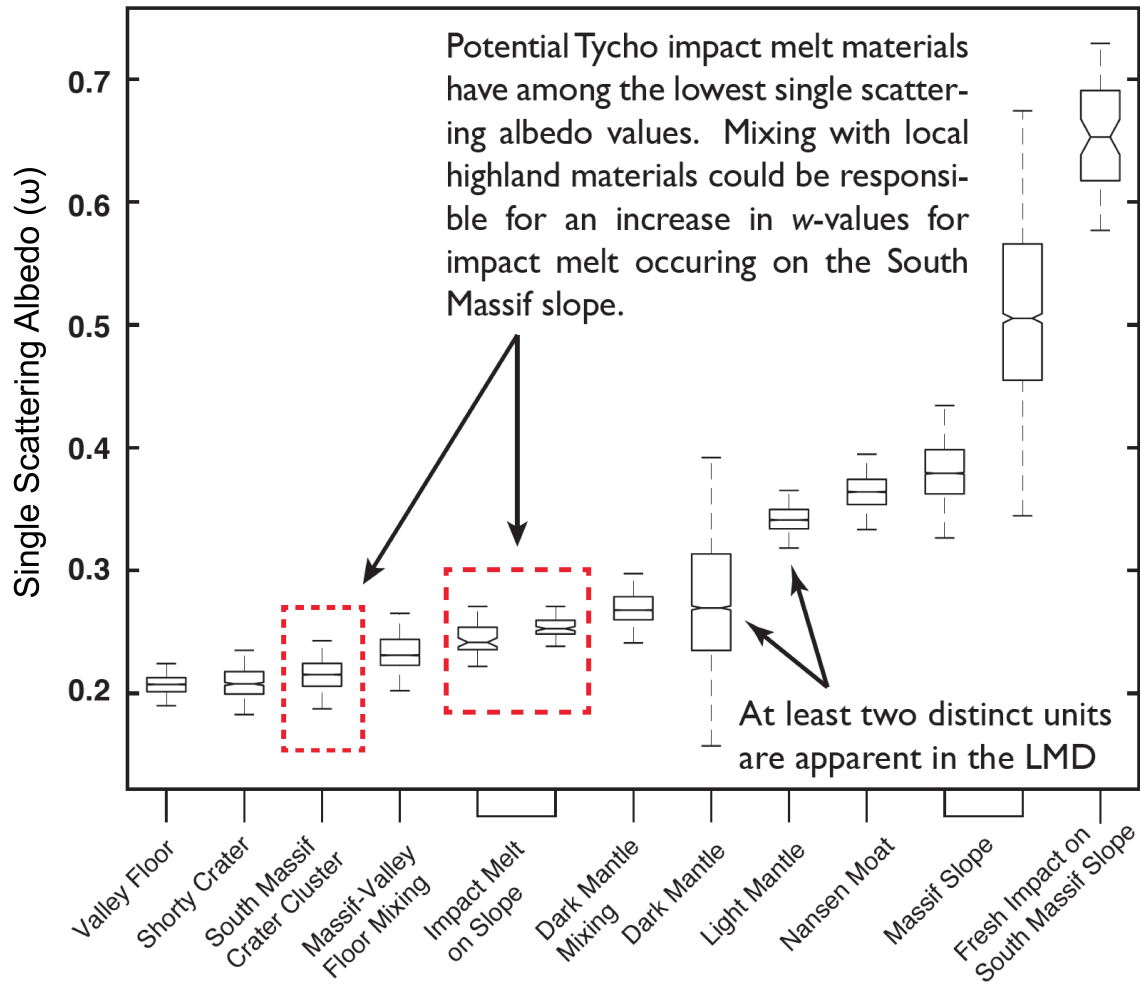


Figure 2.23. Summary statistics for surface units near South Massif and the light mantle deposit. The low albedo materials that occur on the back slope and near the summit of South Massif have among the lowest single scattering albedos within the Taurus-Littrow valley, and are most similar to Shorty Crater. We can distinguish at least two LMD units in our single scattering albedo maps, which is consistent with previous work (Schmitt et al., 2017); additional analyses are needed to determine if albedo variations are in fact related to maturity or composition. Location of surface units is shown in Figure 2.21.

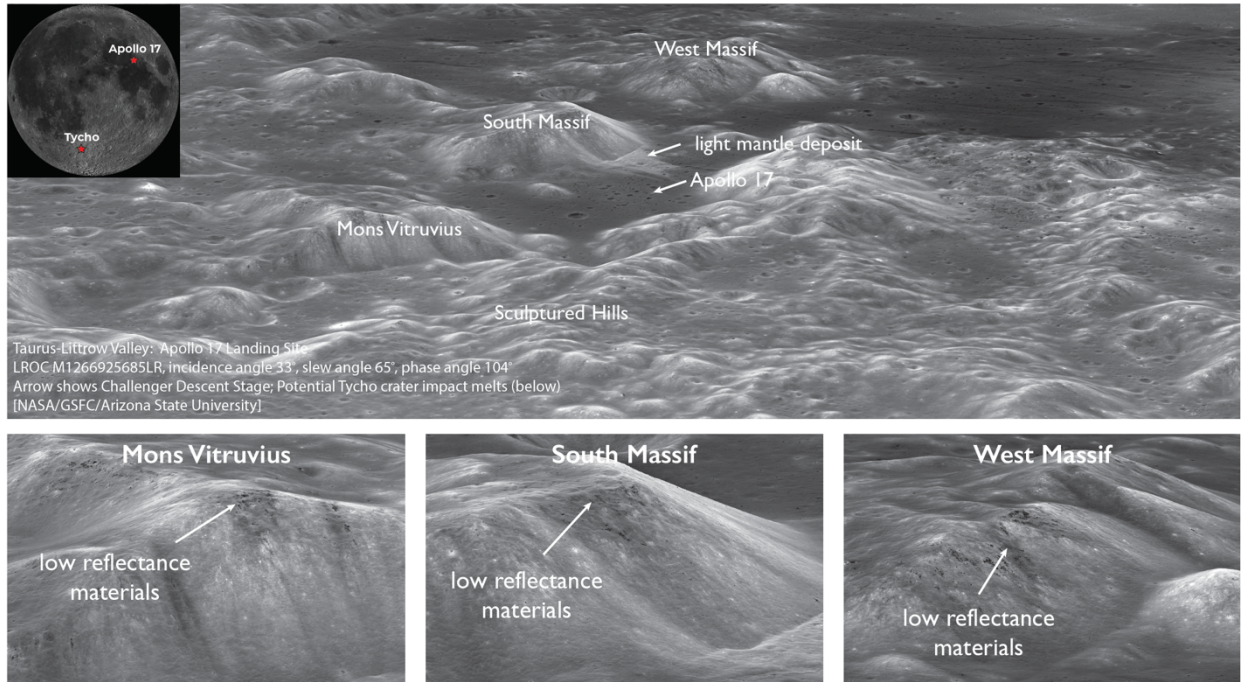


Figure 2.24. Oblique view of the Taurus-Littrow highlighting additional locations of low albedo materials at the summit of Mons Vitruvius and West Massif. These areas contain low albedo materials that have geomorphic evidence consistent with impact melt and correspond to locations of mapped Tycho secondaries. Each of these slopes generally faces to the north. LROC M1266925685LR. Incidence angle 33°, slew angle 65°, and phase angle 104°. Image credit [NASA/GSFC/Arizona State University].

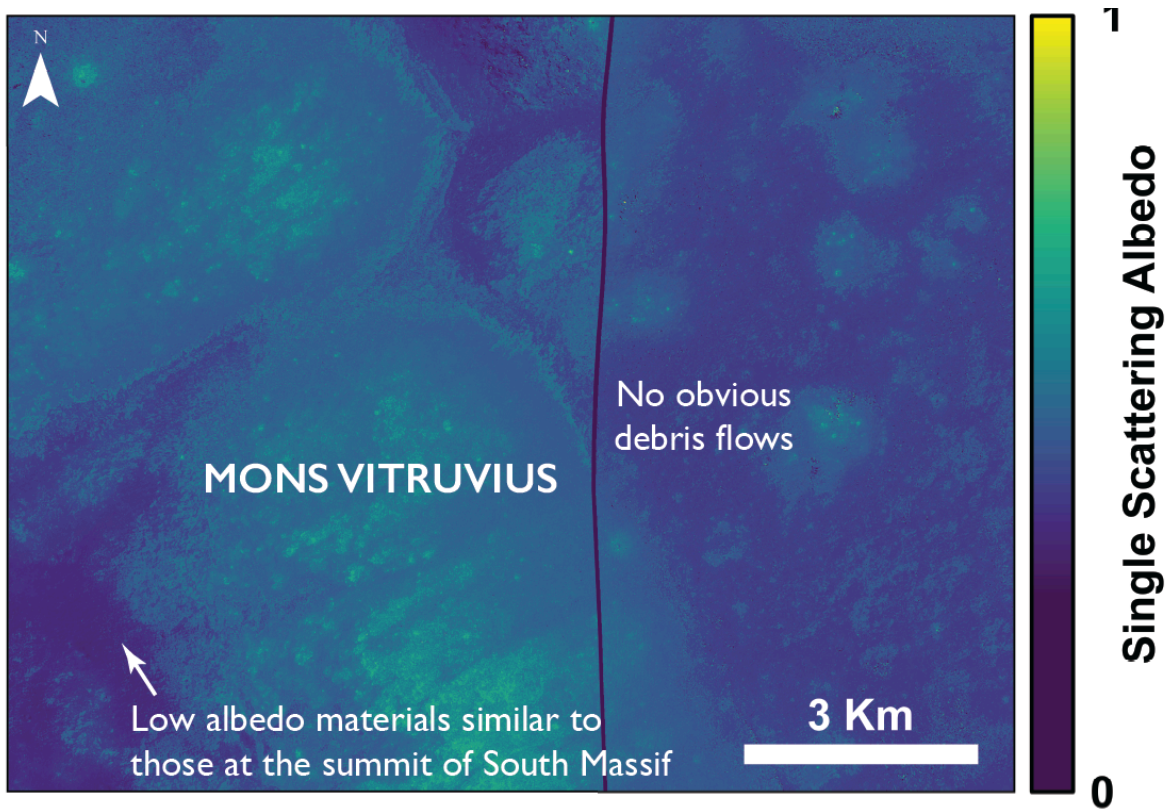


Figure 2.25. Single scattering albedo map of Mons Vitruvius. Low albedo materials occur at the summit of Mons Vitruvius and are similar in albedo and geomorphology to the low albedo materials that occur at the summit of South Massif. However, no obvious debris flows are present at the base of Mons Vitruvius.

Tables

Table 2.1
Image data for Apollo 17 regional mosaic

Image	Center latitude	Center longitude	Pixel scale (m)	Phase angle	Emission angle	Incidence angle	Sun azimuth
M1212883755R	20.507	30.401	0.95	58	14	44	e
M1212883755L	20.502	30.594	0.96	61	17	44	e
M1212876723R	20.522	30.924	0.92	50	5	45	e
M1212876723L	20.518	31.105	0.93	53	8	45	e
M1212869689R	20.515	30.449	0.97	28	19	46	e
M1212869689L	20.512	30.646	0.96	31	16	46	e
M1212862656R	20.535	30.994	1.03	22	27	46	e
M1212862656L	20.531	31.211	1.02	25	24	46	e
M1190519017R	20.320	30.848	1.15	25	27	50	w
M1190519017L	20.307	30.638	1.14	28	25	50	w
M1190504960R	20.310	30.861	1.04	54	6	49	w
M1190504960L	20.297	30.687	1.05	57	9	48	w
M1151674016R	20.417	30.051	1.16	54	13	41	e
M1151674016L	20.414	30.274	1.17	56	16	41	e
M1151666897R	20.417	31.240	1.17	55	14	41	e
M1151666897L	20.414	31.466	1.18	57	17	41	e
M1151659776R	20.428	30.097	1.17	28	16	43	e
M1151659776L	20.427	30.321	1.17	31	14	43	e
M1151652657R	20.430	31.281	1.17	29	15	43	e
M1151652657L	20.429	31.502	1.16	31	12	43	e
M159752868R	19.996	30.560	0.50	65	17	49	e
M159752868L	19.998	30.636	0.50	68	20	49	e
M159746082R	20.000	30.606	0.51	28	23	50	e
M159746082L	20.001	30.685	0.51	31	20	50	e
M152675807R	20.139	30.927	0.49	26	16	40	w
M152675807L	20.137	30.855	0.49	28	13	40	w
M152669024R	20.146	30.983	0.52	61	24	39	w
M152669024L	20.144	20.300	0.52	64	26	39	w
M150321473R	20.279	30.391	0.50	47	18	65	w
M150321473L	20.277	30.316	0.49	50	16	65	w
M150314689R	20.281	30.442	0.51	85	21	64	w
M150314689L	20.279	30.361	0.51	88	24	64	w
M144422670R	20.303	31.008	0.49	52	3	49	e
M144422670L	20.305	31.081	0.49	55	6	49	e
M144415885R	20.297	31.030	0.56	22	32	50	e
M144415885L	20.300	31.127	0.56	24	29	50	e
M137353046R	19.946	30.512	0.52	26	19	41	w
M137353046L	19.944	30.431	0.51	28	16	41	w
M137346262R	19.939	30.558	0.51	56	17	41	w
M137346262L	19.936	30.476	0.52	59	20	41	w
M134991788R	19.951	30.804	0.51	48	17	65	w
M134991788L	19.949	30.725	0.51	51	14	65	w
M134985003R	19.946	30.846	0.52	83	19	64	w
M134985003L	19.944	30.762	0.52	86	22	64	w

Table 2.2*Image data for the photometric series at Apollo 17.*

Image	Center latitude	Center longitude	Pixel scale (m)	Phase angle	Emission angle	Incidence angle	Sun azimuth
M1190519017R	20.320	30.848	1.15	25	27	50	w
M1177564379L	19.649	30.740	1.15	26	2	25	w
M1164610707R	20.106	30.724	0.97	22	1	22	e
M1164610707L	20.119	30.922	0.98	23	2	22	e
M1162255356L	19.838	30.815	1.19	30	2	29	w
M1133996580L	19.572	30.654	1.23	22	2	22	e
M1118681664L	20.191	30.833	0.85	23	2	22	e
M1116323350L	20.226	30.882	0.98	26	2	25	w
M185684128R	20.061	30.645	1.04	22	1	22	w
M172717297R	20.148	30.788	0.48	23	4	25	e
M172717297L	20.151	30.856	0.48	25	1	25	e
M109032389R	20.173	30.735	0.55	31	21	22	w
M109032389L	20.175	30.827	0.54	29	18	22	w
M106690695R	20.185	30.777	1.56	22	21	37	w
M109032389R	20.173	30.735	0.55	31	21	22	w
M1243463429R	19.024	30.859	1.07	47	1	48	e
M1228162761R	20.023	30.660	1.19	38	8	44	e
M1228162761L	20.036	30.816	1.19	40	5	44	e
M1212876723R	20.522	30.924	0.92	50	5	45	e
M1192859369R	20.227	30.920	1.04	30	4	28	w
M1192859369L	20.214	30.746	1.04	33	7	27	w
M1162255356L	19.838	30.815	1.19	30	2	29	w
M1136349272R	20.923	30.844	1.26	39	1	40	e
M134991788R	19.951	30.804	0.51	48	17	65	w
M134991788L	19.949	30.725	0.51	51	14	65	w
M129086118R	20.197	30.729	0.49	54	1	55	e
M129086118L	20.199	30.800	0.49	56	2	55	e
M104311715R	19.955	30.809	1.42	68	12	57	w
M1276388423L	20.090	30.689	0.91	82	2	81	e
M1218752280R	19.953	30.782	0.99	69	1	71	w
M1142241002R	20.218	30.926	1.21	74	1	75	w
M1142241002L	20.219	30.722	1.21	77	2	75	w
M1111607088R	20.545	30.916	1.24	81	9	73	w
M1111607088L	20.544	30.703	1.25	84	11	73	w
M1096293636R	20.507	30.691	1.32	72	1	73	w
M1096286491L	20.489	30.892	1.34	82	10	72	w
M192753724L	20.122	30.882	1.31	68	2	70	e
M180966380L	20.145	30.818	1.33	71	2	70	w
M165645700R	20.313	30.801	0.48	68	1	69	w
M165645700L	20.311	30.732	0.48	71	2	69	w
M162107606L	20.207	30.749	0.48	78	4	74	e
M134985003R	19.946	30.846	0.52	83	19	64	w
M134985003L	19.944	30.762	0.52	86	22	64	w
M131447374R	19.773	30.688	0.49	88	9	79	e
M131447374L	19.775	30.760	0.49	91	12	79	e
M113758461R	19.777	30.761	0.52	70	15	56	e
M113758461L	19.779	30.843	0.52	73	18	56	e

Table 2.3. Average Composition of Apollo 17 soil samples and LRV surface soils

Station	Sample	Location	SiO ₂	TiO ₂	Al ₂ O ₃	Cr ₂ O ₃	FeO	MnO	MgO	CaO	Na ₂ O	K ₂ O	P ₂ O ₅	Mafic Content	I _s /FeO	w	±1σ	n
LM	70011	Lunarmodule	41.3	7.83	12.2	0.40	16.1	0.22	10.0	11.0	0.34	0.08	0.07	33.9	54	0.20	0.03	12
LM	70161	ALSEP	40.3	8.99	11.6	0.46	17.0	0.23	9.79	11.0	0.32	0.08	0.08	35.8	46	0.20	0.03	13
LM	70181	Near deep core	41.0	8.21	12.2	0.45	16.5	0.23	9.80	11.0	0.37	0.09	0.07	34.5	47	0.20	0.01	16
LM	70271	SEP	40.6	8.37	12.6	0.43	16.4	0.23	9.38	11.3	0.40			34.2	56	0.20	0.01	14
S1	71041	Steno	39.9	9.53	10.8	0.47	17.8	0.24	9.66	10.8	0.38	0.08	0.07	37.0	29	0.21	0.03	15
S1	71131	Steno	39.9	10.0	10.6	0.47	17.7		9.58	10.8	0.37	0.08		37.3	33	0.20	0.02	14
S1	71151	Steno	40.1	9.53	11.1	0.45	17.6		9.39	10.8	0.38			36.5	34	0.20	0.02	14
S1	71501	Steno	39.9	9.25	11.1	0.45	17.7	0.23	9.40	10.6	0.38	0.073	0.06	36.3	35	0.20	0.04	15
S2	72321	South Massif	44.9	1.59	21.0	0.21	8.68	0.12	9.95	12.2	0.47	0.16	0.15	20.2	73	0.34	0.02	3
S2	72441	South Massif	45.0	1.50	20.7	0.25	8.72	0.13	10.2	12.4	0.42	0.19	0.17	20.4	68	0.35	0.03	3
S2	72501	South Massif	45.0	1.54	20.5	0.22	8.72	0.12	10.1	12.7	0.48	0.17	0.15	20.3	81	0.33		1
S2	72220,72240, 72260	South Massif	45.3	1.33	21.0	0.23	8.65		9.63	12.5	0.46			19.6	71	0.3	0.08	3
S3	73211	Light Mantle	44.6	1.76	20.7	0.23	8.81		9.91	12.7	0.44			20.5	39	0.39	0.03	5
S3	73221,73241, 73261,73281	Light Mantle	45.2	1.79	20.4	0.23	8.69	0.11	9.96	12.6	0.44	0.15	0.14	20.4	35	0.34	0.05	4
S4-g	74241,74261	Shorty Gray	41.6	7.72	13.4	0.42	15.4	0.20	9.31	11.3	0.46	0.13	0.10	32.4	5	0.2	0.02	2
S4-o	74221	Shorty Orange	38.6	8.80	6.5	0.68	22.2	0.29	14.4	7.70	0.37	0.08	0.04	45.4	1	0.19	0.02	2
S5	75061,75081	Camelot	39.6	9.72	11.0	0.47	17.6	0.24	9.60	10.7	0.37	0.08	0.07	37.0	37	0.37	0.04	4
S6	76501	North Massif	43.4	3.20	18.5	0.27	10.4	0.14	11.2	12.3	0.38	0.10	0.08	24.9	58	0.28	0.02	14
S6	76241,76261, 76281	North Massif	43.5	3.51	17.9	0.28	10.8	0.16	10.8	12.1	0.42	0.12	0.10	25.1	53	0.26	0.04	14
S7	77511,77531	North Massif	43.6	3.90	17.2	0.28	11.6	0.17	10.1	11.9	0.41	0.11	0.08	25.6	80	0.23	0.01	13
S8	78501	Sculptured Hills	42.8	5.31	15.7	0.36	13.3	0.18	10.0	11.7	0.39	0.09	0.07	28.6	36	0.25	0.05	4
S8	78221,78231, 78251	Sculptured Hills	43.5	3.93	17.0	0.34	11.9	0.16	10.6	11.9	0.37	0.10	0.08	26.5	89	0.28	0.07	2
S8	78421,78441, 78461,78481	Sculptured Hills	43.6	3.52	16.9	0.35	12.2	0.16	11.0	11.3	0.40	0.09		26.8	80	0.24	0.05	4
S9	79121,79511	Van Serg	41.9	6.11	13.8	0.40	15.3	0.23	10.1	10.7	0.42	0.09	0.06	31.6	71	0.21	0.02	2
S9	79221,79241, 79261	Van Serg	42.0	6.38	13.9	0.42	15.3	0.20	9.99	11.3	0.38	0.10	0.07	31.6	71	0.21	0.02	15

*Compositional data compiled from Heiken and McKay (1974) and Korotev et al. (1992)

**Mafic content defined as sum of MgO+FeO+TiO₂

Table 2.3 (continued) . Average Composition of Apollo 17 soil samples and LRV surface soils

Station	Sample	Location	SiO ₂	TiO ₂	Al ₂ O ₃	Cr ₂ O ₃	FeO	MnO	MgO	CaO	Na ₂ O	K ₂ O	P ₂ O ₅	Mafic Content	I _s /FeO	w	±1σ	n
LRV1	72131	Horatio-Bronte	41.3	7.95	12.6	0.43	16.3		9.41	11.2	0.40			33.7	60	0.26	0.03	4
LRV10	76131	Turning Point	43.5	3.74	17.5	0.29	11.2		10.5	12.1	0.42			25.4	70	0.31	0.05	16
LRV11	78121	Sculptured Hills	43.2	4.50	16.3	0.34	12.7		10.0	11.9	0.41	0.10		27.2	68	0.22	0.02	5
LRV12	70311,70321	Sherlock	39.9	9.97	11.1	0.46	17.3		9.36	10.7	0.38	0.07		36.7	42	0.20	0.01	14
LRV2	72141	Light Mantle	43.5	4.42	16.0	0.36	13.4	0.18	9.97	11.8	0.40	0.11	0.10	27.8	81	0.22	0.04	5
LRV3	72151,72161	Dark Mantle	42.4	5.08	14.3	0.41	15.0	0.21	10.8	11.0	0.43	0.10	0.08	30.9	87	0.24	0.03	6
LRV4/S2A	73151	Light Mantle	44.9	1.30	21.4	0.22	8.48		9.61	12.8	0.43			19.4	68	0.34	0.01	2
LRV5	74111	Light Mantle	44.8	2.56	19.9	0.26	9.75		8.91	12.7	0.43			21.2	31	0.41	0.05	5
LRV6	74121	Light Mantle	44.4	2.50	19.2	0.26	10.3	0.14	10.1	12.1	0.43	0.14	0.12	22.9	88	0.28	0.02	5
LRV7	75111	Victory Crater	41.8	6.83	12.8	0.45	16.1		10.3	10.7	0.42			33.2	54	0.23	0.06	6
LRV8	75121	Horatio-Victory	41.9	6.58	13.4	0.42	15.7		9.86	11.3	0.40			32.1	67	0.23	0.06	6
LRV9	76121	SEP-Station 6	42.2	6.14	14.3	0.39	14.6		9.83	11.3	0.41			30.6	71	0.19	0.01	13

*Compositional data compiled from Heiken and McKay (1974) and Korotev et al. (1992)

*Mafic content defined as sum of MgO+FeO+TiO₂

Table 2.4 External data for ground-truth calibration sites.

Location	Mafic Content	I_S/FeO	ω
Apollo 11	31.2	78	0.22
Apollo 12	27.8	63	0.29
Apollo 14	21.5	74	0.33
Apollo 15	26.6	74	0.31
Apollo 16	10.8	85	0.47
Luna 16	28.2		0.24
Luna 20	17.3		0.42
Luna 24	30.6		0.26
Chang'e-3	35.0		0.25
Lunar pure anorthosite	1.8		0.58
62231 45-20 microns [†]	12.5	80.7	0.44

*Mafic content defined as sum of MgO+FeO+TiO₂

* I_S/FeO and ω values from Clegg-Watkins et al. (2017) and references therein

[†] Data from Taylor et al. (2010)

Chapter 3: Characterizing the Geochemical and Lithologic Diversity of the Vestan Megaregolith: Implications for Remote Sensing and Planetary Differentiation

Disclosure: The following chapter is pending submission to the Journal of Geophysical Research – Planets in September 2019, as a result of the primary author’s graduate research. Co-authorship is shared with Timothy M. Hahn Jr., Nicole G. Lunning, Andrew W. Beck, Paul K. Carpenter, Robert J. Bodnar, Randy L. Korotev, Harry Y. McSween Jr., and Bradley L. Jolliff. Timothy M. Hahn Jr. prepared the manuscript. The content of the chapter contains the original submission materials in an unaltered form prior to co-author revisions.

Abstract

Howardites are analogs for the vestan regolith, offering a window into the geochemical and lithologic diversity on Vesta, and allow improved interpretation and calibration of Dawn’s vestan data through coordinated sample analysis and remote sensing studies. We have characterized six paired howardites, collected from the Dominion Range, Antarctica, during the 2010 ANSMET field season, using petrographic, electron probe microanalysis, laser ablation ICP-MS, and instrumental neutron activation analyses. These howardites contain abundant lithic clasts of eucritic and diogenitic composition, as well as atypical lithologies only recently recognized (dacite and Mg-rich harzburgite). Additionally, we identified secondary material (breccia-within-breccia and impact melt) derived from multiple impact events. We describe the characteristics of the howardites and the lithic clasts they contain to (1) establish the range and scale of petrologic diversity, (2) recognize inter- and intra-sample mineralogical and lithological heterogeneity, (3) confirm the initial pairing of these stones, and (4) demonstrate the magmatic complexity of Vesta, and by inference, early formed planetesimals. We identified a minimum of 21 individual

lithologies represented by lithic clasts >1 mm, based on textural and geochemical analysis; however, more lithologies may be represented as comminuted mineral fragments. Large inter- and intra-sample variations exist between the howardites, with distinct diogenite:eucrite and basaltic eucrite:cumulate eucrite ratios, which may be identifiable in Dawn data. We conclude that these meteorites are fragments of the megaregolith and have the potential to represent the largest sample of the vestan surface and are therefore ideal for remote sensing calibration studies.

3.1 Introduction

Asteroid 4 Vesta, thought to represent an intact and differentiated protoplanet, was investigated by the Dawn spacecraft beginning on 16 July 2011 (Russell et al., 2012). Observations have revealed a compositionally diverse surface, which records a geologically complex and violent collisional history (Combe et al., 2015; De Sanctis et al., 2012; Jaumann et al., 2012; Pieters et al., 2012; Raymond et al., 2014; Reddy et al., 2010; Ruesch et al., 2014; Russell et al., 2012; Stephan et al., 2014). The howardite-eucrite-diogenite (HED) meteorite clan was first associated with Vesta on the basis of visible and near-infrared (VISNIR) ground-based telescopic observations (Thomas B. McCord et al., 1970); Dawn's encounter has further strengthened the Vesta-HED connection by providing: (1) high-resolution VISNIR spectra that indicate pyroxene compositions similar to the HEDs, including an absence of nanophase Fe, (2) geochemical data signifying less heterogeneity than smaller asteroids, but consistent with HED meteorites, and (3) crater size-frequency distributions that document ancient surface terrains (>3 to 4 Ga) consistent with the ancient crystallization ages of eucrites and diogenites (McSween et al., 2013 and references therein). Unfortunately, detailed investigation and interpretation of remote sensing data may be limited by calibrations based on small HED samples; using larger samples may help to resolve this problem.

The modern surface of Vesta is covered by a 1 to 2 km-thick regolith, which is a consequence of large- and small-scale impacts, resulting in the comminution and redistribution of crustal and possibly mantle lithologies (Jaumann et al., 2012; Marchi et al., 2012; Marzari et al., 1996). Asteroid regoliths are often considered two-layer systems, with the near-surface representing the actively gardened portion and the underlying megaregolith consisting of fragmented lithologies and bedrock. These two portions of the regolith can be distinguished during remote-sensing observations based on physical and mineralogical characteristics (Denevi et al., 2012). For example, the megaregolith is relatively more resistant to erosion, and therefore appears as prominent features on the surface that may have only recently been exposed (i.e., Arruntia crater; Thangjam et al., 2014; Thangjam et al., 2016). Howardites, which are impact-brecciated mixtures of vestan igneous lithologies, are analogs for both portions of the regolith (Fuhrman & Papike, 1981; Pun et al., 1998); solar-wind-rich howardites represent the surface regolith (Bischoff et al., 2006; Cartwright et al., 2014; Cartwright et al., 2013), while solar-wind-poor and fragmental material denote the megaregolith. Here we follow the terminology of Warren et al. (2009) and denote “regolithic” howardites as having spent a prolonged period in the active surface regolith, and therefore enriched in solar-wind implanted noble gases, chondritic components, and glasses. We define megaregolithic howardites as those lacking characteristics associated with regolithic howardites, while containing a population of large and abundant lithic clasts.

Howardites are complex breccias composed of eucritic and diogenitic lithic clasts, in addition to comminuted mineral fragments, impact melts, and exogenous materials. Eucrites are basaltic rocks composed primarily of pigeonite and plagioclase (Hsu & Crozaz, 1996, 1997; Mayne et al., 2009), thought to represent surface flows and shallow intrusives (Duke & Silver, 1967). Diogenites are orthopyroxenites, harzburgites, and dunites (Beck & McSween, 2010; Beck

et al., 2011; Fowler et al., 1994, 1995; Shearer et al., 2010), and have been hypothesized to represent cumulates or residua formed during planetary differentiation (Mandler & Elkins-Tanton, 2013; D. W. Mittlefehldt, 1994; David W. Mittlefehldt et al., 2012; Righter & Drake, 1997). A number of studies have systematically characterized howardites in an attempt to understand the diversity, heterogeneity, and properties of the vestan regolith to allow improved interpretation of Dawn's vestan data (e.g., Beck et al., 2015; Beck et al., 2012; Lunning et al., 2016; D. W. Mittlefehldt et al., 2013). To increase the effective sample size, allowing for a more representative view of the vestan surface and identification of important mineralogical features, howardite pairing groups have been targeted for characterization studies. Recently, Lunning et al. (2016) conducted a systematic study of the Grosvenor Mountain (GRO) 95 howardite pairing group (total mass ~212 g; pre-atmospheric radius 10-15 cm), which samples the surface regolith (Cartwright et al., 2014). Beck et al. (2012) examined the Pecora Escarpment (PCA) 02 howardites (total mass ~135 g; pre-atmospheric radius 40-60 cm) representing the megaregolith, an interpretation based on subsequent solar-wind implanted noble gas analyses by Cartwright et al. (2013).

As a complement to these studies, we have conducted a petrographic and geochemical investigation of the Dominion Range (DOM) 2010 howardites (total mass ~1.1 kg) to quantify further the characteristics of the vestan regolith. Here we summarize the bulk geochemistry and modal mineralogy of the howardites, mineral compositions of lithic clasts, and provide a comparison to other howardite pairing groups. The DOM 10 howardites are among the most geochemically and lithologically heterogeneous howardites, and have the potential to be the largest sample of the vestan surface in our collection. Although solar-wind implanted noble gas analyses have not been conducted on the DOM 10 howardites, we posit they are samples of the vestan megaregolith and provide evidence to support this suggestion. Additionally, we discuss

characteristics of these meteorites that may have implications for spectroscopic studies of the vestan surface and the differentiation of early formed planetesimals.

3.2 Materials and Methods

3.2.1 Samples

We examined six meteorites from a proposed howardite pairing group collected from the Dominion Range (DOM), Antarctica, in 2010 (Table 3.1). The initial pairing of these stones was based on proximity of collection (1.5 km radius; Figure 3.1) and petrographic similarities (Corrigan et al., 2011). During our preliminary investigation, we examined a single thin section from each stone to characterize petrologic and textural variations between samples and confirm initial pairing (DOM 10838,6; 10100,8; 10120,6; 10837,7; 10105,6; 10839,6). We subsequently obtained additional sections from separate areas within three stones (DOM 10100,21; 10105,10; 10838,10) to quantify intra-sample variations. Additionally, we obtained chip samples for each stone to characterize the bulk geochemistry.

3.2.2 Electron Probe Microanalysis (EPMA)

Major- and minor-element abundances in minerals were determined using a Cameca SX-100 electron microprobe at the University of Tennessee and a JEOL 8200 electron microprobe at Washington University in St. Louis; mineral analyses were performed using the operating conditions described in Hahn et al. (2017) and Seddio et al. (2013), respectively. For the analyses taken with the Cameca, Standard PAP corrections were applied (Pouchou & Pichoir, 1991). For the analyses taken with the JEOL 8200, we used Probe for EPMA software ~~was used~~ for data collection and processing, using ZAF and Phi-Rho-Z ($\phi(\sigma z)$) correction algorithms. Natural and synthetic standards were used for calibration, with analyses of standards deviating <1 % from known values.

3.2.3 Laser Ablation ICP-MS

We measured pyroxene trace-element concentrations *in-situ* at Virginia Tech using an Agilent 7500ce inductively coupled plasma mass spectrometer (ICP-MS) equipped with an Excimer 193 nm ArF GeoLasPro laser for sample ablation. The spot size of each analysis was controlled by the availability of fracture- and inclusion-free areas (16-90 μm), with between 1 and 3 spots analyzed per grain. The NIST SRM610 reference glass was used as an external standard. At the beginning and end of each data collection period (~2 hours), the reference standard was analyzed to allow for drift correction. Prior to each analysis, approximately 60 seconds of He gas background (blank) signal was collected. Samples were ablated in a helium atmosphere at a repetition rate of 5 Hz for 20 to 60 s. During ablation, a helium-argon gas mixture that continuously flows through the sample cell transports the analyte to the ICP-MS system. The LA ICP-MS lab at Virginia Tech has previously established 3σ analytical precision for the REEs analyzed during the course of this study as follows: Ce 0-5 %; Pr and Eu 5-10 %; La, Nd, Sm, Gd, Dy, Er, Yb, and Lu 10-20 %. To determine reproducibility, the NIST SRM610 was used as a reference, and USGS standards BCR-2G, BHVO-2G, BIR-1G, NKT-1G, and NIST SRM612 and 614 were analyzed as “unknowns”. Standards were analyzed five times following routine analytical procedures. USGS standards BCR-2G, BHVO-2G, and BIR-1G are natural basalt glasses, and NKT-1G is a natural nephelinite. For data reduction purposes we utilized the SILLS software program, which provides time-resolved signal analysis, which provides a method to evaluate and eliminate from the quantification procedure portions of the signal representing contamination, whether from the surface or inclusions (Guillong et al., 2008). Therefore, only acceptable signals, interpreted to represent robust analyses of single, contaminant-free phases, are used in the data-reduction process.

3.2.4 Instrumental neutron Activation Analysis (INAA)

We analyzed subsamples of each howardite by INAA at Washington University to determine select major- and trace-element concentrations. For each howardite, at least three chip subsamples were requested for analysis by INAA. All samples were first photographed and separated into sub-splits weighing ~60 to 130 mg, with a total of twenty sub-splits analyzed. Samples were sub-divided by wrapping each sample in weighing paper and lightly striking the chip samples with a stainless steel chisel. Sample fragments were continually broken until all fragments were less than 3 mm in diameter. Subsamples for INAA consisted of either a single rock fragment or several fragments produced during the subdivision procedure. For INAA, subsamples were sealed into tubes of ultrapure fused silica and then irradiated in the University of Missouri Research Reactor with a thermal neutron flux of $5 \times 10^{13} \text{ cm}^{-2} \text{ s}^{-1}$ for 36 hours. Each sample tube was radio assayed by gamma-ray spectrometry at least four times between 6 and 24 days after irradiation, with initial measurements performed for longer duration and closer to the detector. The TEABAGS program of Lindstrom and Korotev (1982) was used for INAA data reduction.

3.2.5 Fused bead analysis

Following INAA, we analyzed the bulk major-element composition of select samples by fused bead (FB) EPMA. Subsamples used for INAA were still too radioactive, which prevented handling of the samples; therefore, we chose to analyze only samples for which we had a surplus of non-irradiated material (Table 3.2; DOM 10100,27; DOM 10837,16; DOM 10100,22; DOM 10100,24; DOM 10120,12; and DOM 10120,15). Additionally, we included the BHVO-1 standard to assess any effects of our sample preparation procedures (e.g., volatile loss during heating). The remaining, non-irradiated subsamples were first ground in an agate mortar and pestle to homogenize each subsample. A molybdenum strip resistance heater was then used to fuse the resulting powers under an argon atmosphere following the procedure described in Brown (1977)

and Jolliff et al. (1991). The samples were heated above the liquidus to completely melt the powder and allow sufficient mixing; complete melting was assessed through visual estimation. The current was rapidly removed from the Mo strip to promote quenching of the fused glass bead.

After the powders were fused, each fused bead was mounted into a 1" epoxy round following the Lunar and Meteorite Curatorial Thin Section Laboratory sample processing procedure. At least two fused beads were created and mounted for each available sample to improve the accuracy of determining the bulk composition. We analyzed the FBs for 14 major and minor elements using the JEOL JXA-8200 electron microprobe at Washington University in St. Louis. Spot analyses were conducted with an accelerating voltage of 15 keV, a beam current of 25 nA, and a 20 micron spot size. We measured the concentrations of Na, Mg, Al, Si, Mn, Fe, K, P, Ni, Cr, Ti, Ca, S, and Mo; natural and synthetic standard materials were measured for calibration (Na–albite; Mg–forsterite; Al–anorthite; Si, Ca–wollastonite; Mn–Mn-olivine; Fe–hematite; K–orthoclase; P–apatite; Ni–Ni olivine; Cr– Cr₂O₃; Ti–rutile; S–pyrite; Mo–molybdenum metal. Typical detection limits for the elements analyzed were, in wt.% element, ~0.01; only Ni and Mo had higher detection limits of 0.02 and 0.04 wt.% element, respectively. Background subtraction and matrix corrections were applied using the mean atomic number correction and standard ZAF methods, respectively. We directly measured Mo concentrations to assess the diffusion of Mo into the melt and the loss of Fe from the melt to the molybdenum metal during heating. This procedure was done to assess whether low analytical totals for the elements known to be in the samples are because of a high concentration of Mo dissolved in the glass beads. An interference correction to account for the overlapping Mo and S peaks (173.168 and 172.096 mm). The average MoO₃ of the BHVO-1 standard was 2.35 wt.% (Table 3.2); therefore, we only included analyses with <2 wt.% Mo when determining the average bulk composition of the FBs, and we report averages on

a Mo-free basis in Table 3.3. Molybdenum concentrations averaged 0.8 wt.% MoO₃ in the fused bead analyses. Oxide concentrations determined by EPMA were typically within 1-5% of that determined by INAA, except for FeO (~10-12% lower than INAA-derived concentrations). The apparent loss of Fe in the fused beads is attributed to the incorporation of Fe into Mo metal.

3.2.6 Compositional and Mineralogical Mapping by EPMA

The petrology- and mineralogy-oriented communities have long recognized the need for the integration of quantitative chemical analyses with qualitative observations (e.g., textural analysis). In response, numerous efforts have focused on the integration of geochemical datasets and image processing software to extract and interpret geochemical information, while retaining textural relationships. Only moderate success has been achieved, however, because applications have generally been limited to simple assemblages that contain relatively few mineral phases with homogeneous chemical compositions, and a long data-acquisition time is required (i.e., Maloy & Treiman, 2007). We provide two methods for integrating EPMA compositional mapping with remote sensing software, Environment for Visualizing of Images (ENVI) and IDL Workspace. Our methods provide a powerful tool for petrologic investigations and alleviate current issues with similar techniques (i.e., Pret et al. 2010). Using complex howardite breccias, we demonstrate applications to relevant petrologic problems. Detailed documentation of data and image analysis procedures will be made available, upon request, in the form of IDL scripts (data analysis and visualization) and ENVI tutorials (image processing and visualization).

Mineralogic and Lithologic Mapping

Mineralogic and lithologic distribution maps were produced for each thin section to determine mineral abundances and variations in the distribution of lithologies (Beck et al., 2012; Lunning et al., 2016). Specifically, 10 elemental x-ray maps were collected in a series of two

passes using a combination of wavelength- and energy-dispersive spectrometers (WDS: Fe, Mg, Si, Al, Ca, Cr, Ni, K, and EDS: Ti and S); these elements provide the compositional resolution needed to chemically distinguish the various HED lithologies. A potential of 15 kV and a beam current of 30 nA with a 1 μm beam and 8 μm step-size was used during elemental mapping. Dwell times were 50 ms for all elements. The acquisition of elemental x-ray maps for mineralogic and lithologic mapping is akin to typical EPMA elemental mapping (i.e., x-ray intensities), whereas the quantitative procedure described below combines high-intensity x-ray mapping with high-level matrix corrections to produce quantitative analyses at each individual pixel (i.e., wt.% element; Figure 3.2).

Quantitative Compositional Mapping (QCM)

Compositional mapping by EPMA can include sophisticated background measurements and subtraction, using background offset measurements, and a full matrix correction at each pixel, resulting in an elemental concentration map. For QCM, the per-pixel count time is 2 to 3 orders of magnitude less than traditional spot analyses. To alleviate the issue of short signal integration times, a high probe current (>100 nA) was used during the QCM procedure to collect a sufficient number of X-rays, as compared to probe currents used during standard EMPA spot analyses (e.g., 15-30 nA; Figure 3.2).

In this study, EPMA compositional maps were acquired using the JEOL JXA-8200 with 5 wavelength-dispersive spectrometers and a silicon-drift EDS, using JEOL and Probe Software applications, at Washington University in St. Louis. Analytical conditions of 15kV, 100 to 250 nA, 3 micron step size and beam diameter, and a dwell time of 150 to 500 msec were used during the mapping procedure (Figure 3.2). A full $\phi(\rho z)$ correction was applied to each pixel in the

acquired X-ray intensity maps using Probe Image and Calcimage software; the calibration uses a conventional quantitative analysis standardization, with WDS background subtraction made using the mean atomic number (MAN) background correction (Donovan et al., 1996; 2016; Carpenter et al., 2017). This correction procedure allows the counting time to be spent entirely on the analytical peak, thus improving significantly the analytical sensitivity during elemental mapping. Similar to the mineralogic and lithologic mapping procedure described previously, two passes were used to obtain 10 elemental concentration maps, with typical acquisition times of 12 to 24 hours, with ~4 hours of computational time required for matrix corrections.

Data Processing and Classification

For both mapping procedures described above, a “geochemical information cube”, analogous to a multispectral image cube, was then created by combining elemental maps (e.g., x-ray intensities and wt.% element) using remote-sensing software ENVI 4.2 (Figure 3.2). Using coordinated point analyses, regions of interest (ROIs) were then defined for individual mineral phases to develop a “training set” for classification. To allow for a direct comparison to data of Lunning et al. (2016), we applied ROIs that were consistent between pairing groups. Additionally, phase ROIs were selected on a clast-by-clast basis to elucidate key features in the matrix mineralogy (e.g., from which clasts are mineral fragments derived?). The thin-sections were then classified using a supervised classification procedure in ENVI (minimum distance), where all pixels in the image (i.e., thin section) are assigned to a specific mineral class based on their Euclidean distance from each ROI average in n-dimensional elemental space. Pixels that lie outside a set standard deviation for each class are deemed unclassified. Prior to classification we removed cracks and background epoxy from the image using a minimum value protocol, where pixels in the image that fall below a given threshold are discarded during classification. Special

precautions were taken for non-silicate phases, which naturally have low totals because oxygen is calculated rather than measured by EPMA. Classifications are performed iteratively, where in each successive classification, phases that are unclassified (i.e., compositionally distinct from other classified phases) are used to generate new ROIs and classification routines are iterated until the total number of unclassified pixels is $< 5\%$; lower values correspond to more reliable classifications. Classifications were validated using “ground-truth” analyses (point analyses). The beam- and step-sizes used during mapping constrain the resolution of the final classification image; therefore, larger uncertainties are expected for small and minor phases because their classification may be based on only a few pixels.

3.3 Results

3.3.1 Petrography

The DOM 10 howardites are composed of polycrystalline and polymineralic (lithic) clasts, in addition to secondary impact-derived breccia clasts (breccia-within-breccia), impact melts, and non-typical HED material, set in a fine-grained matrix of largely comminuted plagioclase and pyroxene. The abundance of lithic clasts varies between sections, with some containing less than 3 visible lithic clasts, while others include >15 ; lithic clasts are generally >1 mm in the longest dimension, although smaller clasts are observed, and can be up to 6 mm. Textures within the lithic clasts include subophitic to ophitic, spherulitic, granular, and granoblastic; grains sizes range from very fine-grained (<0.1 mm) to coarse-grained (>5 mm). Three types of breccia domains can be distinguished: a monomict diogenite, a polymict eucrite, and a howardite breccia containing large and abundant Mg-rich olivine grains. Impact melts are present, but not ubiquitous, in all thin-sections. Impact melt textures are vitrophyric and clast-rich. Two sections (10100,21 and

10105,10) contain shock melt veins that traverse the sections, with evidence of flow and crystallization at the margins, suggesting the rock was relatively coherent at the time of formation.

3.3.2 Bulk Geochemistry

Mineralogic variation between howardite breccias is common, which results in compositional variation between subsamples, and reflects the proportion of eucritic and diogenitic material. We report the bulk composition of the DOM 10 howardite subsamples determined by INAA, alongside the estimated percentage of eucritic material (POEM) in the howardites in Table 3.4. The POEM was calculated using the method of Jérôme and Goles (1971), which assumes the polymict breccias are two-component mixtures; we discuss later the possibility that the HED meteorite suite is not a simple binary mixture. Specifically, we compared Ca concentrations to mean basaltic eucrite and diogenite ($POEM_{Ca}$; Mittlefehldt et al. 2013). The $POEM_{Ca}$ in the breccias ranges from near end-member diogenite to 90 $POEM_{Ca}$ (Figure 3.3; 90% eucritic material), which supports the identification of multiple breccia domains in the DOM 10 howardites.

Bulk trace-element characteristics of the DOM 10 howardites share similarities to historical analyses of HEDs (Figure 3.4); however, several subsamples are anomalous, indicating the breccias are not simply two component mixtures. For instance, subsamples of 10837 and 10838 display a factor of 2 to 3 enrichment in K relative to average eucrite (Figures 3.4 and 3.5). For reference, we plot the calculated major- and trace-element chemistry of the dacite lithology identified by Hahn et al. (2017).

In addition to analysis of trace-element compositions by INAA, bulk major- and minor-element compositions were determined by analysis of fused beads. Average bulk compositions for

the samples analyzed are reported on a Mo-free basis in Table 3.3. We compared the oxide concentrations determined by INAA to the concentrations determined from fused beads. Figure 3.6 shows the oxide concentrations determined by INAA plotted against the concentrations determined by analysis of FBs (wt. % FeO, Na₂O, CaO, and Cr₂O₃). In general, FeO and Na₂O are generally lower in the FBs, which is consistent with Fe loss to Mo metal and volatile loss of Na₂O during heating; however, in some instances the FB oxide concentrations are above the 1:1; this can be interpreted to suggest that while loss of Fe and Na is apparent, there is some inter- or intra-sample variation responsible for the scatter in the fused bead data. In other words, on the sampling scale of the crushed meteorite powder, there is a large amount of geochemical heterogeneity, as is consistent with and typical for the complex howardite breccias; this observation and conclusion is further supported by the thin-section compositional mapping and detailed petrologic investigation discussed below.

When comparing the bulk geochemistry of the FBs to previous analyses of HEDs, the subsamples appear to be representative of typical howardites and have not sampled end-member lithologies (e.g., eucrites and diogenites). For example, Figure 3.7 shows the elemental composition of the FBs in comparison to a compilation of HED compositions (Mittlefehldt et al., 2013). As expected, the samples have compositions characteristic of a two-component mixture of eucrite and diogenite lithologies. A few samples, DOM 10100,24; 10120,12; and 10120,15, have chemical signatures indicative of a diogenite-rich breccia; however, a minor eucrite component is also apparent. Unfortunately, the bulk geochemistry of the FBs provides little to no new insight into the petrology of the Dominion Range 2010 howardites and suggests that a detailed investigation of individual lithologies within the breccias is required to fully understand the

compositional and petrologic diversity of the meteorites; this conclusion supports the current understanding of howardites representing complex meteorite breccias.

3.3.3 Geochemistry and Textures of Vestan Lithologies

In the ensuing sections, we present the major- and minor-element chemistry of mineral phases within lithic clasts and mineral fragments to characterize the diversity of crustal components represented in DOM 10 howardites. Owing to the large number of lithic clasts, only clasts >1 mm were examined. We attempt to separate lithologies first based on textures, followed by further separation based on mineralogy and mineral chemistry, and where necessary, provide trace-element data from pyroxenes to refine our classification further. The range of pyroxene end-member compositions for the DOM 10 howardites are shown in Figure 3.8; REE patterns for pyroxenes measured in this study are displayed in Figure 3.9. In total, 21 separate lithologies are described including 7 diogenites, 4 cumulate eucrites, 8 basaltic eucrites, and 2 recently discovered lithologies: dacite (Hahn et al., 2017) and Mg-rich Harzburgite (Hahn et al., 2018; Lunning, McSween, et al., 2015). A summary of the lithologies identified, their characteristics, and sample association is reported in Tables 3.5 and 3.6.

Diogenites

Five diogenite lithologies, represented by lithic clasts and mineral fragments (>1 mm), were identified based on mineral compositions and textures; we refer to these as diogenite types D1 through D5 (Table 3.7). Furthermore, we recognize two additional lithologies based on trace-element chemistry of orthopyroxene (types D6 and D7; Tables 3.7 and 3.8). Mineralogy of the diogenite types vary from monomineralic polycrystalline (orthopyroxene) to a 4-phase assemblage of olivine, orthopyroxene, troilite, and FeNi metal. The textures observed in the diogenite clasts

include fine-grained hypidiomorphic granular (Type 1; Figure 3.10), medium-grained granular (Types D2 and D4; Figures 10 and 11, respectively), coarse-grained granular (Type 3; Figure 3.11), fine-grained granoblastic (Type D5; Figure 3.12). Diogenite types D6 and D7 are mineral fragments that lack definitive textural context. The lithic clasts show variation in major- and minor-element concentrations consistent with previously identified diogenites; the Mg# of pyroxenes span the complete range known for diogenites (66 to 85; Figure 3.13). Minor-element concentrations are correlated with major-element composition; for example, decreasing Mg# is positively correlated with Al₂O₃ and TiO₂ wt.%, while Cr₂O₃ wt.% is negatively correlated (Figure 3.13). These characteristic minor-element compositions aid in separating lithologies (i.e., Al₂O₃ wt.% vs. Mg#). We measured trace-element concentrations in 4 of the 7 lithologies (Figures 3.11 and 3.14; Table 3.8). Variations are observed in CI normalized concentrations, REE slope, and depth of Eu anomalies. For example, types D6 and D7 show an order of magnitude difference in CI-normalized concentrations and large variations in Eu/Eu* (Figure 3.14; 0.45 to 0.02).

Cumulate Eucrites

We recognize four cumulate eucrite lithologies within the DOM 10 howardites (Figure 3.15; Types C1 through C4). Classification of these clasts as cumulate eucrites is based on pyroxene chemistry and, where possible, observed cumulate textures. Cumulate clasts consist dominantly of pyroxene and plagioclase, with accessory spinel, ilmenite, Fe metal, troilite, silica, and phosphates. Pyroxene has undergone varying degrees of exsolution to orthopyroxene-pigeonite and clinopyroxene pairs. Zircon grains were identified in Type 4 cumulate eucrite clasts. Cumulate eucrite types C1 and C2 contain pyroxene compositions that lie within the range for typical cumulate eucrites (En₄₆₋₆₅); however, types C3 and C4 are more Fe-rich, although textures clearly indicate that they are cumulate in origin (Table 3.9; Figure 3.15).

Basaltic Euclrites

At least eight basaltic euclrite types are distinguishable in the DOM 10 howardites (Figures 3.16 and 3.17; Table 3.10; Types B1 to B8). The basaltic euclrite polymineralic clasts show textures ranging from granoblastic to ophitic. Regardless of texture, all but one basaltic euclrite contain exsolution lamellae (type B8; Figure 3.17). Pyroxene exsolution lamellae tend to be more pronounced in clasts exhibiting granoblastic textures, while subophitic to ophitic clasts contain pyroxene with submicron exsolution lamellae. Basaltic euclrite types B1 through B4 all exhibit granoblastic textures. Pyroxene major-element chemistry is consistent with typical basaltic euclrites ($En_{<45}$) and pyroxene minor-element concentrations show only limited variation (Figure 3.16 and 3.17). Basaltic euclrite types B5 and B6 exhibit subophitic and ophitic textures, respectively (Figure 3.17). Although texturally these two clasts are similar, the major- and minor-element chemistry of pyroxene suggest they are chemically discrete (Table 3.10; Figure 3.17). Pyroxene compositions of type B7 basaltic euclrites are intermediate between types B5 and B6; the texture of this clast is spherulitic, with radiating plagioclase grains. Basaltic euclrite type B8 is only observed in 10838,10 and occurs as individual grains distributed throughout the section. Figure 3.17 displays the type specimen for this lithology, in addition to pyroxene major- and minor-element composition. Pyroxene within type B8 basaltic mineral fragments is strongly zoned with Mg-rich cores and Ca-rich rims (Table 3.10). Additionally, variations in core to rim compositions are observed from grain to grain, as shown in Figure 3.17.

Mg-rich harzburgites

We identified Mg-rich lithic clasts, similar to those described by Lunning et al. (2015), consisting of intergrown olivine and pyroxene (harzburgite; Figure 3.18). These clasts were the

subject of a further detailed investigation (Hahn et al., 2018). Here we only briefly describe the major-, minor-, and trace-element chemistry of the clasts, and summarize the findings of Hahn et al. (2018). Olivine and pyroxene in the harzburgite clasts show a wide variation in major-element chemistry (Mg#s 82 to 92). Minor-element correlations in pyroxene show increasing Al/Cr ratios with near constant Ti concentrations. Associated with the harzburgite clasts are euhedral to subhedral grains of Fe metal and a ubiquitous association of chromite-orthopyroxene symplectites (Figure 3.18). Trace-element concentrations in Mg-rich pyroxene are variably depleted relative to CI chondrites and are LREE-enriched.

Dacite

We identified a basaltic eucrite-like clast dominated by clinopyroxene, plagioclase, and quartz, with minor amounts of troilite, Fe metal, ilmenite, and phosphates. Unlike typical basaltic eucrites, the primary pyroxene is augite, which occurs as large (> 1mm) oikocrysts (Figure 3.19). Moreover, quartz is a major, rather than minor, phase within the clast (~ 30%). Pyroxene major- and minor-element chemistry is consistent with basaltic eucrites; however, REE abundances and the presence of primary augite suggest a more evolved origin (Figure 3.19). A more complete characterization of this lithology is given by Hahn et al. (2017).

3.3.4 Mineralogic and Lithologic Distribution Maps

Mineral modes for all nine thin sections were determined using the mapping procedures described previously, and distribution maps of the mineralogy and lithologies are shown in Figures 3.20, 3.21, and 3.22. Large variations in mineral abundances are observed between each howardite, and significant intra-sample variations were also observed (Table 3.11). For example, eucritic minerals comprise ~40% and ~84% of 10839,6 and 10838,10, respectively. However, these same

variations are observed in sections cut from the same stone, where 10838,6 contains ~36% eucritic minerals (Figure 3.21; Table 3.11). Similar intra-sample variations are observed in 10100,8 and 10100,21; however, the two sections cut from 10105 show nearly identical modal mineralogy (Table 3.8). Differences in eucrite and diogenite ratios suggest three distinct breccia clasts have likely been sampled (10:1; 4:1; 1:1; Table 3.11; Figure 3.23), and further support is given by basaltic and cumulate eucrite ratios (Figure 3.24). Furthermore, a breccia clast identified in 10838,6 contains only diogenitic minerals, suggesting a fourth breccia has been sampled. The observed variation in mineralogy is consistent with the bulk geochemistry of the howardites. Specifically, the $POEM_{Ca}$ display the same range in eucrite:diogenite ratios determined independently by mineralogic and lithologic mapping methods.

3.4 Discussion

3.4.1 Pairing of the Dominion Range 2010 Howardites

We studied, in detail, the petrology of the DOM 10 howardites in order to confirm their initial pairing. As stated previously, all six meteorites were found within an approximately 1.5 km radius. The petrologic characteristics identified in this study provide strong support for the pairing of these six howardites. First, the DOM 10 howardites contain a diverse array of lithologies related to eucritic and diogenitic rock types (Tables 3.5 and 3.6). We have shown that these are shared lithologies between the various meteorites. For example, type D2 diogenites are observed in 10837,7, 10120,6, 10105,6, and 10838,6. Second, we have identified a Mg-rich harzburgite lithology with a 2-phase symplectite of chromite and orthopyroxene that has not been recognized in other howardites, and is common to all six DOM 10 howardites; this is the most cogent argument for the pairing of the DOM 10 howardites. Therefore, in spite of the wide variation in modal

mineralogy between each stone, we conclude that the six stones in the DOM 10 howardite pairing group are indeed paired. We attribute the intra-sample mineralogical diversity to reflect the sampling of different breccia clasts within the pairing group. These breccia domains may be crucial for calibrating Dawn's vestan data.

Future cosmogenic nuclide analyses of the DOM 10 howardites could provide a more concrete conclusion as to the pairing of these stones. Additionally, such studies might incorporate howardite DOM 14169, eucrite DOM 10103, and diogenite DOM 10350 (also found within 1.5 km radius of DOM 10 howardites). Although we did not examine these meteorites during the course of this study, their preliminary petrographic descriptions (Corrigan et al., 2011) are similar to the DOM 10 howardites or, in the case of the eucrite and diogenite samples, share similar textures and mineral chemistry to lithic clasts in the DOM 10 howardites. For instance, diogenite DOM 10350 shares the same coarse-grained tabular orthopyroxenes, with similar compositions to type D3 diogenites examined here. We hypothesize that DOM 10350 may represent a large lithic clast that was "plucked" during atmospheric entry, although additional studies will be needed to support this suggestion, our initial hypothesis is supported by the intra-sample mineralogical variations observed in the DOM 10 howardites.

The heterogeneity of the DOM 10 howardites at the thin-section scale indicates that characterization of a single section from a megaregolithic howardite is insufficient to capture a representative mineralogical sample, and that characterization of multiple sections is needed. Although this observation has been made before (Lunning et al., 2015), the DOM 10 howardites exceed previously recognized heterogeneity and lithologic diversity in howardites.

3.4.2 Recognition of Distinct Lithologies

The six howardites collected during the 2010 field season from the Dominion Range sample numerous lithologies that provide fundamental information regarding the geological evolution of the asteroid Vesta. We have identified 21 petrologically distinct lithologic types: 8 basaltic eucrites, 4 cumulate eucrites, 7 diogenites, an Mg-rich harzburgite, and an evolved dacite lithology; a summary of their characteristics is given in Tables 3.5 and 3.6. We have attempted to associate each lithic clast with a specific meteorite showing similar major- and minor-element pyroxene chemistry, although other aspects may not necessarily be consistent (i.e., texture; Fowler et al., 1995; Lunning et al., 2015; Mayne et al., 2009; Mittlefehldt & Lindstrom, 2003; Shearer et al., 2010; Takeda & Graham, 1991; Warren & Jerde, 1987). Some lithologies, however, appear to be absent from the meteorite collection as whole rock samples (i.e., dacite, Mg-rich harzburgites and Fe-rich cumulates). This absence indicates a few lithic clasts likely sample previously unrecognized lithologies on Vesta, and therefore provide further constraints on geologic and differentiation processes on early formed planetesimals (e.g., Hahn et al., 2017; Hahn et al., 2018). Specifically, evolved dacite and Fe-rich cumulate eucrite clasts provide evidence that the relationships and compositional boundaries between eucrite classes are not distinct. For instance, type C3 cumulate eucrite clasts show unambiguous cumulate textures, yet the pyroxenes are well within the basaltic eucrite compositional field (Figure 3.15), providing evidence that melts more evolved than basaltic eucrites should exist on Vesta and are capable of producing Fe-rich cumulates.

A clear picture is beginning to emerge regarding the differentiation of Vesta, and by analogy, the differentiation of early formed planetesimals. Specifically, the petrologic heterogeneity identified within the HED suite through petrographic and geochemical observations

is greater than expected, and indicates the differentiation of small bodies in the early Solar System was a complex process. It is, therefore, difficult to envision how such a geologically complex meteorite suite could have originated from the solidification of a simple magma ocean; consequently, we argue against the general application of magma ocean models to planetesimal differentiation.

Our discussion of the petrologic diversity in the HED meteorite suite would not be complete without discussing the possibility that some HED meteorites may have originated on parent bodies other than Vesta. Wasson (2013) discussed several lines of evidence that the HED meteorites may not have originated on Vesta, but rather from numerous basalt-covered asteroids, which formed from a common reservoir. The working hypothesis of Wasson (2013) may explain the high degree of petrologic diversity in the HED suite, although the diversity observed in a single howardite pairing group appears to argue against this idea.

3.4.3 Samples of the Vestan Megaregolith

The DOM 10 howardites contain >21 distinct lithologies, abundant large lithic clasts, and lack chondritic components; therefore, like the PCA 02 howardites and diogenites, we propose an origin from the immature megaregolith on Vesta (Beck et al., 2012). Specifically, preservation of large mineral and lithic clasts (>1 mm) and a comparison of the mineralogic characteristics of surface regolithic and megaregolithic howardites (Table 3.12), implies the DOM 10 howardites experienced minimal impact gardening. In comparison to the PCA 02 howardites and diogenites, the DOM 10 howardites appear to have sampled a greater variety of lithologies. The GRO 95 howardites also display a more limited range in proportions of eucritic to diogenitic minerals, with distinct clusters at 4:1 and 2:1 (Figure 3.23), which suggests they have evolved towards a more

homogenized composition because of impact gardening (Lunning et al., 2016); a broader range in eucritic and diogenitic mineral proportions are observed in the DOM 10 howardites (Table 3.11), offering further support that they represent immature regolith. Therefore, we conclude that the DOM 10 howardites originated from the immature megaregolith on Vesta.

Basaltic to Cumulate Eucrite Ratio

Lunning et al. (2016) noted variations in the ratio of basaltic and cumulate eucrite material in regolithic howardites, which is an important observation, and perhaps the most significant. When comparing modal analyses for the PCA 02 and DOM 10 megaregolithic howardites, with that of regolithic howardites GRO 95, Kapoeta, Bununu, and Bholgati, we found that the abundance ratios of basaltic eucrite to cumulate eucrite appear to form clusters (Figure 3.24; Table 3.12). We hypothesize that these clusters may represent original basaltic eucrite and cumulate eucrite ratios in the source regions, and that subsequent smaller impacts have acted to homogenize those portions in the surface regolith, and left the same ratios in the underlying megaregolith. Indeed, the DOM 10 howardites contain at least three breccia types with distinctive mineralogy, two of which contain basaltic eucrite:cumulate eucrite ratios identical to Kapoeta and Bholgati (Figure 3.24; Tables 3.11 and 3.12).

Plagioclase Depletion

Lunning et al. (2016) conducted a petrologic study of the GRO 95 regolithic howardites. These howardites appear to be depleted of plagioclase relative to eucritic pyroxene (Fuhrman & Papike, 1981; Lunning et al., 2016), suggesting plagioclase may be more easily comminuted or melted by impact processes, which could serve as an indicator of regolith maturity. Lunning et al. (2016) also considered that granular sieving could be the dominant process, suggesting mature

terrains might be underlain by megaregolith that portions of which are enriched in plagioclase. The GRO 95 howardites also show a ~2:1 eucrite:diogenite ratio, which may indicate mature regolith (Warren et al., 2009; Figure 3.24). Additionally, Lunning et al. (2016) noted the broad range in the ratio of basaltic eucrite to cumulate eucrite (2:1 to 1:3), indicating unrecognized diversity of eucritic lithologies in the regolith, that may potentially be resolvable in Dawn spacecraft data (Beck et al., 2015).

The GRO 95 howardites are finer-grained, with smaller and less abundant polymineralic clasts than the DOM 10 howardites, which is consistent with separate origins for these meteorites in the surface regolith and megaregolith, respectively (Bischoff et al., 2006). Because the DOM 10 howardites are megaregolithic and relatively texturally immature, we expected to see plagioclase in abundances consistent with, or enriched, relative to eucritic pyroxene in unbrecciated eucrites (1:1; Mayne et al., 2009); instead, we observed depletions in plagioclase similar to the GRO 95 howardites (Figure 3.24a). Only DOM 10105 contains plagioclase and eucritic pyroxene in a 1:1 ratio, which is likely caused by the high abundance and large size of eucritic lithic clasts (Figure 3.22). This observation seems inconsistent with a granular sieving hypothesis (Lunning et al., 2016). The observed plagioclase depletion remains an enigmatic feature of howardites, apparently occurring in both the surface regolith and megaregolith. We note, however, considering the mass balance of such a process, the expected plagioclase enrichment by granular sieving would only occur in certain portions of the megaregolith.

Inter- and Intra-sample heterogeneity

Beck et al. (2012) investigated petrologic variations in the PCA 02 howardite and diogenite pairing group. Cosmogenic nuclide analysis suggests these meteorites represent a pre-atmospheric

meteoroid approximately 1 meter in diameter. Additionally, Beck et al. (2012) demonstrated that the PCA 02 howardites and diogenites contain silicate material with compositions covering all known HED lithologies, and the diversity of the lithologies implies they originated from a variety of source regions. These meteorites are interpreted to represent samples of the megaregolith, implying that meter-scale diversity exists in the regolith. Although no cosmic-ray exposure data are available for the DOM 10 howardites, the collective mass of the 6 howardites (~1.1 kg) is a factor of 8 larger than the PCA 02 howardites and diogenites, and therefore collectively might represent the largest piece of the vestan megaregolith in the collection that has been thoroughly characterized. Subsequent radionuclide analyses are needed to support this hypothesis.

The PCA 02 howardites and diogenites are dominated by diogenitic and olivine-rich impact-melt clasts with eucritic material interspersed, whereas the DOM 10 howardites show no clear lithologic dominance, with ratios of eucrite to diogenite ranging from 10:1 to 1:1 (Table 3.11). Unlike the DOM 10 howardites, the PCA 02 howardite and diogenite pairing group displays only small intra-sample mineralogical dissimilarities (i.e., 15% to 25% variation in total eucrite and diogenite minerals; Table 3.12); in contrast, the DOM 10 howardites can show >50% variations in eucrite and diogenite mineralogy within a single stone. We observed a single thin-section (10100,8) of breccia-within-breccia in which one side is eucrite-rich and contains no Mg-rich olivine mineral fragments, and the other side is dominated by diogenite clasts and contains Mg-rich olivines (Figure 3.20). In contrast, section 10838,6 contains a breccia clast with only diogenite minerals (Figure 3.21). DOM 10837,7 is dominated by a large impact melt clast (Figure 3.22). The DOM 10 howardites are evidence that extreme heterogeneity exists in the megaregolith, and they offer insights into regolith composition that may be detectable in Dawn data, and therefore suitable for remote sensing calibration studies.

3.4.4 Implications for Remote Sensing

Developing a data set for rigorous interpretation of Dawn's remote-sensing data of Vesta has been an important objective of some recent HED studies (Beck et al., 2013, 2015; Mittlefehldt et al., 2013; Thangjam et al., 2016). Identification and mapping of eucrite, diogenite, and howardite terrains on the vestan surface has been based on VIR pyroxene absorption bands (De Sanctis et al., 2012) and GRaND neutron absorption characteristics (Prettyman et al., 2013); however, separation of HED subgroups has proven more difficult. Nevertheless, Beck et al. (2015) have shown that principal component analysis of data from the GRaND instrument is capable of further differentiating between HED meteorite subgroups (i.e., basaltic vs. cumulate eucrites). The identification of substantial large- and small-scale mineralogical variations, both basaltic eucrite:cumulate eucrite and eucrite:diogenite ratios, within megaregolith analogs have important implications for remote sensing observations of the vestan surface. Specifically, the observation of distinctive eucrite:diogenite ratios, in combination with the array of basaltic eucrite:cumulate eucrite ratios, make the DOM 10 howardites ideal candidates for spectral calibration studies by targeting the breccia domains within the sample. Such investigations might make it possible to map these lithologic units on the vestan surface, which has the potential to advance our understanding of the regolith composition and internal structure of Vesta.

As suggested by Warren et al. (2009), the modern regolith of Vesta may be the result of a single large impact around 1 Ga. Such an event would have been the sole source of diogenitic components to the regolith, and subsequently smaller impacts would have acted to homogenize the regolith towards a 2:1 eucrite to diogenite ratio. The various eucrite to diogenite ratios in the DOM 10 howardites could thus represent original ratios in numerous ancient source regions. More recent impacts may have facilitated the excavation of this ancient material, which may be

resolvable in the Dawn data. We have also reported variations in olivine abundance (1 to 15%; Table 3.11), composition, and grain size in the DOM 10 howardites, which are useful for interpreting diagenetic lithologies containing variations in olivine content (Beck et al., 2015; i.e., dunite, harzburgite, and orthopyroxenites).

3.5 Conclusions and Summary

Petrologic and geochemical investigations of the DOM 10 howardites have revealed a diverse array of lithic clasts with compositions covering the complete spectrum of HED meteorites, in addition to lithologies not recognized as whole stones in the meteorite collection. The abundance and large size of lithic clasts indicates that these meteorites were part of the megaregolith on Vesta. In total, 21 lithologies were identified as clasts, and more may be represented in comminuted mineral fragments. Additionally, INAA analyses suggest the HED meteorite suite may not be a simple binary mixture of eucrite and diogenite material, but instead contains a third, albeit minor, component that is enriched in incompatible trace elements.

The identification of unique diogenite:eucrite and cumulate:basaltic ratios within breccia clasts likely represents the original ratios within the source regions sampled; these characteristics may be identifiable by the Dawn spacecraft. Collectively, the DOM 10 howardites have the potential to represent the largest piece of the vestan megaregolith, and therefore could be useful to interpret Dawn data from relatively fresh regions on Vesta, which may expose the underlying vestan megaregolith. The complexity of meteorite breccias provide unique challenges for petrologic characterization studies, and the mineralogic and lithologic mapping methods presented here provide a means to conduct extensive coordinated sample analysis with spacecraft calibration studies.

Figures

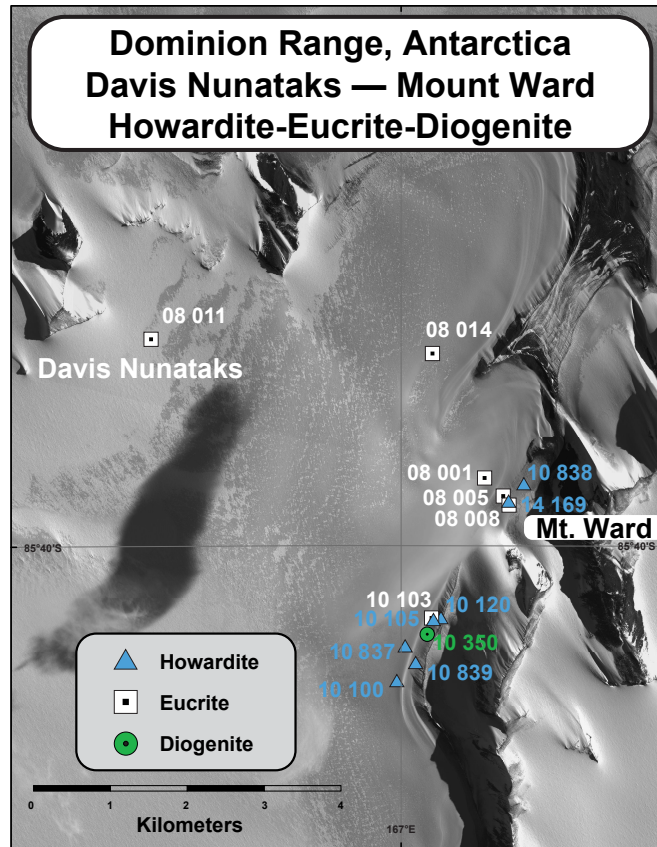
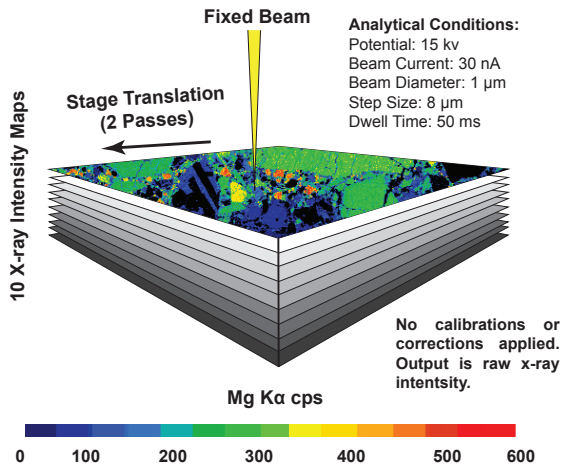


Figure 3.1. Locations of the six DOM 10 howardites collected during the 2010 ANSMET field season. All six stones were found within a 1.5 km radius. Location of a howardite (DOM 14169) collected during the 2014 field season is also shown. Additional HED finds (eucrites and diogenites) are shown in the lower image. Meteorite location map created and provided by John Schutt.

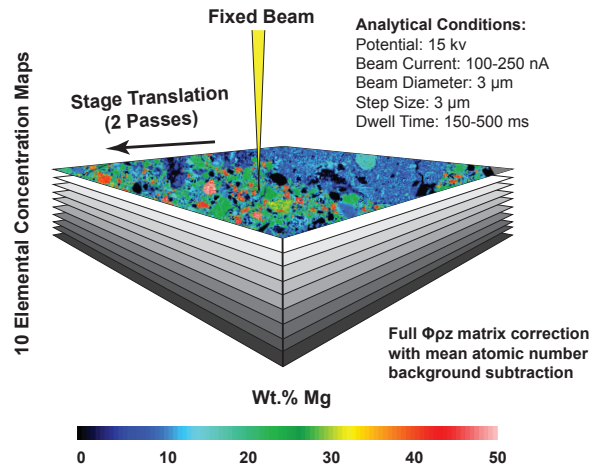
Mineralogic and Lithologic Mapping



Output Data Products:

- Mineralogic and lithologic distribution maps
- Modal mineralogy
- Fracture porosity

Quantitative Compositional Mapping



Output Data Products:

- Mineralogic and lithologic distribution maps
- Modal mineralogy
- Mineral stoichiometry
- Mineral end-member distribution maps
- Quantitative elemental ratio maps
- Fracture porosity
- Density-corrected bulk composition
- Quantitative variation diagrams

Figure 3.2. Summary graphic of the compositional mapping procedures. The mineralogic and lithologic mapping method (left) is a less robust method, and results in a mineralogic classification of the samples of interest. The quantitative compositional mapping (QCM) method (right) essentially results in the same output (mineralogic classification); however, the QCM method has the added benefit of providing a quantitative analysis at every pixel, which allows for additional data products to be produced during post-classification processing (see figure for details).

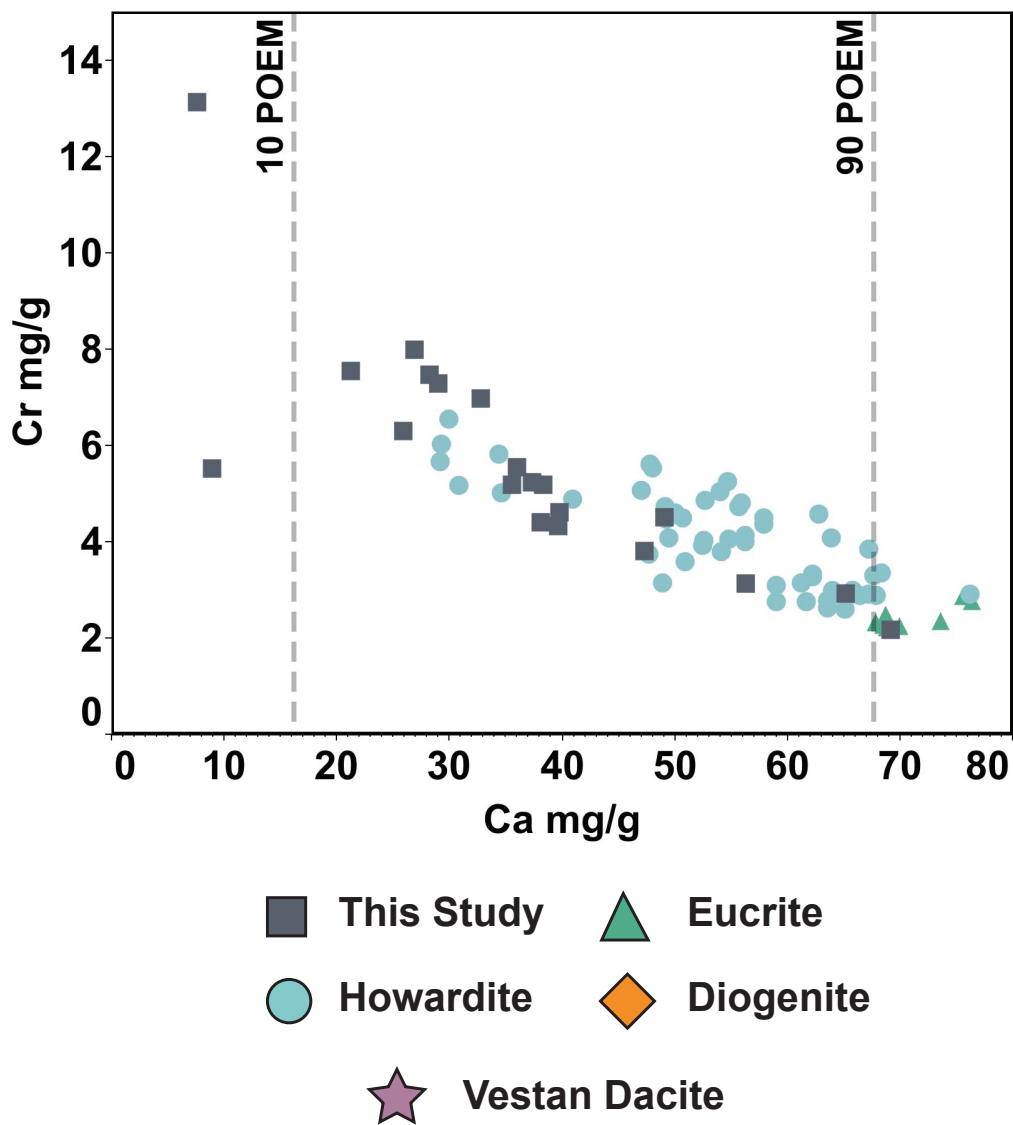


Figure 3.3. Element variation diagram for Cr and Ca. Values for 10 and 90 $POEM_{Ca}$ are shown for reference. The DOM 10 howardites display large variations in $POEM_{Ca}$, confirming the inter- and intra-sample variations previously documented using petrography and lithologic mapping. External data from (Mittlefehldt et al., 2013; Mittlefehldt, 2015).

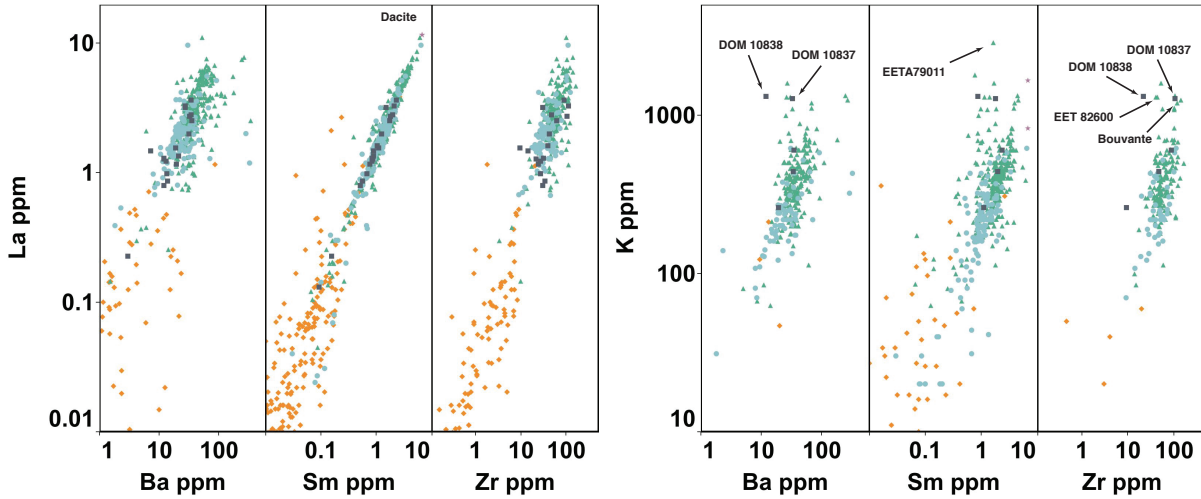


Figure 3.4. Element variation diagrams for select major- and trace-elements in the DOM 10. External data for HEDs from (Mittlefehldt et al., 2013; Mittlefehldt, 2015). Dacite composition determined by Hahn et al. (2017) using laser ablation ICP-MS mineral analyses and modal recombination. Trace-element characteristics of the DOM 10 howardites share similarities to historical HED analyses; however, several subsamples are anomalous, indicating the breccias are not simply two component mixtures. For instance, subsamples of 10837 and 10838 display a factor of 2 to 3 enrichment in K relative to average eucrite, indicating the presence of a component enriched in incompatible elements.

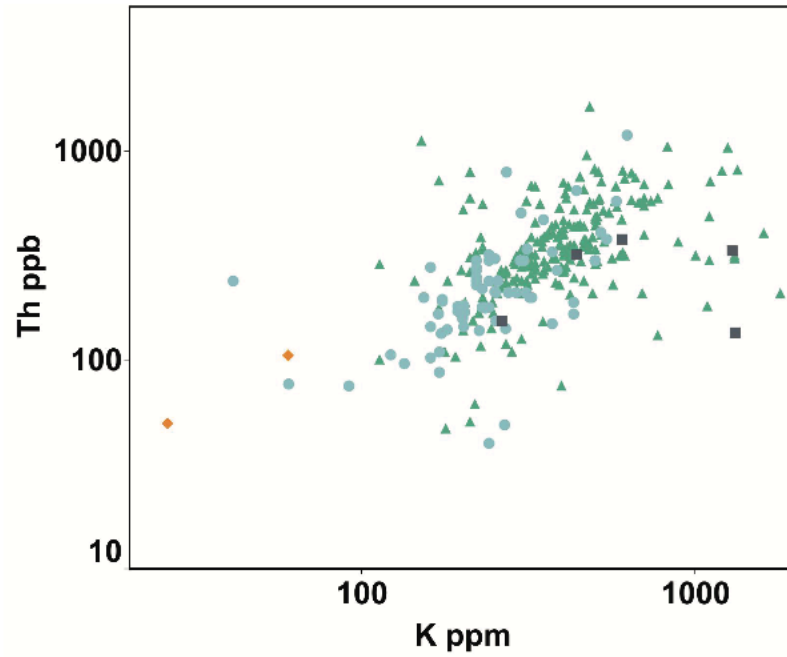


Figure 3.5. Element variation diagram for K and La determined by INAA. The DOM 10 howardite subsamples contain both K-enriched and K-depleted samples. We interpret this as a contribution from a vestan dacite component, which indicates the dacite component or its geochemical signature may be present and identifiable in other HED samples . External data from (Mittlefehldt et al., 2013; Mittlefehldt, 2015).

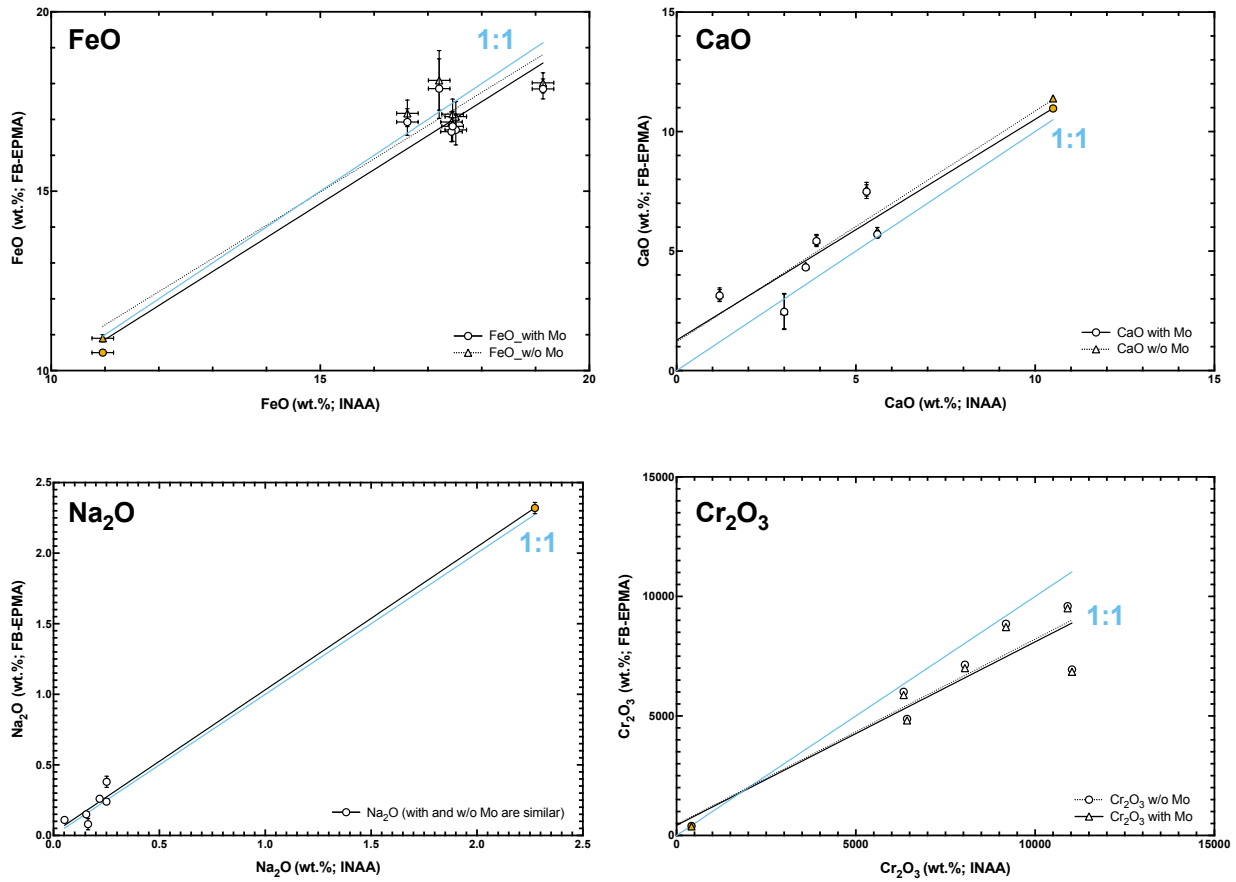


Figure 3.6. Comparison of DOM 10 howardite compositions determined by EPMA of fused beads and INAA. The INAA data are plotted against the fused bead data for FeO, CaO, Na₂O, and Cr₂O₃. The FeO and Na₂O are generally less than the 1:1 line, which suggests Fe loss to Mo metal and volatile loss of Na. However, in some cases the fused bead data are above the 1:1, which we interpret to suggest that while loss of Fe and Na is apparent, there is some inter-sample variation responsible for the scatter in the fused bead data. In other words, on the sampling scale there is a large amount of heterogeneity, as is typical for the howardites and apparent in the thin-section mineral maps. The colored symbols on the plots are the BHVO-1 sample.

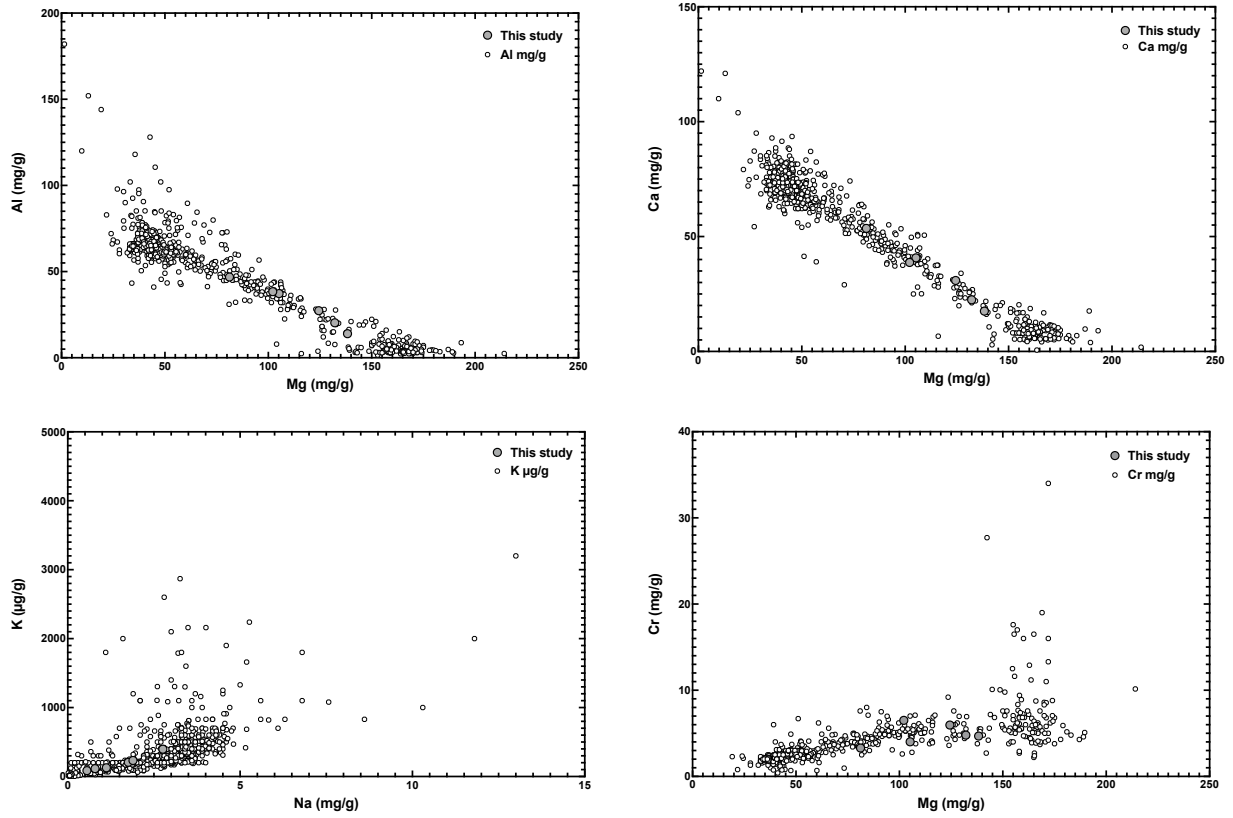
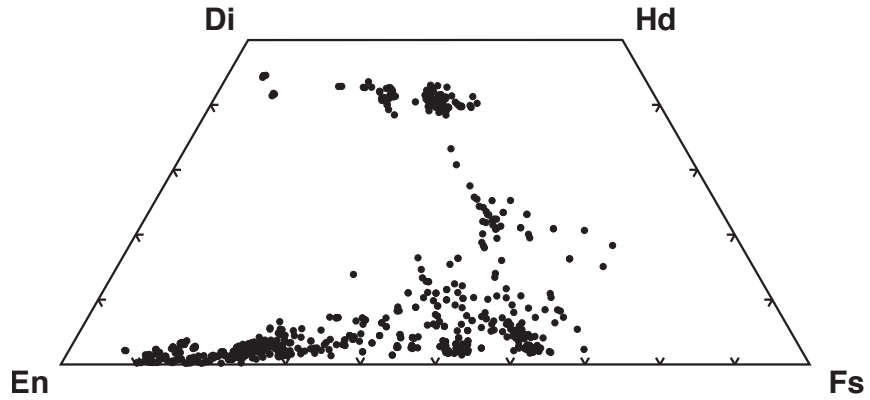


Figure 3.7. Comparison of EMPA fused bead data to historical analyses of HEDs. The DOM 10 howardites are typical howardites and are comprised of mainly a two component mixture of diogenite and eucrite material; however, proportions of eucrite to diogenite material varies significantly.



Key for Figures 8-10, 13-15, and 17

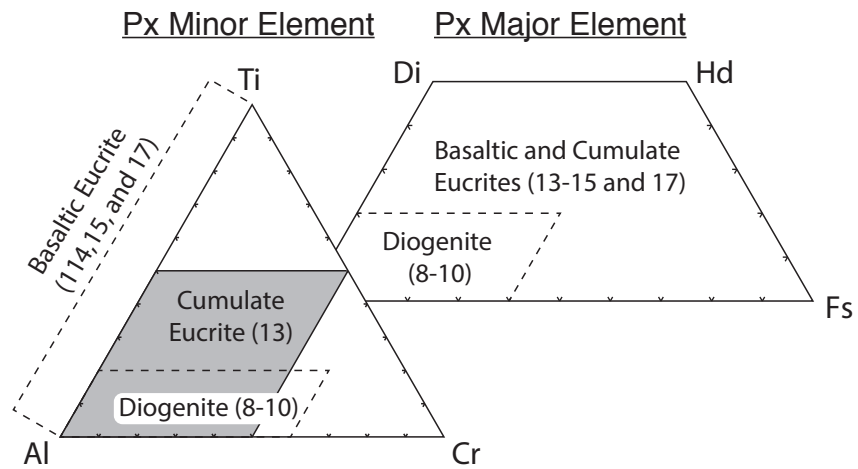


Figure 3.8. Pyroxene compositions for the DOM 10 howardites. The compositions span the complete range for the HED meteorite clan. Shown below is the key for subsequent figures that display major- and minor-element concentrations for pyroxenes. To maximize space, only a subset of the diagram is shown for different HED lithologies.

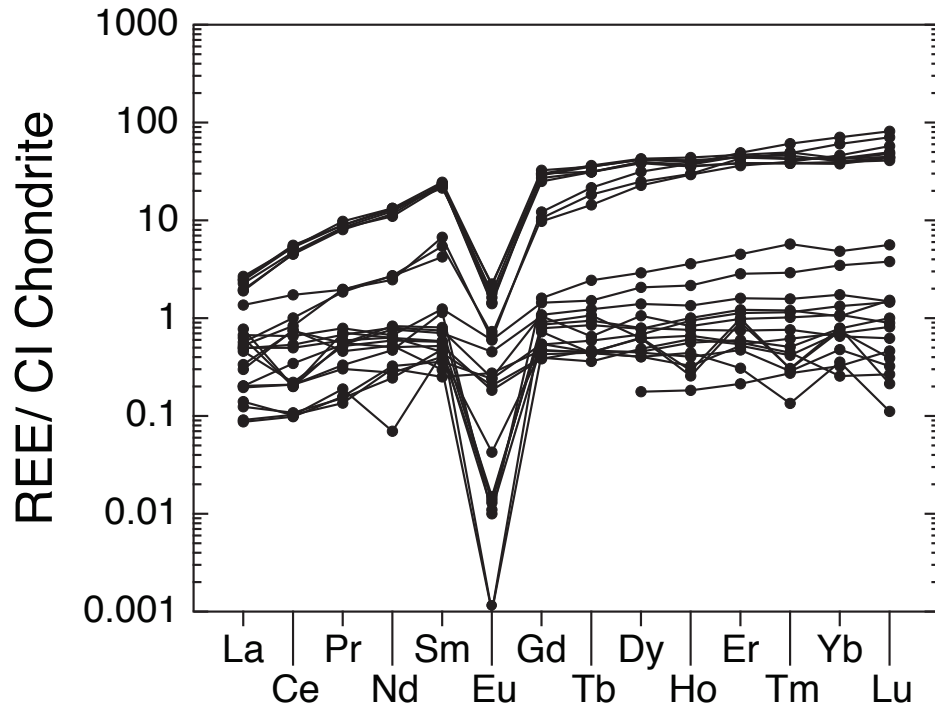


Figure 3.9 Rare earth-element chemistry of select pyroxenes in the DOM 10 howardites. Pyroxene trace-element compositions are consistent with eucritic and diogenitic meteorites; however, anomalies are observed, such as REE-enriched pyroxenes in some basaltic eucrite clasts. Data are normalized to CI chondrites (Anders & Grevesse, 1989).

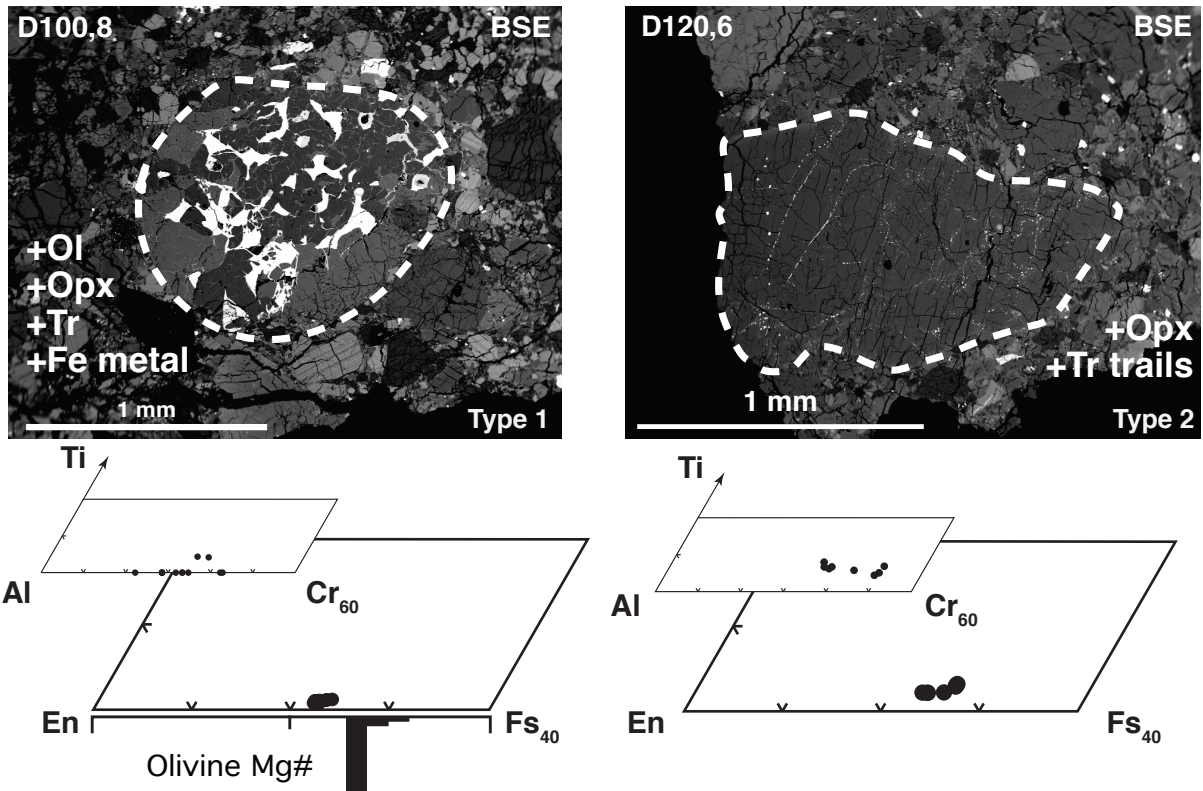


Figure 3.10. Examples of types 1 and 2 diogenite lithic clasts observed in the DOM 10 howardites. Insets show pyroxene major- and minor-element trends. Where appropriate, olivine composition (Mg#) is shown. See Figure 3.8 for key.

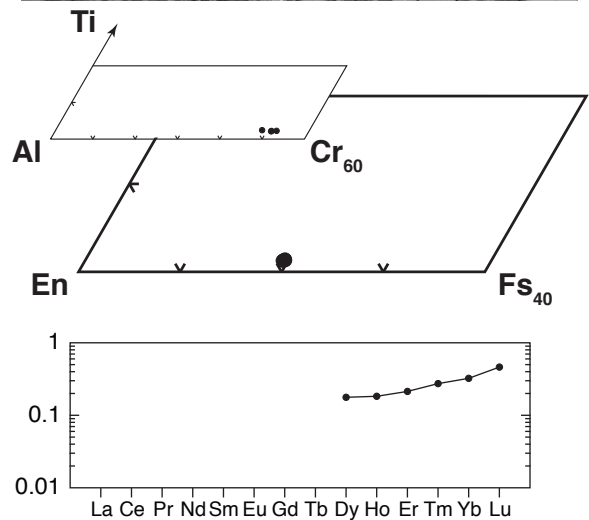
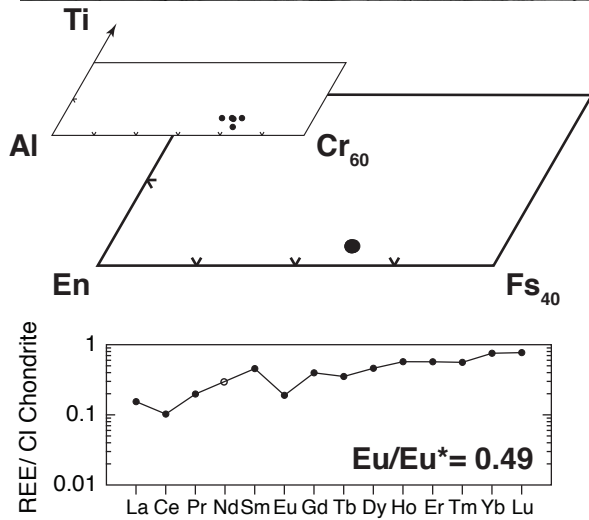
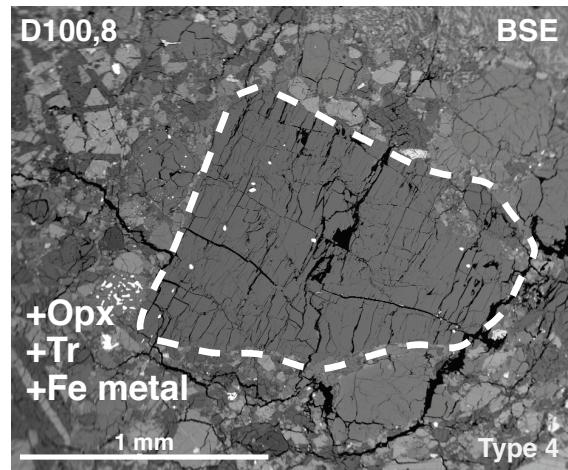
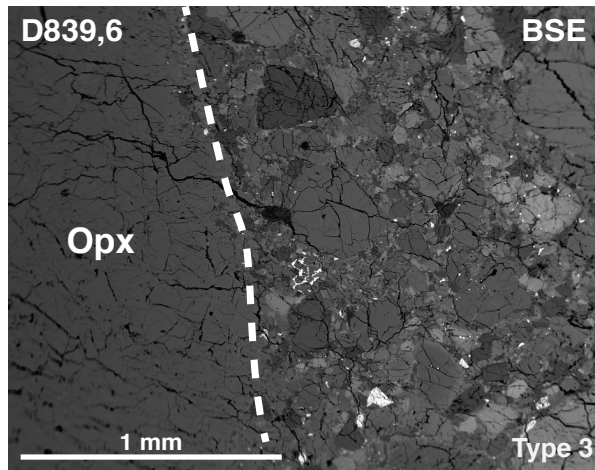


Figure 3.11. Examples of types 3 and 4 diogenite polycrystalline clasts are shown, along with pyroxene major- and minor-element compositions. Pyroxene REE patterns are shown below the corresponding lithology. REE data are normalized to CI chondrites (Anders & Grevesse, 1989). See Figure 3.8 for key.

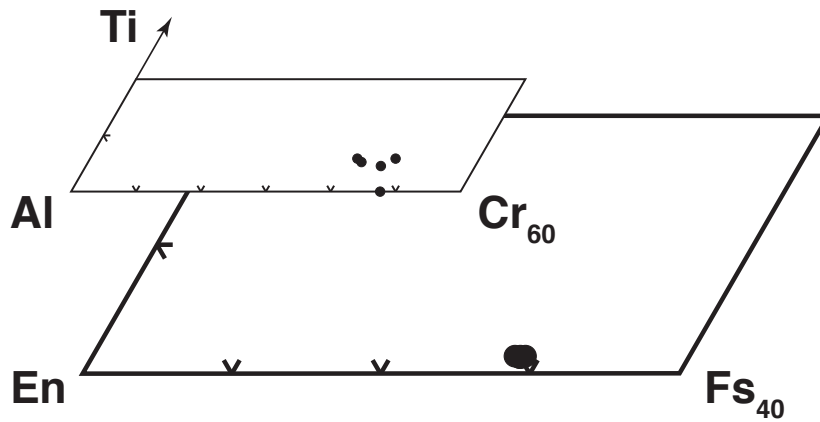
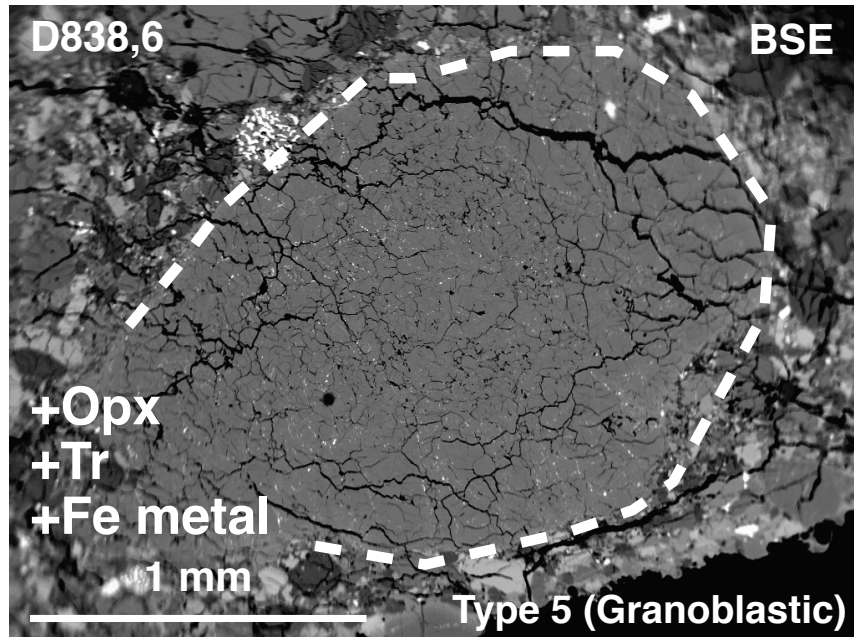


Figure 3.12. Type 5 diagenite polymineralic lithic clast example. Pyroxene major- and minor-element composition are shown below. Granoblastic textures are not shown in this figure because BSE images display composition, and do not highlight textures in the absence of compositional heterogeneity. See Figure 3.8 for key.

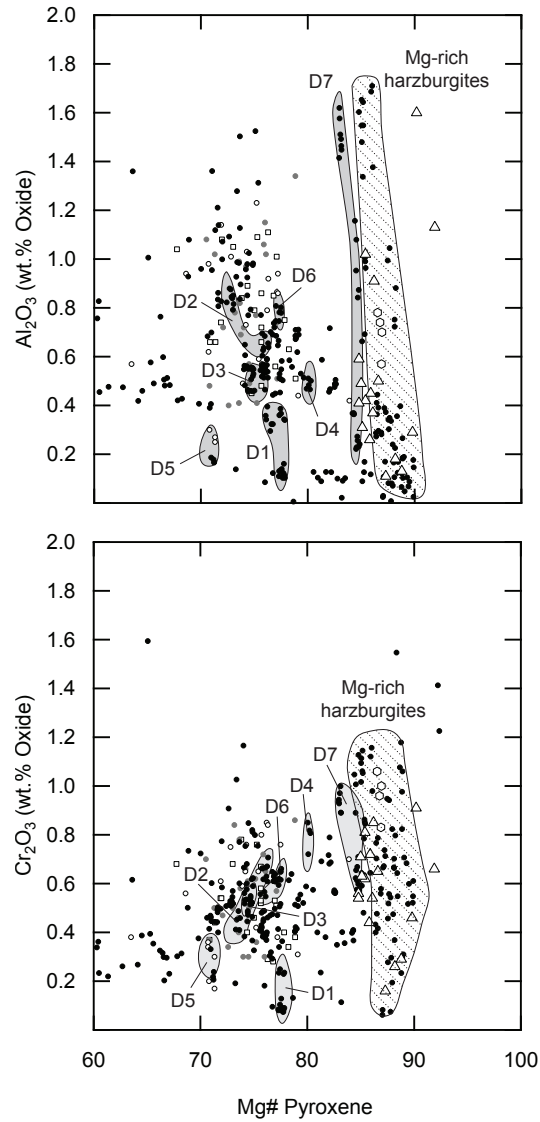


Figure 3.13. Minor-element concentrations vs. Mg# in diogenite pyroxenes. Variations in minor-element chemistry can be used to distinguish lithologies. Specifically, Al₂O₃ and Cr₂O₃ are more useful for classification because they exhibit large variations. Compositional range for individual diogenite types shown in figure. Outliers indicate that more diversity exists; however, without additional mineralogical or textural information, it is difficult to distinguish between discrete lithologies and continuous compositional trends.

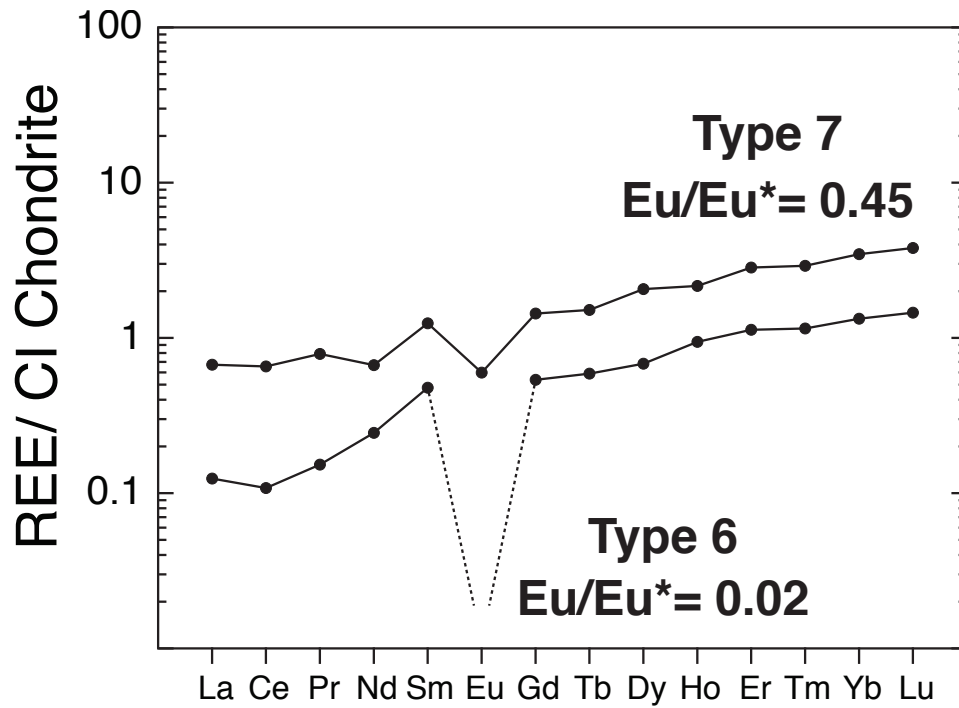


Figure 3.14. Rare earth element patterns for diogenite mineral fragments (types 6 and 7). Note the large variations in Eu anomalies, suggesting plagioclase crystallized from diogenite parent magmas, but to various extents. Data are normalized to CI chondrites (Anders & Grevesse, 1989)

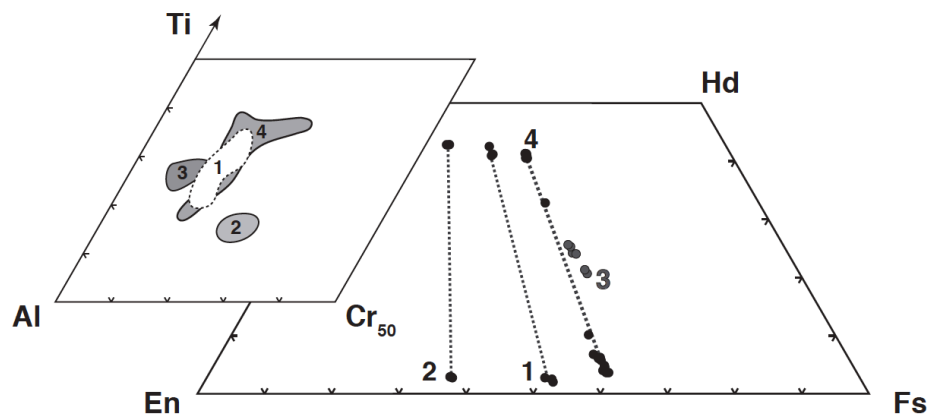
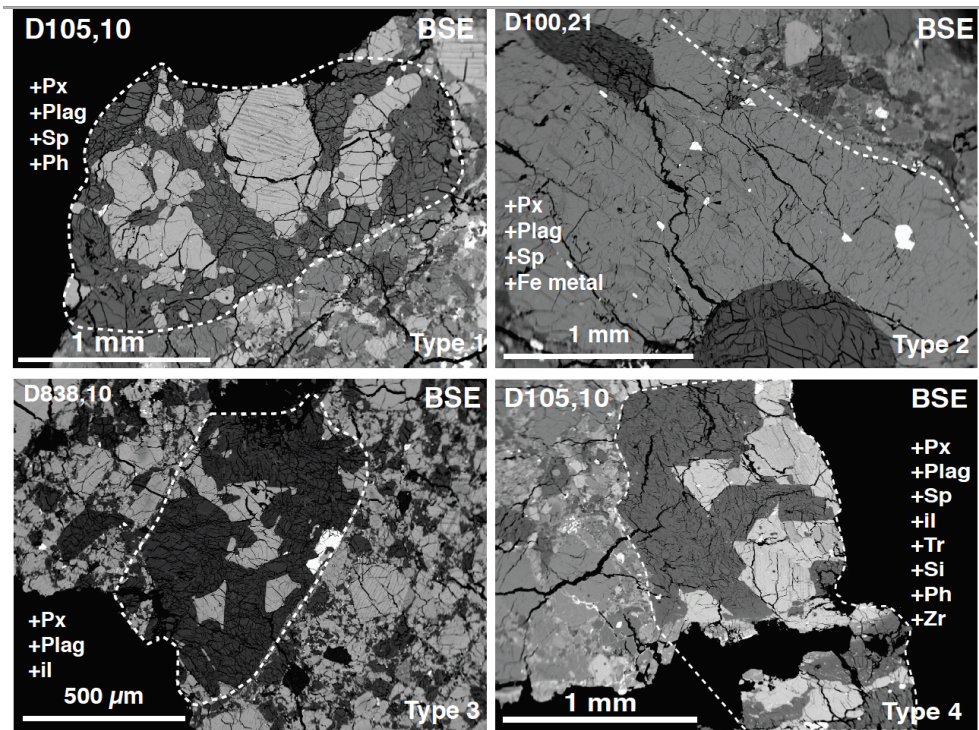


Figure 3.15. Examples of cumulate eucrite lithic clasts. Corresponding pyroxene end-member and minor-element concentrations are shown below. To reduce clutter, only end-member compositions that define the tie-line are shown, as analyses in between are caused by beam overlap in EPMA. Type 1 cumulate eucrites display cumulate textures and pyroxene compositions consistent with typical cumulate eucrites. Type 2 cumulate eucrite contains pyroxene compositions consistent with more Mg-rich cumulate eucrites; however, cumulate textures are less obvious. Fe-rich cumulate eucrite lithic clasts (types 3 and 4) are found, for which the composition of pyroxenes lies within the basaltic eucrite field; however, obvious cumulate textures are observed. We therefore classify these samples as cumulate eucrites based on textural considerations, rather than compositional. See Figure 3.8 for key.

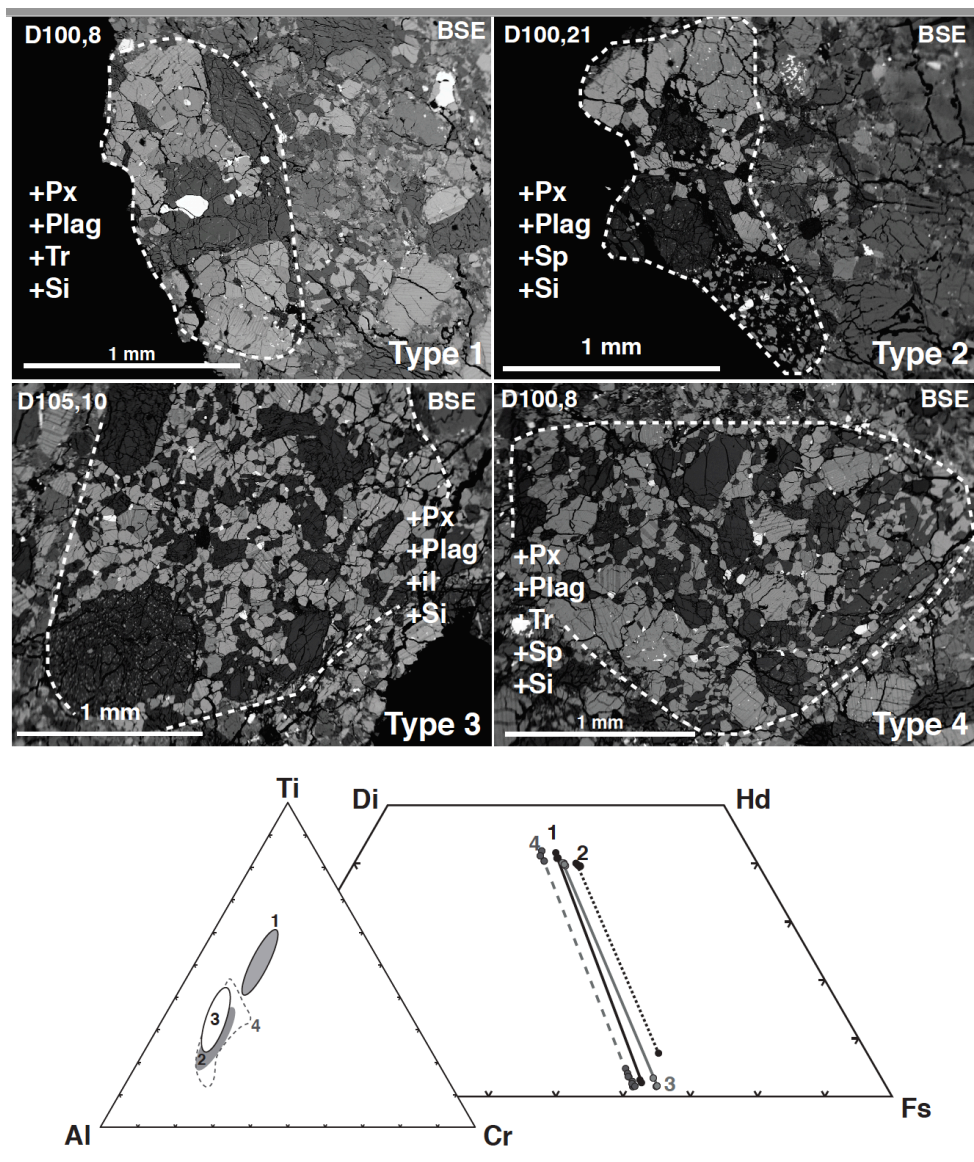


Figure 3.16. Basaltic eucrite lithic clasts with granoblastic textures (types 1 through 4). Pyroxene major- and minor-element compositions shown below. To reduce clutter, only end-member compositions that define the tie-line are shown, as analyses in between are caused by beam overlap in EPMA. See Figure 3.8 for key.

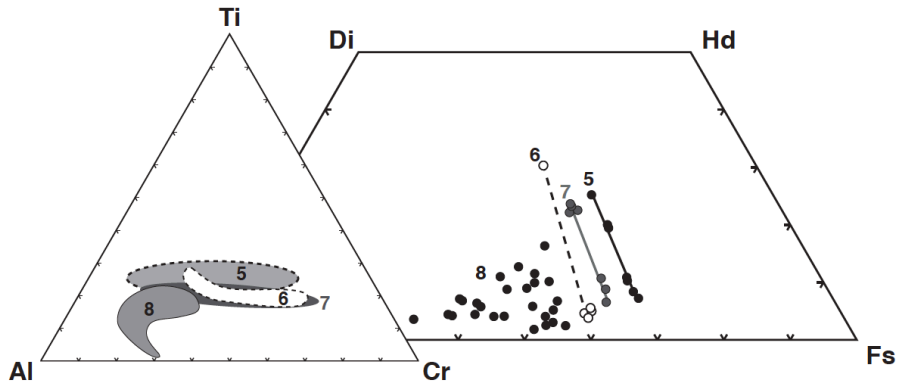
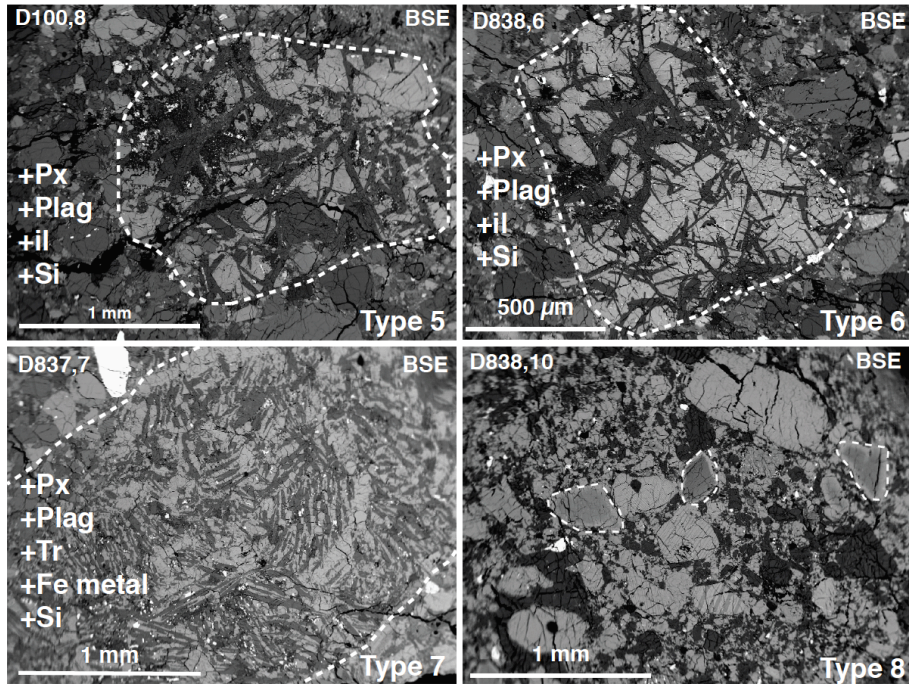


Figure 3.17. Types 5 through 8 basaltic eucrite lithic clasts and mineral fragments. Pyroxene major- and minor-element compositions are shown below. To reduce clutter, only end-member compositions that define the tie-line are shown, as analyses in between are caused by beam overlap on the EMP. Basaltic eucrite types 5 and 6 show subophitic and ophitic textures, respectively. Spherulitic textures are observed in the type 7 basaltic eucrite clasts. Basaltic eucrite type 8 is zoned, and only occurs as mineral fragments in section 10838,10. See Figure 3.8 for key.

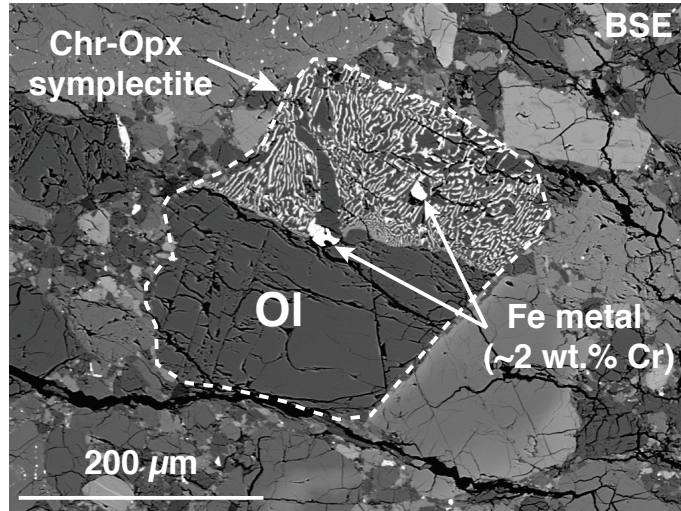


Figure 3.18. Example of harzburgitic-dunitic lithology identified by Hahn et al. (2018) in the DOM 10 howardites. This lithology is an assemblage of olivine, pyroxene, and Fe metal, with an associated chromite-orthopyroxene symplectite. The Mg#s for olivine and pyroxene within the clasts range from 82 to 92.

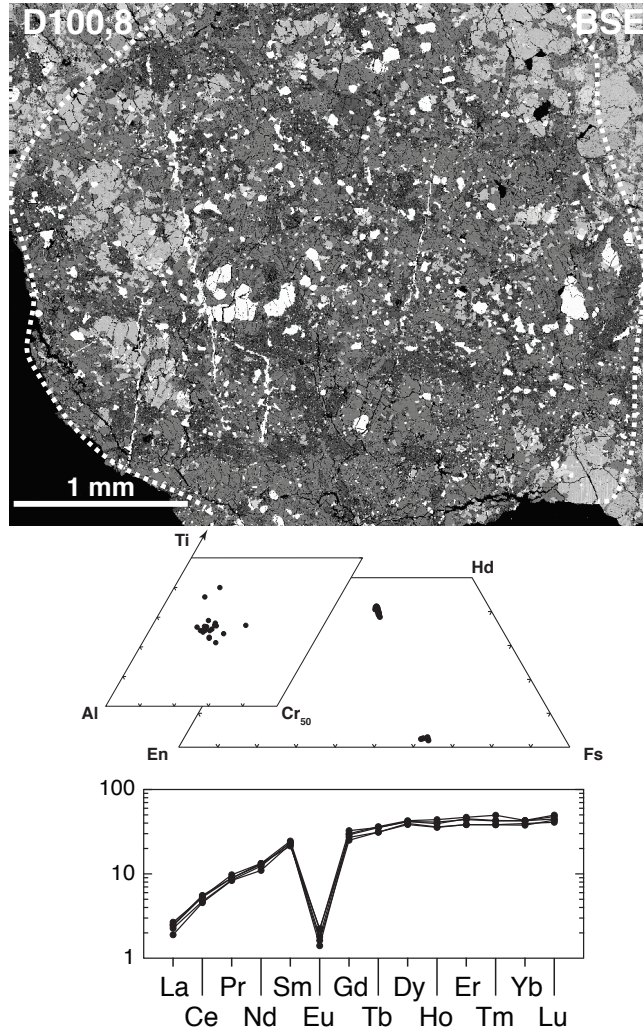


Figure 3.19. Dacite clast identified in the DOM 10 howardites by Hahn et al. (2017). The clast is dominated by plagioclase, quartz, and primary augite. Accessory Fe metal, ilmenite, phosphates, pigeonite, troilite, and K-feldspar are also observed. Pyroxene end-member and minor-element compositions, as well as REE data are shown below. This lithology is hypothesized to represent residual melt pockets in the vestan crust. Data for REEs were normalized to CI chondrites (Anders & Grevesse, 1989).

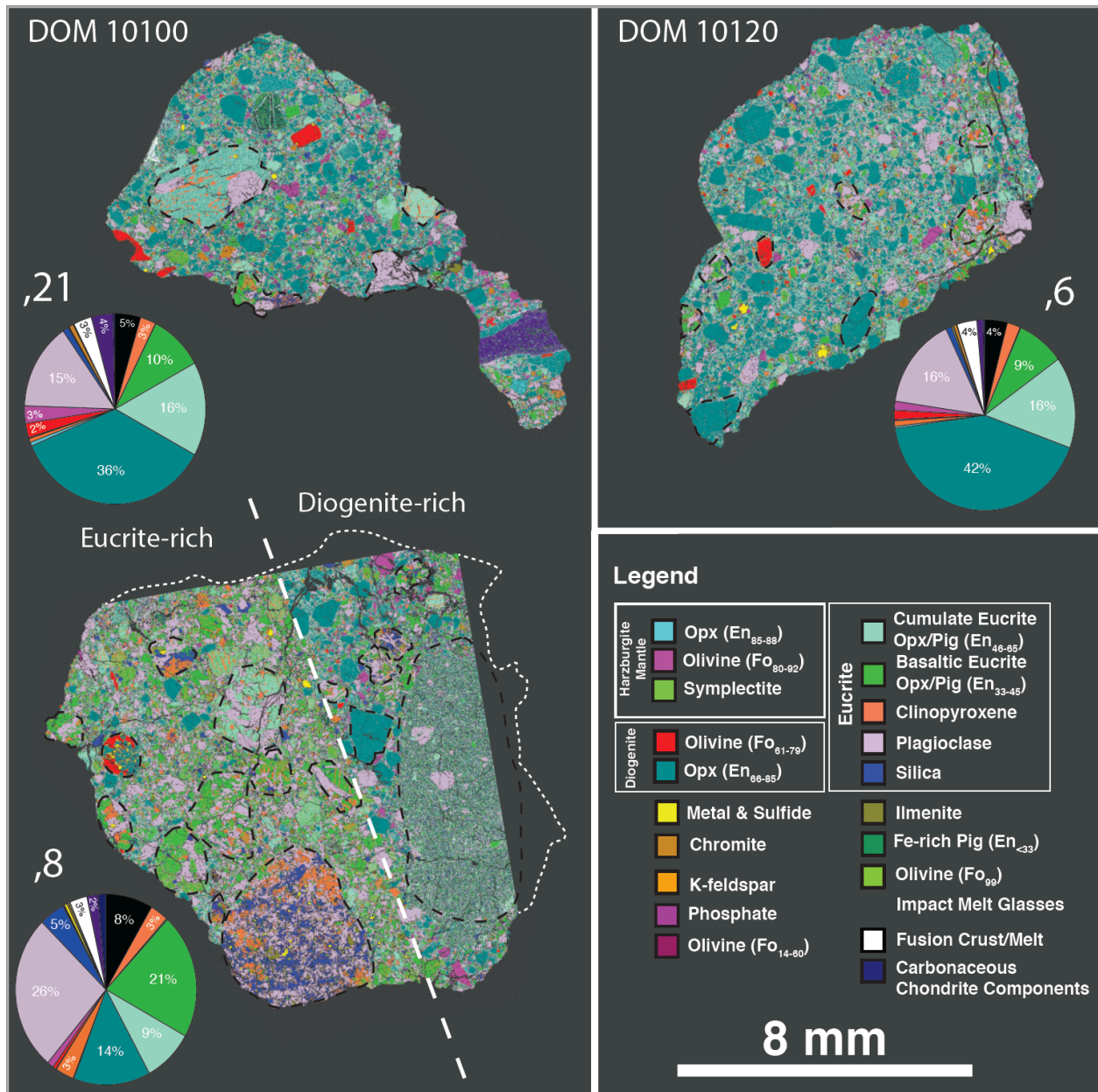


Figure 3.20. Lithologic distribution maps developed using a modified workflow of Beck et al. (2012). Shown here are maps created for DOM 10100 and 10120. A pie chart corresponding to each section displays the modal abundance of minerals within the section. Note that section 10100,8 contains a clear division between eucrite- and diogenite-rich areas; this indicates that sample is a breccia-within-breccia.

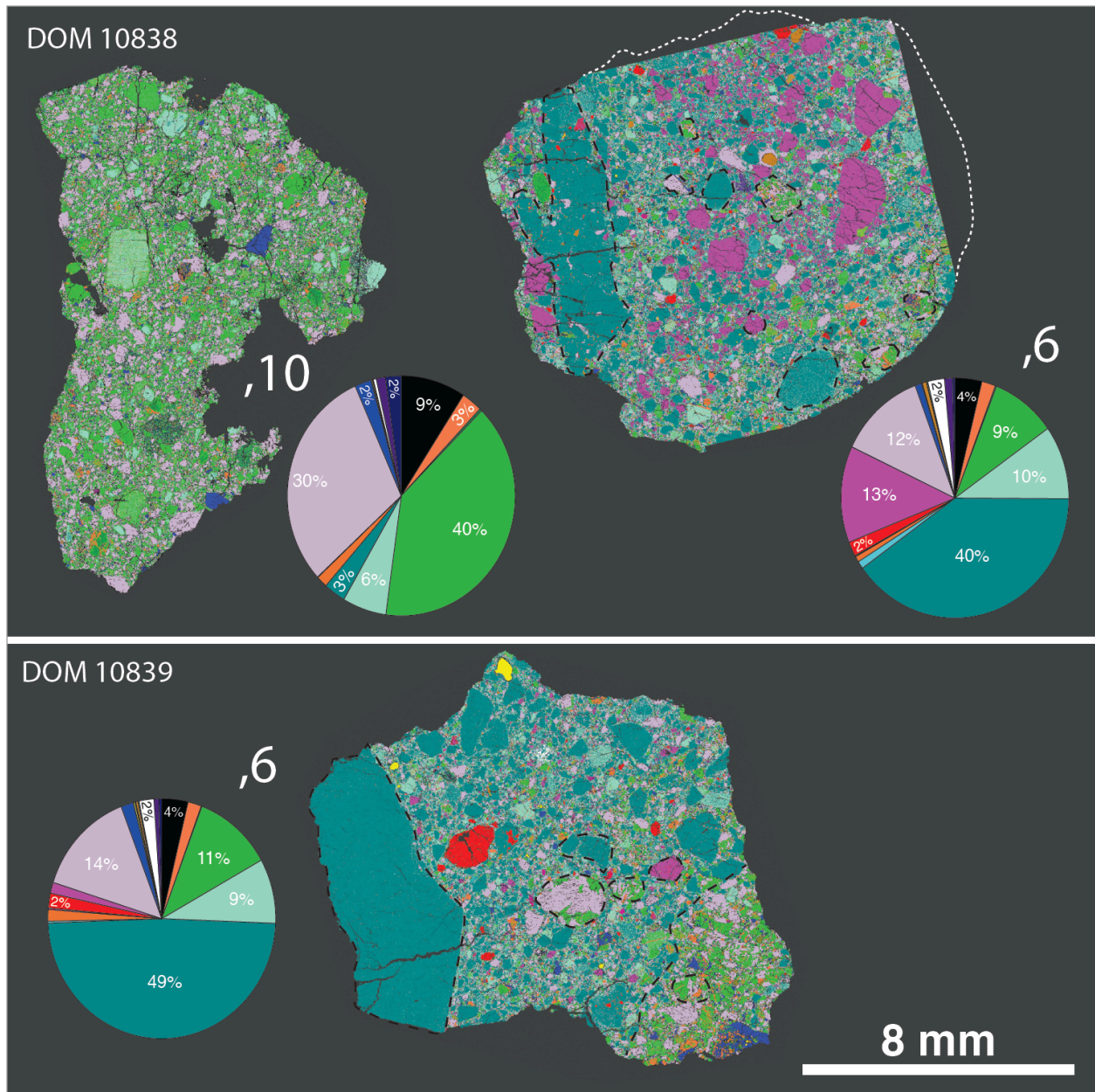


Figure 3.21. Lithologic distribution maps for DOM 10838 and 10839. Corresponding legend is shown in Fig. 3.20. Note that 10839,6 contains eucrite- and diogenite-rich areas; the eucrite-rich breccia clast is found in the lower right portion of the section. The two sections cut from 10838 contain large intra-sample variations in mineralogy (i.e. 9% and 40% basaltic eucrite in 10838,6 and 10838,10, respectively). Section 10838,6 also contains a large (>8 mm) breccia clast with only diogenitic minerals (left).

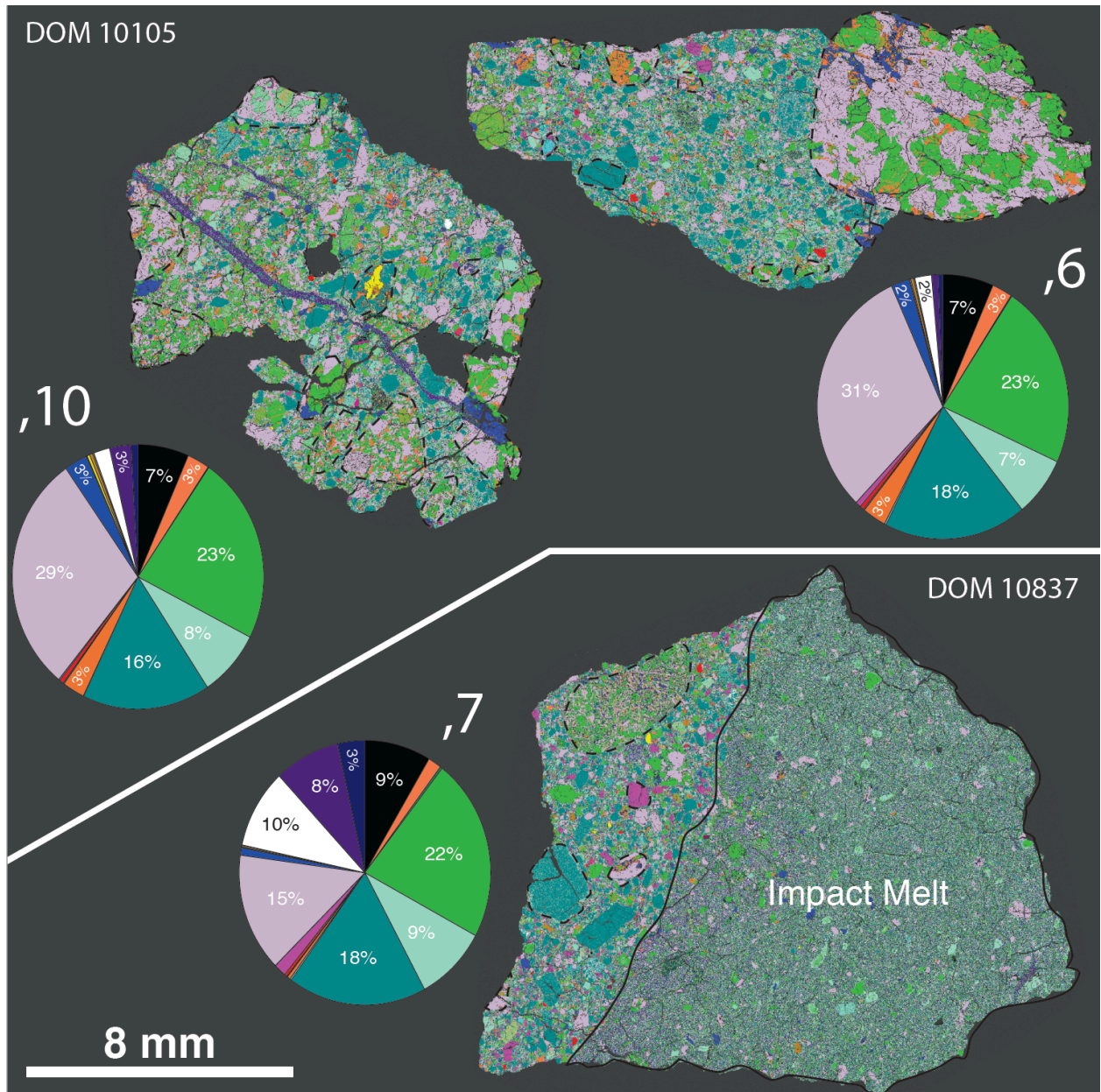


Figure 3.22. Lithologic distribution maps for DOM 10105 and 10837. Section 10837,7 is dominated by a clast-laden impact melt.

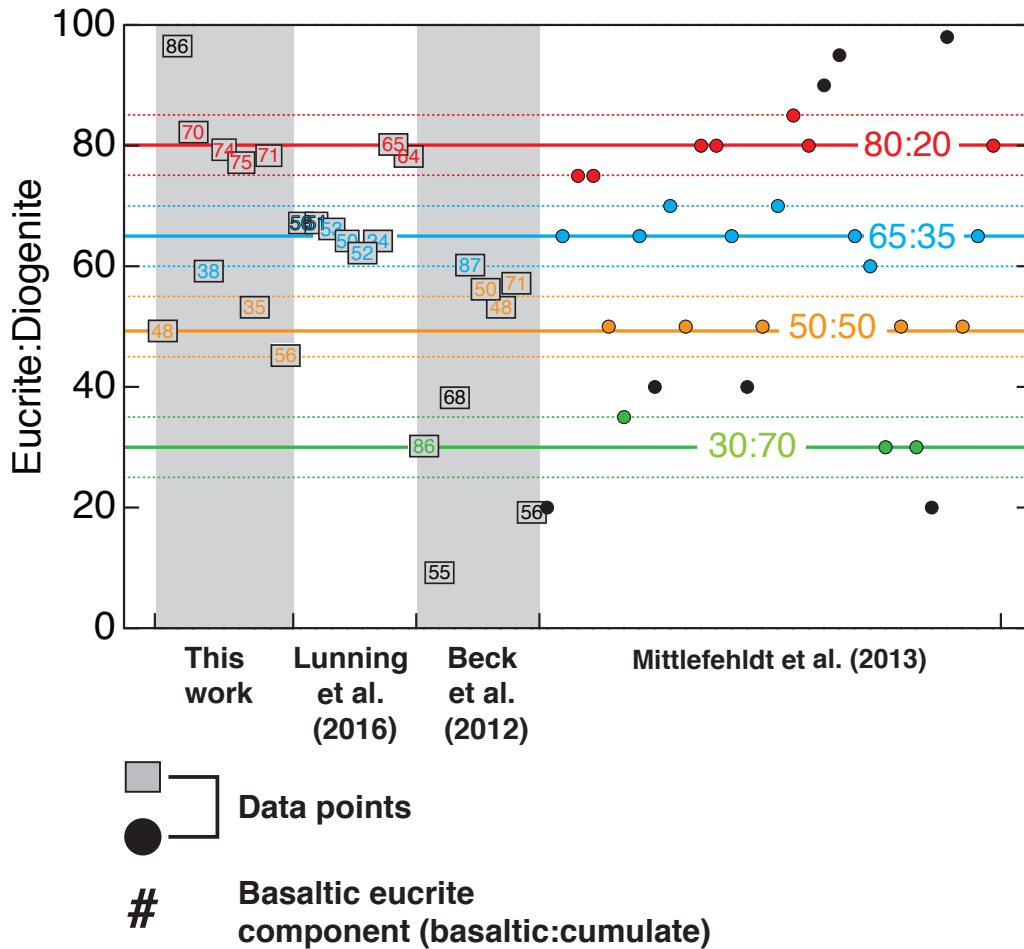


Figure 3.23. Calculated ratios of the abundances of eucrite to diogenite for various HEDs, with corresponding basaltic eucrite to cumulate eucrite ratios shown as a number inside each data point. Eucrite:diogenite ratios for Mittlefehldt et al. (2013) were calculated from petrographic and bulk chemical analysis, and the basaltic eucrite:cumulate eucrite ratio cannot be determined. Solid colored lines depict average eucrite:diogenite ratios that appear frequently, and may represent original values of various source terrains. Data values shown in black fall between the common ratios, which may be the result of error or misrepresentation of the data due to large clasts that dominated thin sections (i.e. DOM 10105,6; Fig. 3.22).

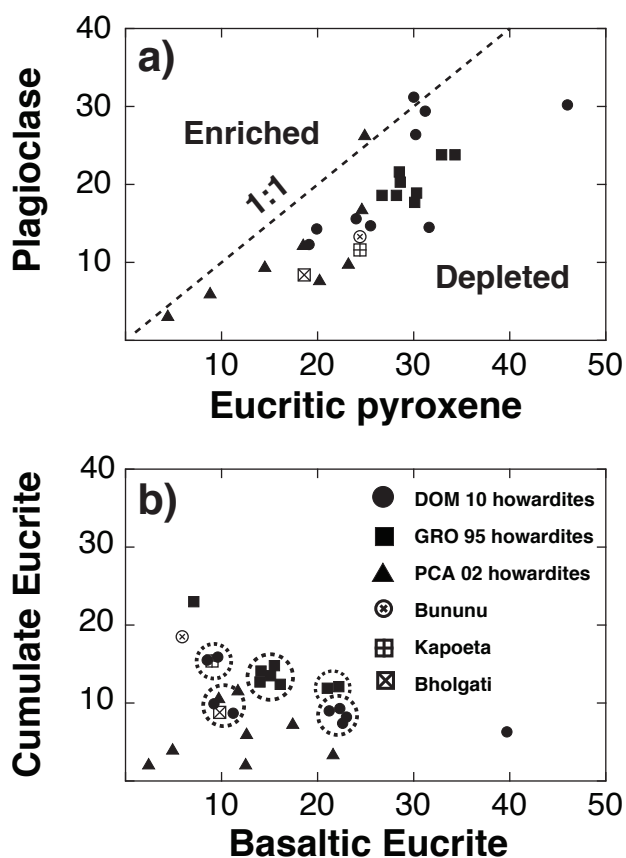


Figure 3.24. a) Plot of plagioclase vs. euclitic pyroxene in thin-sections from the DOM 10, PCA 02, and GRO 95 howardite pairing groups. The large regolithic howardites Bununu, Kapoeta, and Bholgati are also shown. Only a few sections appear to contain plagioclase and euclitic pyroxenes in the same ratio as in unbrecciated eucrites (1:1, Mayne et al. 2009); all others are depleted in plagioclase relative to euclitic pyroxene. b) Cumulate vs. basaltic eucrite abundances in the same meteorites. Sections from each pairing group appear to cluster around particular values, possibly reflecting original ratios before brecciation. Data for PCA 02 howardites from Beck et al. (2012), and for all other howardites from Lunning et al. (2016).

Tables

Table 3.1. Summary of attributes for howardite pairing groups.

Meteorite	Section	Group	Subgroup	Dimensions (cm)	Weight (g)	Paired?	Reference
DOM 10100	,8	Howardite	Fragmental	6.5 x 7.0 x 5.0	426.0	✓	[1] and this study
-	,21						[1] and this study
DOM 10838	,10	Eucrite ^a	Brecciated	2.75 x 3.0 x 2.5	31.9	✓	[1] and this study
-	,6	Howardite ^b	Fragmental				[1] and this study
DOM 10105	,6	Howardite	Fragmental	4.0 x 3.5 x 2.25	40.9	✓	[1] and this study
-	,10						[1] and this study
DOM 10120	,6	Howardite	Fragmental	5.0 x 3.0 x 3.0	65.7	✓	[1] and this study
DOM 10837	,7	Howardite	Fragmental	7.5 x 6.0 x 5.0	471.4	✓	[1] and this study
DOM 10839	,6	Howardite	Fragmental	4.0 x 3.75 x 2.5	58.7	✓	[1] and this study
DOM 10103		Eucrite	Brecciated	6.0 x 3.0 x 3.0	71.6	?	[1]
DOM 10350		Diogenite	Unbrecciated	3.5 x 2.5 x 2.0	27.3	?	[2]
GRO 95534	,4	Howardite	Regolithic	3.0 x 2.7 x 1.5	17.9	✓	[3]
GRO 95535	,11	Howardite	Regolithic	3.2 x 2.5 x 2.7	53.8	✓	[3]
-	,16						[3]
GRO 95574	,17	Howardite	Regolithic	5.5 x 3.5 x 3.0	90.6	✓	[3]
GRO 95581	,7	Howardite	Regolithic	4.0 x 2.0 x 2.5	49.4	✓	[3]
-	,14						[3]
GRO 95602	,10	Howardite	Regolithic	4.3 x 3.6 x 1.0	51.5	✗	[3]
-	,13						[3]
GRO 95633	,2	Howardite	Regolithic	4.7 x 2.5 x 3.0	58.1	✗	[3]
GRO 95522	,18	Eucrite	Unbrecciated	13.7 x 7.1 x 5.8	613.2	✗	[3]
PCA 02009	,7	Howardite	Fragmental	3.0 x 2.0 x 2.2	22.5	✓	[4]
-	,12						[4]
PCA 02013	,6	Howardite	Fragmental	5.0 x 3.0 x 2.2	41.0	✓	[4]
-	,9						[4]
PCA 02014	,6	Howardite	Fragmental	3.5 x 2.5 x 1.5	21.2	✓	[4]
PCA 02015	,4	Howardite	Fragmental	3.5 x 2.5 x 1.5	16.8	✓	[4]
-	,7						[4]
PCA 02018	,4	Howardite	Fragmental	2.0 x 1.2 x 1.0	3.1	✓	[4]
PCA 02019	,4	Howardite	Fragmental	2.5 x 2.5 x 1.5	11.7	✓	[4]
PCA 02008	,8	Diogenite	Fragmental	3.0 x 2.0 x 2.0	19.1	✓	[5]

^aClassification determined during this study by modal analysis.

^bInitial classification given to DOM 10838

¹Corrigan et al. (2011)

²Mittlefehldt et al. (2015)

³Lunning et al. (2016)

⁴Beck et al. (2012)

⁵Beck et al. (2010)

Table 3.2 Composition fo DOM 10 howardite fused beads

	DOM		DOM		DOM		DOM		DOM		DOM		BHVO-1	
	10100,27		10837,16		10100,24		10120,15		10120,12		10100,22		2	
beads	4		4		2		3		1		2		2	
n	20	$\pm 1\sigma$	27	$\pm 1\sigma$	12	$\pm 1\sigma$	19	$\pm 1\sigma$	4	$\pm 1\sigma$	15	$\pm 1\sigma$	15	$\pm 1\sigma$
Na ₂ O	0.24	0.01	0.37	0.04	0.08	0.04	0.15	0.01	0.11	0.01	0.26	0.02	2.24	0.04
MgO	17.4	0.33	13.5	0.95	22.9	1.17	20.6	0.26	21.9	0.12	16.9	0.45	6.83	0.08
Al ₂ O ₃	7.04	0.43	8.85	1.29	2.65	1.15	5.16	0.26	3.84	0.23	7.24	0.78	13.5	0.08
SiO ₂	49.0	0.49	48.7	0.61	52.0	1.65	49.6	0.32	50.6	0.23	49.0	0.41	48.6	0.23
MnO	0.51	0.02	0.53	0.03	0.56	0.02	0.51	0.02	0.56	0.01	0.54	0.03	0.17	0.01
FeO	16.7	0.42	17.9	0.83	16.9	0.37	16.7	0.28	16.8	0.42	17.9	0.28	10.5	0.10
K ₂ O	0.02	0.01	0.05	0.01	0.01	0.01	0.02	0.01	0.01	0.01	0.03	0.01	0.51	0.02
P ₂ O ₅	0.04	0.01	0.06	0.05	0.01	0.01	0.02	0.01	0.01	0.01	0.02	0.01	0.28	0.03
NiO	<0.02	0.01	<0.02		<0.02		<0.02		<0.02		<0.02		<0.02	
Cr ₂ O ₃	0.59	0.02	0.48	0.04	0.68	0.04	0.87	0.06	0.70	0.04	0.95	0.12	0.04	0.01
TiO ₂	0.33	0.02	0.55	0.07	0.14	0.05	0.22	0.03	0.17	0.04	0.31	0.07	2.70	0.05
CaO	5.70	0.16	7.49	0.29	2.46	0.74	4.32	0.10	3.14	0.25	5.42	0.23	11.0	0.06
SO ₃	0.21	0.06	0.28	0.16	0.22	0.07	0.29	0.06	0.20	0.10	0.45	0.14	0.01	0.01
MoO ₃	1.52	0.75	0.65	0.56	0.66	1.09	0.97	0.51	0.98	1.15	0.40	0.60	2.35	0.44
TOTAL	99.3	0.22	99.4	0.22	99.3	0.34	99.4	0.30	99.0	0.09	99.4	0.24	98.7	0.27

Table 3.3 Composition fo DOM 10 howardite fused beads (Mo-free basis)

	DOM		DOM		DOM		DOM		DOM		DOM		BHVO-1	
	10100,27		10837,16		10100,24		10120,15		10120,12		10100,22		2	
beads	4		4		2		3		1		2		2	
n	20	$\pm 1\sigma$	27	$\pm 1\sigma$	12	$\pm 1\sigma$	19	$\pm 1\sigma$	4	$\pm 1\sigma$	15	$\pm 1\sigma$	15	$\pm 1\sigma$
Na ₂ O	0.24	0.01	0.38	0.04	0.08	0.04	0.15	0.01	0.11	0.01	0.26	0.02	2.32	0.04
MgO	17.8	0.33	13.6	0.95	23.3	1.17	21.0	0.26	22.4	0.12	17.1	0.45	7.09	0.08
Al ₂ O ₃	7.19	0.43	8.97	1.29	2.68	1.15	5.24	0.26	3.92	0.23	7.31	0.78	14.0	0.08
SiO ₂	50.1	0.49	49.4	0.61	52.7	1.65	50.4	0.32	51.6	0.23	49.5	0.41	50.4	0.23
MnO	0.52	0.02	0.54	0.03	0.57	0.02	0.52	0.02	0.57	0.01	0.55	0.03	0.17	0.01
FeO	17.1	0.42	18.1	0.83	17.2	0.37	16.9	0.28	17.1	0.42	18.0	0.28	10.9	0.10
K ₂ O	0.03	0.01	0.05	0.01	0.01	0.01	0.02	0.01	0.01	0.01	0.03	0.01	0.53	0.02
P ₂ O ₅	0.04	0.01	0.07	0.05	0.01	0.01	0.02	0.01	0.01	0.01	0.02	0.01	0.29	0.03
NiO	<0.02	0.01	<0.02		<0.02		<0.02		<0.02		<0.02		<0.02	
Cr ₂ O ₃	0.60	0.02	0.49	0.04	0.69	0.04	0.89	0.06	0.71	0.04	0.96	0.12	0.04	0.01
TiO ₂	0.33	0.02	0.55	0.07	0.14	0.05	0.23	0.03	0.17	0.04	0.31	0.07	2.80	0.05
CaO	5.83	0.16	7.59	0.29	2.49	0.74	4.39	0.10	3.21	0.25	5.47	0.23	11.4	0.06
SO ₃	0.21	0.06	0.28	0.16	0.22	0.07	0.29	0.06	0.20	0.10	0.46	0.14	0.01	0.01

Table 3.4. Bulk geochemistry of DOM 10 howardite subsamples determined by INAA

Sample	Reference	Method	POEM _{Ca}	Na mg/g	K ppm	Ca mg/g	Sc ppm	Cr mg/g	Fe mg/g	Co ppm	Ni ppm	Zn ppm	Br ppb	Rb ppb	Sr ppm	Zr ppm	Cs ppb
Dacite_1	Hahn et al. 2018	Calculated		5.20	830	80.0									155		
Dacite_2	Hahn et al. 2018	Calculated		5.20	1660	87.0									155		
DOM 10837,14	This Study	INAA	92.3	4.18	602	69.1	32.4	2.18	153	3.69	17.3	b.d.	150	701	85.7	87.0	2.01
DOM 10837,16	This Study	INAA	44.1	1.86	b.d.	38.1	21.4	4.40	134	18.3	106	1.03	b.d.	2724	95.6	29.8	18.4
DOM 10837,13	This Study	INAA	40.2	1.58	1314	35.6	20.3	5.17	134	22.5	213	1.65	11.4	1676	43.9	21.8	18.2
DOM 10120,12	This Study	INAA		0.39	b.d.	8.9	15.1	5.50	136	21.4	21.9	0.04	361	52.9	16.8	b.d.	0.57
DOM 10120,13	This Study	INAA	35.8	1.46	b.d.	32.8	19.1	6.97	133	24.9	147	0.57	26.5	77.7	29.3	23.8	13.8
DOM 10120,15	This Study	INAA	25.2	1.15	b.d.	26.0	17.6	6.29	136	33.9	152	0.23	185	1549	25.6	27.0	0.40
DOM 10105,11	This Study	INAA	44.5	1.73	262	38.4	23.6	5.17	141	17.7	80.3	b.d.	218	2744	71.6	9.34	1.93
DOM 10105,14	This Study	INAA	86.1	3.26	440	65.2	28.9	2.92	129	11.6	65.5	b.d.	187	2756	63.4	46.4	1.21
DOM 10105,12	This Study	INAA	61.1	2.55	b.d.	49.1	26.3	4.51	146	14.2	40.8	b.d.	104	2255	38.3	61.3	1.07
DOM 10839,9	This Study	INAA	58.5	2.68	b.d.	47.4	23.8	3.80	136	17.2	80.3	b.d.	248	2694	70.7	112	16.6
DOM 10839,7	This Study	INAA	46.7	2.09	b.d.	39.8	22.0	4.61	136	15.2	67.7	b.d.	89.3	124	34.0	41.4	0.47
DOM 10839,8	This Study	INAA		0.16	b.d.	7.6	13.3	13.1	129	14.8	16.1	0.08	60.8	80.1	1.33	b.d.	0.71
DOM 10838,11	This Study	INAA	30.0	1.33	b.d.	29.0	18.9	7.27	134	19.1	73.1	0.21	140	2013	32.1	31.1	8.65
DOM 10838,12	This Study	INAA	42.9	1.82	b.d.	37.4	20.5	5.23	133	16.5	50.2	0.00	43.9	2248	40.6	b.d.	1.38
DOM 10838,14	This Study	INAA	72.3	3.02	1281	56.3	27.1	3.13	135	7.89	26.1	0.68	422	2189	64.5	103	2.47
DOM 10100,23	This Study	INAA	26.7	1.31	b.d.	26.9	18.4	7.98	130	17.5	76.7	0.89	3.68	73.6	49.7	33.1	0.59
DOM 10100,26	This Study	INAA	40.8	1.56	b.d.	36.0	21.2	5.54	136	20.6	90.3	3.02	100	1604	39.5	26.7	1.75
DOM 10100,22	This Study	INAA	28.7	1.62	b.d.	28.2	20.7	7.46	149	23.5	51.6	1.22	24.7	324	59.8	38.7	2.51
DOM 10100,24	This Study	INAA	18.0	1.21	b.d.	21.3	17.0	7.55	129	18.9	85.3	0.72	39.7	2635	46.8	30.2	1.14
DOM 10100,27	This Study	INAA	46.6	1.86	b.d.	39.7	20.8	4.33	136	27.6	132	4.28	18.7	2067	85.4	14.1	1.42
BHVO-1	This Study	INAA		16.9	3858	75.0	31.1	0.29	85.2	44.5	124	85.1	51.1	9504	426	208	63.7

Table 3.4. Bulk geochemistry of DOM 10 howardite subsamples determined by INAA (continued).

Sample	Reference	Method	POEM _{Ca}	Ba ppm	La ppm	Ce ppm	Nd ppm	Sm ppm	Eu ppm	Tb ppm	Yb ppm	Lu ppm	Hf ppm	Ta ppb	Ir ppb	Au ppb	Th ppb	U ppb
Dacite_1	Hahn et al. 2018	Calculated		11.8	29.4		6.60				3.91	0.56						
Dacite_2	Hahn et al. 2018	Calculated		11.8	29.4		6.60				3.91	0.56						
DOM 10837,14	This Study	INAA	92.3	34.0	3.67	8.96	7.38	2.29	0.72	0.56	2.30	0.34	1.69	238	0.11	0.97	382	29.9
DOM 10837,16	This Study	INAA	44.1	26.7	3.21	7.07	6.35	1.49	0.35	0.31	1.06	0.16	0.71	119	3.06	0.85	338	####
DOM 10837,13	This Study	INAA	40.2	11.9	1.29	3.57	2.47	0.85	0.26	0.20	0.85	0.12	0.59	61.2	5.18	2.28	136	25.8
DOM 10120,12	This Study	INAA		3.00	0.23	0.51	0.46	0.15	0.06	0.03	0.20	0.03	0.12	8.9	0.43	0.62	18.7	27.0
DOM 10120,13	This Study	INAA	35.8	19.4	1.17	3.27	2.59	0.76	0.26	0.17	0.73	0.11	0.49	51.4	6.88	1.90	115	9.80
DOM 10120,15	This Study	INAA	25.2	13.5	0.98	2.04	2.78	0.67	0.22	0.17	0.65	0.10	0.42	107	5.60	1.96	87.0	5.04
DOM 10105,11	This Study	INAA	44.5	18.8	1.57	4.96	3.49	1.08	0.31	0.27	1.07	0.16	0.75	104	4.78	0.91	154	####
DOM 10105,14	This Study	INAA	86.1	33.6	2.80	7.69	6.56	1.93	0.60	0.46	1.80	0.26	1.40	164	0.39	1.33	320	55.0
DOM 10105,12	This Study	INAA	61.1	34.7	2.56	6.61	5.22	1.74	0.49	0.40	1.72	0.26	1.44	152	2.72	1.91	294	68.5
DOM 10839,9	This Study	INAA	58.5	27.4	3.29	9.06	3.21	2.06	0.52	0.46	1.70	0.24	1.18	148	2.35	1.42	400	31.2
DOM 10839,7	This Study	INAA	46.7	31.4	1.99	4.92	3.94	1.25	0.39	0.30	1.20	0.17	0.85	111	2.09	0.65	197	38.8
DOM 10839,8	This Study	INAA		b.d.	0.13	0.43	0.04	0.09	0.02	0.03	0.16	0.03	0.11	7.16	0.64	0.28	0.4	2.09
DOM 10838,11	This Study	INAA	30.0	12.0	1.30	3.59	2.45	0.83	0.24	0.21	0.80	0.12	0.51	59.2	3.02	1.36	133	66.5
DOM 10838,12	This Study	INAA	42.9	21.0	1.35	3.23	2.24	0.88	0.30	0.20	0.90	0.13	0.58	64.4	2.37	0.94	133	59.7
DOM 10838,14	This Study	INAA	72.3	32.2	2.75	7.22	6.22	1.78	0.54	0.42	1.66	0.24	1.29	192	1.23	1.62	335	71.2
DOM 10100,23	This Study	INAA	26.7	13.6	0.87	2.18	1.65	0.56	0.22	0.15	0.62	0.09	0.42	36.4	3.52	1.17	85.1	58.2
DOM 10100,26	This Study	INAA	40.8	12.9	1.23	3.25	1.97	0.84	0.28	0.20	0.87	0.13	0.52	99.4	2.23	1.36	145	15.2
DOM 10100,22	This Study	INAA	28.7	b.d.	1.62	4.51	3.53	1.04	0.29	0.23	0.91	0.14	0.67	112	3.84	0.96	194	13.3
DOM 10100,24	This Study	INAA	18.0	12.0	0.80	2.13	1.42	0.51	0.15	0.12	0.54	0.08	0.35	51.6	3.38	1.04	71.2	1.93
DOM 10100,27	This Study	INAA	46.6	7.17	1.48	3.44	2.40	0.89	0.31	0.23	0.94	0.14	0.74	81.8	4.89	2.58	181	40.6
BHVO-1	This Study	INAA		137	15.0	37.4	23.6	6.17	2.02	0.92	1.98	0.26	4.50	1120	0.19	1.65	1127	489

Table 3.5. Summary of lithologic diversity in the DOM 10 howardites.

Lithologic type	Phase	En	Wo	An	Texture	Identifying characteristics	Meteorite association
B1	Pig	36.2 (1)	2.74 (40)	74 to 83	Granoblastic	Px major- and minor-element composition; plagioclase composition	Haraiya (Takeda and Graham 1991)
	Cpx	29.4 (2)	41.3 (7)	-			
B2	Pig	31.1	8.45	79 to 83	Granoblastic	Px major-element composition	Nuevo Laredo (Warren and Jerde 1987)
	Cpx	26.8 (2)	39.9 (3)	-			
B3	Pig	35.8 (12)	3.70 (11)	86 to 90	Granoblastic	Px major-element and plagioclase composition	EET 90020 (Mayne et al. 2009)
	Cpx	29.8 (7)	40.2 (3)	-			
B4	Pig	36.3 (5)	2.6 (8)	85 to 90	Granoblastic	Px major-element and plagioclase composition	LEW 85353; LEW 85305 (Mayne et al. 2009)
	Cpx	29.6 (5)	41.9 (12)	-			
B5	Pig	28.5 (1)	14.6 (70)	81 to 84	Subophitic	Texture; Px and plagioclase major-element composition	Nuevo Laredo (Warren and Jerde 1987)
B6	Pig	37.8 (7)	5.18 (73)	83 to 88	Ophitic	Texture; Px major-element composition	PCA 82501 (Mayne et al. 2009)
	Cpx	31.8	30.8	-			
B7	Pig	32.9 (14)	16.1 (68)	77 to 98	Spherulitic	Texture and Px and plagioclase major-element composition	QUE 99658 (Mayne et al. 2009)
B8	Core	57.2 (37)	5.39 (13)	-	N/A	Zoned composition	None
	Rim	45.1 (35)	7.2 (42)	-			
C1	Pig	46.8 (9)	2.55 (38)	90 to 93	Granoblastic	Texture; pyroxene major- and minor-element composition	Moore County (Mayne et al. 2009)
	Cpx	35.5 (2)	41.6 (9)	-			
C2	Pig	60.7 (1)	3.02 (9)	94 to 95	Cumulate poikilitic	Texture; pyroxene major- and minor-element composition	Serra de Mage; Moama (Mayne et al. 2009)
	Cpx	41.3 (3)	42.9 (1)	-			

Table 3.6. Lithologies identified within each howardite thin-section.

Lithology	DOM 10838,6	DOM 10838,10	DOM 10100,8	DOM 10100,21	DOM 10105,10	DOM 10105,6	DOM 10120,6	DOM 10837,7	DOM 10839,6
B1			x		x				
B2			x	x			x		
B3			x		x				
B4			x		x				
B5			x						
B6	x								
B7								x	
B8		x							
C1		x	x	x	x			x	
C2				x					
C3		x							
C4			x		x	x			
D1			x						x
D2	x					x	x	x	
D3									x
D4			x						
D5	x								
D6									
D7									
Harzburgite	x		x	x	x	x	x	x	x
Dacite			x			x			

Table 3.7. Representative pyroxene and olivine compositions from diogenites in the DOM 10 howardites (wt.% oxide).

Type	D1		D2	D3	D4	D5	D6	D7
Phase	Px	Ol	Px	Px	Px	Px	Px	Px
	n=13	n=10	n=5	n=5	n=8	n=5	n=3	n=3
Oxide								
SiO ₂	55.2 (3)	37.5 (1)	54.3 (8)	54.0 (2)	54.6 (17)	54.1 (1)	54.5 (<1)	55.6 (1)
TiO ₂	<0.03	<0.03	0.08 (3)	0.07 (1)	0.09 (9)	n.d.	0.12 (1)	0.06 (1)
Al ₂ O ₃	0.23 (10)	<0.03	0.59 (7)	0.54 (2)	0.50 (24)	0.23 (3)	0.77 (3)	0.99 (2)
Cr ₂ O ₃	0.18 (10)	<0.03	0.59 (14)	0.60 (3)	0.74 (43)	0.30 (5)	0.64 (2)	0.85 (1)
FeO	14.9 (3)	24.8 (3)	16.7 (26)	15.8 (1)	15.2 (48)	18.6 (2)	14.4 (3)	9.48 (5)
MnO	0.62 (4)	0.56 (1)	0.54 (7)	0.55 (1)	0.51 (17)	0.63 (2)	0.44 (1)	0.36 (<1)
MgO	28.5 (4)	37.0 (1)	26.1 (19)	26.3 (1)	27.4 (42)	25.5 (1)	27.5 (1)	31.1 (1)
CaO	0.49 (10)	<0.03	1.11 (1)	1.13 (1)	0.88 (44)	0.67 (3)	1.01 (2)	1.05 (1)
Total	100.2	100.0	100.1	99.0	99.9	100.0	99.5	99.5
En	76.6 (7)		71.9 (44)	73.1 (1)	74.7 (90)	70.0 (3)	75.7 (4)	83.7 (<1)
Fs	22.4 (5)		25.9 (42)	24.6 (1)	23.6 (81)	28.7 (3)	22.3 (4)	14.3 (<1)
Wo	0.93 (2)		2.20 (2)	2.26 (3)	1.76 (93)	1.32 (5)	2.01 (3)	2.03 (3)
Mg#	77.3 (6)	72.7 (2)	73.5 (45)	74.8 (1)	75.9 (85)	70.9 (3)	77.3 (4)	85.4 (<1)
Fe/Mn	24.0 (13)	43.9 (17)	30.2 (14)	28.6 (1)	29.7 (14)	29.4 (9)	32.0 (12)	25.5 (1)

* Values in parentheses represent 1 standard deviation.

Table 3.8. Rare earth-element chemistry of selected diogenite lithologies (ppm).

	D3	1σ	D4	1σ	D6	1σ	D7	1σ
La	36	7			29	7	158	16
Ce	62	6			65	6	395	29
Pr	18	3			14	3	70	7
Nd					111	36	303	57
Sm	67	11			70	21	183	31
Eu	11	2					33	7
Gd	78	24			106	26	283	42
Tb	13	4			21	4	55	6
Dy	112	24	43	6	166	26	501	48
Ho	32	5	10	2	52	5	120	11
Er	91	13	34	5	179	15	452	38
Tm	14	4	7	2	28	4	71	8
Yb	123	18	53	7	216	18	563	50
Lu	19	7	11	3	35	6	92	10
Eu/Eu*	0.49				0.02 ^a		0.45	

^a Calculated from detection limit of Eu

*Missing data values were either below the detection limit or produce poor statistics (i.e. [1σ/concentration]*100 <40)

Table 3.9. Representative pyroxene compositions in cumulate eucrite lithic clasts (wt.% oxide).

Type	C1		C2		C3	C4	
Phase	Pigeonite	Cpx	Pigeonite	Cpx	Pigeonite	Pigeonite	Cpx
Oxide	n=4	n=3	n=5	n=1	n=7	n=3	n=4
SiO ₂	50.7 (1)	51.2 (3)	52.6 (2)	52.4 (4)	49.2 (1)	49.7 (1)	50.9 (2)
TiO ₂	0.22 (5)	0.42 (2)	0.22 (2)	0.33 (1)	0.64 (5)	0.20 (3)	0.41 (5)
Al ₂ O ₃	0.27 (9)	0.75 (7)	0.53 (5)	0.86 (5)	0.97 (6)	0.23 (6)	0.68 (11)
Cr ₂ O ₃	0.11 (2)	0.26 (4)	0.33 (2)	0.48 (4)	0.25 (5)	0.09 (1)	0.28 (4)
FeO	30.8 (7)	14.2 (5)	23.1 (2)	10.0 (1)	26.3 (13)	34.3 (8)	17.2 (2)
MnO	0.88 (6)	0.45 (2)	0.79 (1)	0.41 (1)	0.84 (3)	1.05 (1)	0.52 (2)
MgO	16.0 (4)	12.3 (1)	21.7 (2)	14.6 (2)	10.5 (3)	12.3 (1)	10.5 (1)
CaO	1.22 (19)	20.1 (3)	1.51 (4)	21.1 (2)	10.6 (10)	2.25 (67)	19.6 (2)
Total	100.2	99.7	100.7	100.3	99.3	100.1	100.1
En	46.8 (9)	35.5 (2)	60.7 (1)	41.3 (3)	32.0 (8)	37.0 (2)	30.6 (1)
Fs	50.7 (13)	23.0 (7)	36.3 (2)	15.9 (3)	44.9 (21)	58.1 (14)	28.3 (2)
Wo	2.55 (38)	41.6 (9)	3.02 (9)	42.9 (1)	23.2 (23)	4.88 (15)	41.1 (3)
Mg#	48.0 (11)	60.7 (6)	62.6 (2)	72.2 (5)	41.6 (12)	39.0 (5)	52.0 (1)
Fe/Mn	34.7 (20)	31.8 (22)	28.8 (2)	24.1 (4)	30.7 (11)	32.4 (7)	32.7 (13)
An	90 to 93		94 to 95		88 to 92	88 to 91	

* Values in parentheses represent 1 standard deviation.

Table 3.10. Representative pyroxene compositions in basaltic eucrite lithic clasts (wt.% oxide).

Type	B1		B2		B3		B4	
Phase	Pigeonite n=2	Cpx n=3	Pigeonite n=1	Cpx n=5	Pigeonite n=6	Cpx n=7	Pigeonite n=13	Cpx n=4
SiO ₂	49.4 (1)	50.2 (3)	48.6	50.0 (3)	49.3 (3)	50.6 (2)	49.2 (3)	50.4 (3)
TiO ₂	0.21 (6)	0.50 (9)	0.28	0.36 (5)	0.17 (2)	0.46 (5)	0.18 (3)	0.37 (2)
Al ₂ O ₃	0.17 (1)	0.73 (13)	0.28	0.61 (6)	0.17 (2)	0.62 (7)	0.17 (3)	0.58 (2)
Cr ₂ O ₃	0.10 (1)	0.30 (6)	0.11	0.26 (4)	0.07 (2)	0.27 (3)	0.09 (3)	0.27 (7)
FeO	35.9 (3)	17.7 (5)	35.5	20.1 (2)	35.6 (9)	18.2 (4)	35.9 (5)	17.2 (4)
MnO	1.07 (1)	0.52 (2)	1.03	0.54 (1)	1.07 (3)	0.53 (2)	1.05 (5)	0.47 (2)
MgO	12.0 (1)	9.93 (20)	10.3	9.06 (2)	11.8 (5)	10.1 (3)	12.0 (2)	10.0 (5)
CaO	1.26 (20)	19.4 (2)	3.88	18.8 (2)	1.70 (50)	19.0 (2)	1.19 (4)	19.7 (8)
Total	100.1	99.4	99.9	99.8	100.2	100.2	99.1	99.0
En	36.2 (1)	29.4 (2)	31.1	26.8 (2)	35.8 (12)	29.8 (7)	36.3 (5)	29.6 (5)
Fs	61.0 (4)	29.4 (6)	60.4	33.2 (5)	60.5 (20)	30.0 (8)	61.1 (9)	28.5 (9)
Wo	2.74 (40)	41.3 (7)	8.45	39.9 (3)	3.70 (11)	40.2 (3)	2.6 (8)	41.9 (12)
Mg#	37.2 (2)	50.0 (4)	34.0	44.7 (5)	37.2 (15)	49.8 (12)	37.3 (5)	51.0 (7)
Fe/Mn	33.4 (3)	33.3 (18)	34.3	36.6 (13)	33.0 (10)	34.2 (14)	33.9 (13)	36.6 (5)
An	74 to 83		79 to 83		86 to 90		85 to 90	

* Values in parentheses represent 1 standard deviation.

Table 3.11. Mineral modes determined for thin-sections from the DOM 10 howardites.

		DOM	DOM	DOM	DOM	DOM
		10838,6	10838,10	10100,8	10100,21	10105,10
Euclite	Clinopyroxene	2.0	2.9	3.2	2.8	2.9
	Fe-rich pyroxene	0.2	0.3	0.2	0.1	0.1
	Basaltic pyroxene	9.2	39.7	21.2	9.6	23.0
	Cumulate pyroxene	9.9	6.3	9.0	15.9	8.2
	High Fe-Ca pyroxene	0.8	1.6	3.3	0.7	2.9
	Plagioclase	12.3	30.2	26.4	14.7	29.4
	Silica	1.0	2.4	4.6	1.1	3.0
	Ilmenite	0.1	0.1	0.3	0.2	0.2
	K-feldspar	b.d.	b.d.	b.d.	b.d.	b.d.
	Phosphate	b.d.	b.d.	0.1	b.d.	0.1
	Olivine Fo ₁₆₋₆₀	0.1	0.1	0.1	0.2	0.1
Diogenite	Diogenite pyroxene	40.0	3.1	13.7	35.7	16.4
	Olivine Fo ₆₁₋₇₉	2.0	b.d.	0.6	2.5	0.5
	Metal and troilite	0.1	b.d.	0.7	0.2	0.4
	Chromite	0.6	0.2	0.3	0.8	0.4
Harzburgite mantle	Olivine Fo ₈₀₋₉₂	13.0	b.d.	1.1	3.0	0.2
	Orthopyroxene En ₈₅₋₈₈	1.0	b.d.	0.2	0.6	0.1
	Symplectite	0.1	b.d.	b.d.	b.d.	b.d.
Exogenic	Olivine Fo _{>98}	b.d.	b.d.	b.d.	b.d.	b.d.
	CM components	0.3	2.2	1.4	0.4	0.9
	Fusion crust	2.4	0.4	3.1	3.3	2.1
	Impact melts	1.1	1.3	2.0	3.9	2.8
	Unclassified	3.8	9.2	8.4	4.6	6.5
	Euclite Minerals	35.5	83.6	68.5	45.2	69.8
	Diogenite Minerals	42.5	3.3	14.6	38.9	17.3
	Basaltic:Cumulate ^a	48:52	86:14	70:30	38:62	74:26
	Plag/(Plag+Euclite Px)	36.6	38.0	44.0	34.1	46.3
	Euclite:diogenite ^a	49:51	97:3	82:18	59:41	79:21
	Euclite minerals/ (Euclite+Diogenite minerals) ^b	45.5	96.2	82.4	53.7	80.2

^aCalculated using the procedure described by Lunning et al. (2016).

Table 3.12. Comparison of mineralogical characteristics for selected howardites.

	Surface Regolithic (Solar Wind-Rich)					Megaregolithic (Solar Wind-Poor)			Megaregolithic	
	Lunning et al. 2016		Fuhrman and Papike 1981			Beck et al. 2012	Labotka and Papike 1980			This work
	GRO 95 Paired	GRO 95602	Kapoeta	Bununu	Bhlogati	PCA 02 Paired ^b	Yurtuk	Frankfort	Pavlovka	DOM 10 Paired
Basaltic eucrite opx+pig En _{<45}	14.0	21.4	9.0	5.9	9.8	10.8	0.5	1.1	6.7	19.1
Cumulate eucrite opx+pig En ₄₆₋₆₅	14.6	12.0	15.4	18.5	8.8	6.0	41.3	16.6	4.1	9.5
Diogenite opx En ₆₆₋₈₅	30.7	18.4	24.4	22.0	19.1	56.2	22.6	56.6	58.6	25.3
Plagioclase	19.5	23.8	11.6	13.3	8.4	10.0	24.8	14.4	17.1	20.5
Component proportions										
Total eucrite:diogenite ratio ^a	65:35	78:22	67:33	69:31	66:34	38:62	79:21	38:62	27:73	69:31
Plag/(plag+eucrite px)	37.7	38.9	32.2	35.3	31.2	44.6	39.2	49.8	63.0	39.6
Basaltic:cumulate eucrite px ratio	49:51	64:36	37:63	24:76	53:47	64:36	1:99	6:94	63:37	67:33

^aExtrapolated from opx+pig projecting eucrites proportionally have 50% plagioclase

^bAverage of PCA 02. Weighted by number of classified pixels per section (Beck et al. 2012 plus pixel counts courtesy of Andrew Beck).

Chapter 4: A Novel Approach to Petrologic Investigations Using Quantitative Compositional Mapping and Image Processing: A view from analysis of meteorite sample NWA 2995

Disclosure: The following chapter is in preparation for submission to the Journal of American Mineralogist, as a result of the primary author's graduate research. Co-authorship is shared with Paul K. Carpenter, Sarah N. Valencia, Nicole G. Lunning, John J. Donovan, Ryan A. Zeigler, Randy L. Korotev, and Bradley L. Jolliff. Timothy M. Hahn Jr. prepared the manuscript. The content of the chapter contains the original submission materials in an unaltered form prior to co-author revisions.

Abstract

We present the first integration of fully quantitative electron probe microanalysis (EPMA) compositional mapping with remote sensing software Environment for Visualizing of Images (ENVI) and IDL Workspace. Compositional, mineralogical, and lithological distribution maps of complex meteorite breccia Northwest Africa (NWA) 2995 are used to demonstrate the applicability of our newly developed data acquisition and image classification techniques to relevant petrologic problems. We applied a supervised classification procedure in ENVI (i.e., minimum distance in n-dimensional chemical space) to classify the mineralogy of NWA 2995 (e.g., bulk sample, matrix, and individual lithic clasts). The resulting classification images are used to extract the processed wt. % element data by mineralogy, clast type, and mineral fragments derived from the matrix. Using ENVI protocols and IDL routines, images are generated, which contain information regarding stoichiometry, mineral end-member compositions, elemental ratios, phase distribution, and fracture porosity. Additionally, average mineral compositions are

calculated; density-corrected bulk composition reconstructions are performed on lithic clasts, matrix components, and exsolved or zoned minerals. Our methods provide a powerful tool for petrologic investigations and alleviate current issues with similar techniques. We provide a new, easily accessible, tool for the interrogation of geologic materials.

4.1 Introduction

The petrology- and mineralogy-oriented communities have long recognized the need for the integration of quantitative chemical analyses with qualitative observations (e.g., textural analysis; Reed, 2005). Standard methods, however, are typically time intensive and require a mastery of optical microscopy. For example, mineral identifications and modal proportions are generally determined using transmitted or reflected light microscopy and point-counting of rock thin-sections, respectively. Additionally, large uncertainties can exist when identifying minerals and their proportions. In response to such difficulties and uncertainties, numerous efforts have focused on the integration of geochemical datasets and image processing software to extract and interpret geochemical information, while retaining textural relationships. Only moderate success has been achieved, however, as applications are commonly limited to simple systems that contain relatively few mineral phases with homogeneous chemical compositions (e.g., Maloy & Treiman, 2007; Prêt et al., 2010). Moreover, a long data-acquisition time is typically required.

In this paper we describe a new, highly effective method for petrologic investigations. Our analytical techniques and data processing routines are well suited for investigation of complex samples and for which only limited quantities exist (e.g., meteorites and Apollo breccias). Petrologic investigations that require high precision and accuracy are also well suited (i.e., resource exploration). We combine high-quality, quantitative EPMA compositional mapping with

remote sensing software ENVI, coupled with R data analysis and visualization techniques, to conduct comprehensive petrologic investigations using a semi-automated approach. Compositional, mineralogical, and lithological distribution maps of complex meteorite breccia Northwest Africa (NWA) 2995 (Figures 4.1 and 4.2) are used to demonstrate the applicability of our newly developed methods for petrologic investigations that incorporate quantitative petrography, bulk geochemistry, and clast chemistry (Figure 4.3).

4.2 Sample NWA 2995

Lunar meteorite NWA 2995 is a 538 gram feldspathic fragmental breccia collected in Algeria in 2005 (Connolly et al., 2006) and contains various fine-grained lithologies characteristic of the lunar highlands terrain (e.g., anorthosite, norite, gabbro, and granulitic and glassy impact melts), set in a glassy matrix. Chips of NWA 2995 have been analyzed by instrumental neutron activation analysis (INAA) and EPMA; comparison of compositional data supports the grouping of lunar meteorites NWA 2995, 2996, 3190, 4503, 5151, and 5152 (Connolly et al., 2006; Korotev et al., 2009; Mercer et al., 2013). Mean compositional data for NWA 2995 and associated meteorites suggest the breccia is a 2:1 mixture of feldspathic and mare material, with approximately 5% KREEP component (Korotev et al., 2009). Previous work has been conducted on NWA 2995 and paired stones, which characterized the petrography, clast inventory, petrology, and mineral chemistry of lithologic clasts within the breccias (e.g., Gross et al., 2014; Mercer et al., 2013). In this study, we combine recent advances in quantitative EPMA compositional mapping and image classification to demonstrate the applications of such methods for investigating the petrology and mineral chemistry of complex meteorite breccias. Specifically, we investigated the mafic clast inventory of a polished thick section of NWA 2995 to understand the

origin of mafic lithologies within the lunar highlands terrain and compare to previous petrologic investigations of paired stones (Figure 4.2).

4.3 Analytical procedure

The development of EPMA quantitative compositional mapping (QCM) methods has been a combined effort of many researchers and experts in microanalysis (Carpenter et al., 2017; Carpenter et al., 2013). Below, we briefly describe the data acquisition and correction procedures where appropriate; a companion paper that fully describes the methods and development of quantitative EPMA compositional mapping is currently in preparation. Consequently, the purpose of this paper is to demonstrate the applications and usefulness of such methods for investigating complex meteorite breccias or samples for which only limited quantities exist. Here, we specifically focus on methods of compositional data analysis and automated mineral classification routines.

4.3.1 Data acquisition

For this study, EPMA mapping experiments were done with the WUSTL JEOL JXA-8200 electron probe microanalyzer with 5 wavelength-dispersive spectrometers (WDS) and a silicon-drift energy dispersive spectrometer (EDS), using JEOL and Probe Software applications. The X-ray intensity maps were acquired using Probe Image and Calcimage software, which performs a full $\Phi(\rho z)$ correction at each pixel in the map (Carpenter et al., 2013). The calibration uses a conventional quantitative analysis standardization, with WDS background subtraction made using the mean atomic number (MAN) background correction (Donovan et al., 1996). The MAN background correction allows all counting time to be spent on the analytical peak, which significantly improves sensitivity during mapping. Two map passes were used to generate a 10-

element WDS compositional map (Figures 4.4 and 4.5), with typical acquisition times of 12-24 hours, and ~4 hours of computer time required for matrix correction of a 1024x1024 map. A summary graphic of the analytical conditions and setup of QCM is given in Figure 4.4.

4.3.2 Mineralogic classification algorithms and routines

Automated image classification and machine learning algorithms can be applied to the 10-element WDS compositional maps to classify the mineralogy of a thin section using knowledge of mineral compositions and formulas. Specifically, two approaches exist: 1) unsupervised classification (cluster analysis) and supervised classification (image classification). A schematic showing the two approaches, and examples of associated algorithms, is shown in Figure 4.6. Below, we describe the main advantages and disadvantages of unsupervised and supervised machine learning algorithms, and give examples of k-means clustering and k-nearest neighbors classification (i.e., minimum distance in n-dimensional chemical space, where n=10).

Unsupervised classification

Unsupervised classification (clustering) relies on pixel based classification, where the computer uses specific clustering algorithms to determine the natural, statistical groupings within the data. A few cluster algorithms are shown in Figure 4.6; however, only the K-means clustering algorithm is explored in this paper. Unsupervised classification algorithms are typically applied when the user has little to no prior knowledge of the sample (e.g., mineralogy or mineral chemistry). With unsupervised classification algorithms, the user defines a number of clusters and the computer statistically analyzes the data to assign each data point (i.e., image pixel) to a cluster. Because the data are assigned to each cluster via the computer and little prior information is assumed about the sample, the user is required to evaluate the classification data post classification to determine what each cluster represents (i.e., identify the mineral each cluster represents).

We used the k-means, unsupervised clustering algorithm to classify the mineralogy of NWA 2995 using the 10 element WDS compositional maps (Figure 4.7). The k-means classification algorithm is a partitional clustering algorithm that partitions the data into k clusters, with k specified by the user. Each cluster (k_i) has a centroid that is iteratively adjusted until the within-cluster sum of squares is minimized using Euclidean distance. The k-means algorithm is simple, intuitive, and efficient, and is therefore a popular clustering algorithm; however, the k-means algorithm requires the user to define k and is known to be sensitive to outliers within the dataset.

Supervised classification

Supervised classification algorithms rely on prior knowledge of the sample or dataset under investigation. With supervised classification, the user defines “training data” to train the classification algorithm. For example, a mineral class can be defined using compositional or stoichiometry information (e.g., Figure 4.5). The classification algorithm then uses the training instances to assign the remaining data (i.e., pixels) to the appropriate training class. A few examples of supervised classification algorithms are shown in Figure 4.6. With supervised classification algorithms, the majority of the effort is required from the user prior to classification of the dataset and requires specific care when selecting training data; however, after a classification model has been trained, the rule-based classification can be applied to new instances with relative ease. For instance, a mineral classification can be trained on a lunar sample (e.g., NWA 2995) and then be applied to a different lunar meteorite or even a meteorite from a completely different parent body (e.g., vestan meteorites) with only minor modifications required, with the assumption that the mineralogy is similar.

We applied a supervised classification procedure using ENVI (i.e., minimum distance in n-dimensional chemical space) to classify the mineralogy of NWA 2995 (e.g., bulk sample, matrix, and individual clasts; Table 4.1; Figure 4.8). Mineral phases were identified based on the elemental data (wt. % element), and ROIs selected accordingly, to develop a training set for classification

routines. We selected mineral phase ROIs on a clast-by-clast basis to potentially elucidate key features of the matrix mineralogy (e.g., from which clasts are mineral fragments derived?). Mineral classifications were performed iteratively, where in each successive classification, phases that are unclassified (i.e., compositionally distinct from other classified phases) are used to generate new ROIs and classification routines are iterated until the total unclassified pixels is $< 5\%$.

4.3.3 Ground-truth validation:

The mineralogic classification results from both unsupervised and supervised classification algorithms can be validated using externally determined class labels (Theodoridis & Koutroumbas, 2008). For example, electron microprobe spot analyses and EDS identification of mineral phases can be used to validate the accuracy of automated mineral identification and classification results. We collected ground truth data with the electron microprobe (e.g., point analyses) to characterize the mineralogy and mineral chemistry of NWA 2995; these data were then used to verify the automated mineral classification clusters. We observed that while both unsupervised and supervised classification algorithms provide similar results, the supervised classification routine provides additional benefits that make it the method of choice. Specifically, the supervised classification routine allows the user to more easily identify minor mineral phases in the sample that are small yet have differing compositions from the user-defined training data, and so are unclassified in the classification images (e.g., zircon). However, we note that unsupervised classification is useful for the initial exploratory analysis of the sample under investigation.

4.4 Results and Discussion

The electron microprobe is a powerful analytical tool for characterizing the geochemistry and mineral chemistry of meteorite samples but can also be useful for determining the bulk composition of a sample. For example, modal recombination analysis (MRA) uses average mineral compositions, mineral proportions, and mineral densities to estimate the bulk composition of the sample using a simple mass balance approach. We determined the modal mineralogy and bulk composition of the matrix in NWA 2995 to compare to the bulk composition determined by fused bead analysis (Table 4.1). Additionally, three mafic clasts were selected and examined in detail (Figure 4.9).

Mineral classification maps for mafic clasts B, G, and H are shown in Figure 4.9. All quantitative EPMA compositional data are detailed in Table 4.1, where the density-corrected bulk composition of each clast is compared with: (a) the bulk composition for NWA 2995 (Maps 1 and 2), which represent large areas of the slab; (b) the matrix data, which is representative of the slab with clasts subtracted; and (c), with the EPMA fused-bead analysis (Korotev et al. 2006). Clasts B and G are subophitic olivine basalts (possibly too small to be representative, and containing excess olivine), and clast H is an ophitic olivine gabbro. Clast B contains subhedral olivine of two distinct compositions, low- and high-Ca pyroxene, ilmenite, and spinel, and has a basaltic composition with a comparatively high FeO content (21 wt.%). Clast G contains olivine, low-Ca pyroxene, plagioclase, and spinel. Clast H contains low- and high-Ca pyroxene, plagioclase, minor olivine, and has a relatively aluminous composition.

There is excellent agreement between the matrix bulk composition determined by compositional mapping and the fused-bead EPMA data acquired previously, indicating that both techniques can be used to accurately measure the bulk composition of meteorites as represented

by subsampled areas. A main advantage of quantitative EPMA compositional map data is in comparison of areas representing spatial domains of essentially point analyses, phases, and lithic regions. This advantage can be used to compare clast and matrix composition, characterize mineral zoning, and to determine the abundance of mineral fragments and glass. In addition to treatment of map data using fully quantified concentrations, the procedure outlined here can be used to characterize samples based on the classification (e.g., pyroxene type; Figure 4.10) and further clustering and classification algorithms can be applied to these subsets of the original data to further delineate characteristics of the sample. For example, pixels classified as pyroxene in the original classification can be subset and then a separate unsupervised clustering algorithm can be applied to estimate the number of pyroxene types in the sample (Figure 4.10); these data can then be visualized in typical compositional spaces (e.g., pyroxene end-member ternary) to assess the variation in pyroxene types (Figure 4.12).

4.6 Summary and Future Work

We combined new, advanced methods of microanalysis (quantitative EPMA compositional mapping) with statistical clustering and image classification algorithms, with the goal of developing new methods of characterizing complex meteorite breccias. Compositional, mineralogical, and lithological distribution maps of lunar meteorite Northwest Africa 2995 was used to demonstrate the applicability of our newly developed data acquisition and image classification techniques to relevant petrologic problems. Supervised classification procedures were applied to classify the mineralogy of NWA 2995 (e.g., bulk sample, matrix, and individual lithic clasts). Classification images were then used to extract the processed wt. % element data by mineralogy and clast type. Using the methods developed in this paper, we generated images that contain information regarding stoichiometry, mineral end-member compositions, elemental ratios,

phase distribution, and fracture porosity. Additionally, average mineral compositions can be combined with nominal mineral densities to estimate the density-corrected bulk composition of selected regions; this method was applied to mafic lithic clasts and the matrix of NWA 2995. The methods developed in this paper provide a powerful tool for petrologic investigations and a new, easily accessible, tool for the interrogation of geologic materials. Future work includes development of a semi-automated classification procedure that uses linear discriminant analysis and requires minimal user input. Specifically, the semi-automated approach would capitalize on the strict stoichiometric constraints of minerals, which would help define training data for mineral classifications. Finally, incorporation of compositional data analysis routines that deal with the unique nature of compositional data (i.e., closure) will allow more robust statistical analyses to be applied to the quantitative compositional mapping data and allow the accuracy of classifications to be more readily determined.

Figures

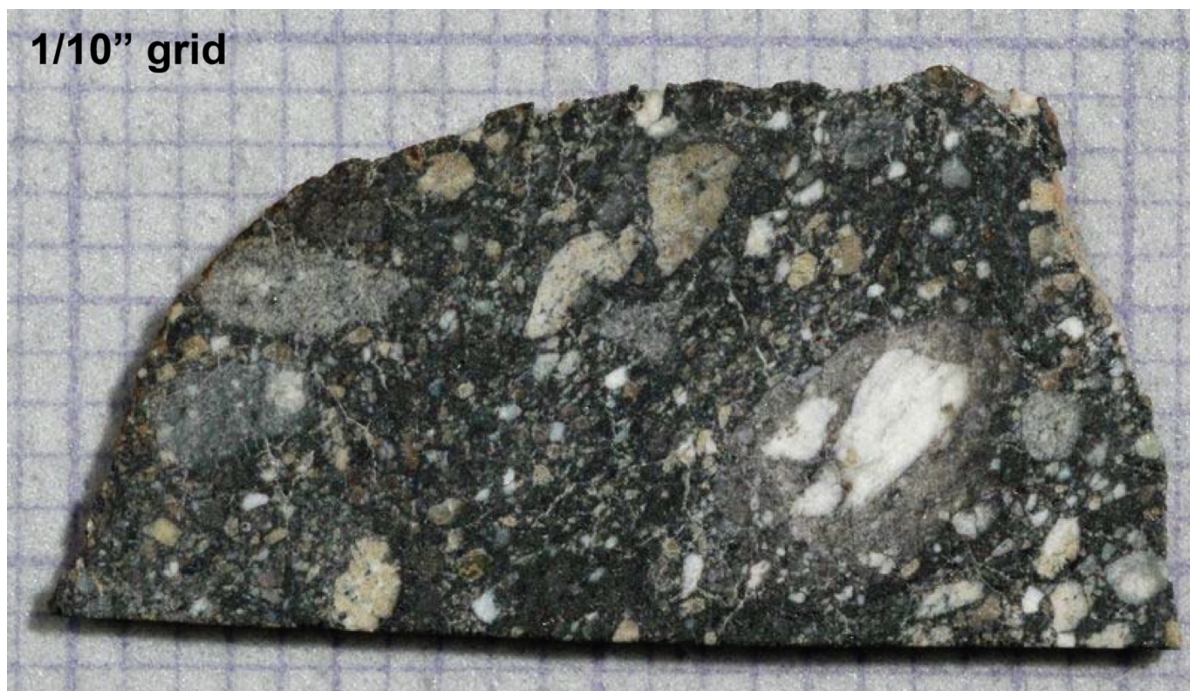


Figure 4.1: Sawn face of feldspathic fragmental breccia NWA 2995. (Photo credit: Randy Korotev; sample courtesy of Jim Strobe). NWA 2995 contains a variety of lithic clasts, comminuted mineral fragments, and distinct breccia domains.

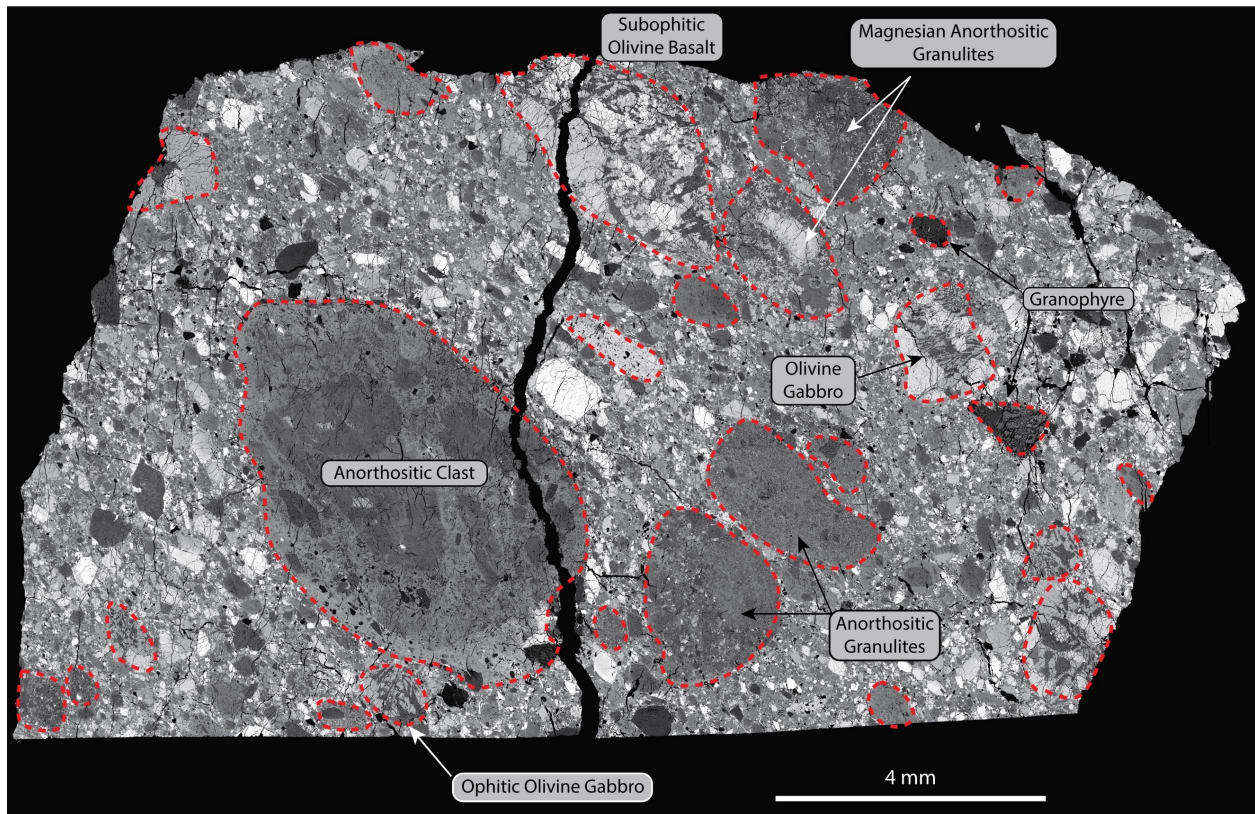


Figure 4.2: Backscattered electron image of NWA 2995. Red outlines denote the boundaries between obvious lithic clasts and adjacent matrix. Lithic clast range from anorthositic to gabbroic to basaltic. Granophyric clasts are also present.

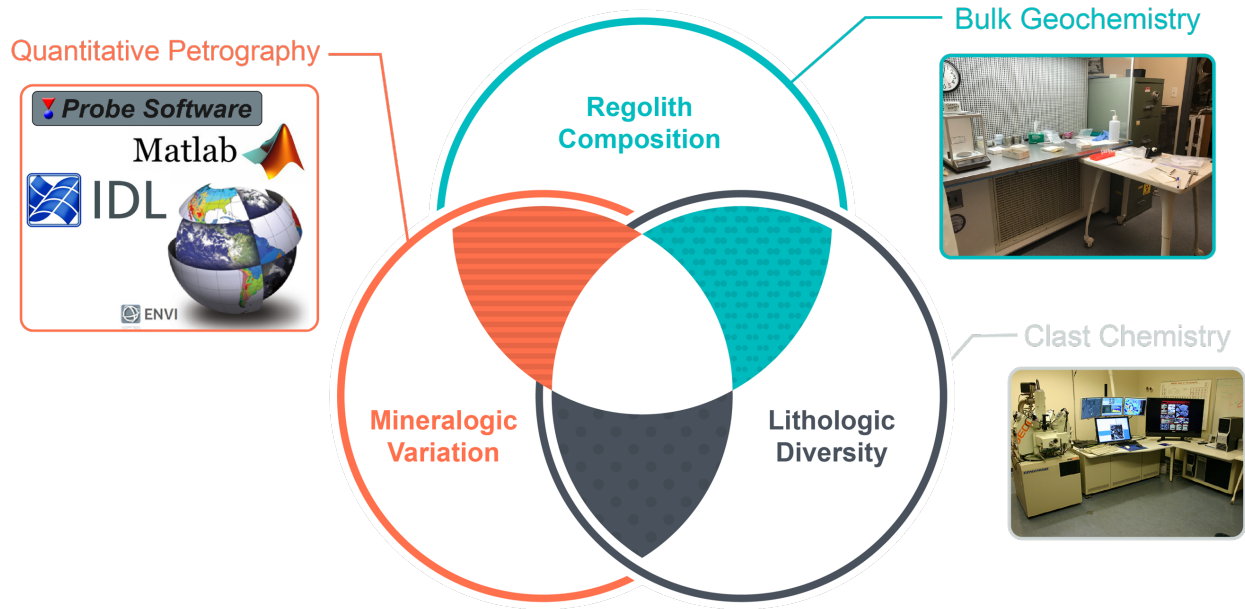
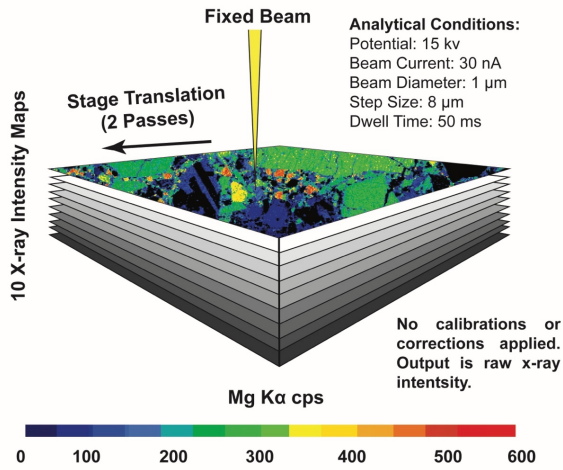


Figure 4.3: Schematic Venn diagram describing the components of a comprehensive petrologic investigation. An extensive petrologic characterization study consists of three specific tasks: 1) characterize the bulk geochemistry of the sample; 2) describe the lithologic diversity through detailed analysis of lithic clasts and associated mineral chemistry; 3) characterize the petrography of the sample, specifically with a qualitative, as well as a quantitative approach. These three tasks ensure that the petrogenesis of a sample is fully understood.

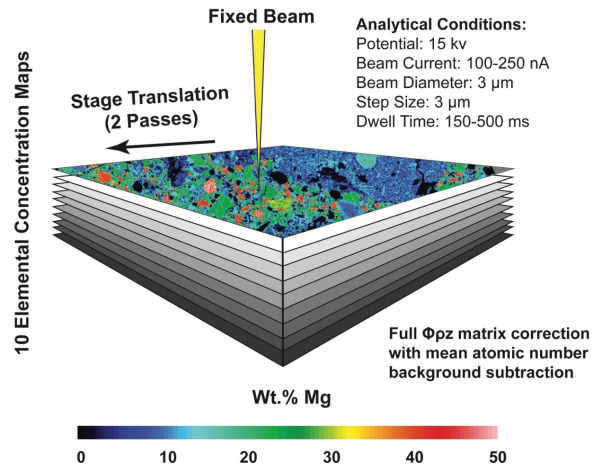
Mineralogic and Lithologic Mapping



Output Data Products:

- Mineralogic and lithologic distribution maps
- Modal mineralogy
- Fracture porosity

Quantitative Compositional Mapping



Output Data Products:

- Mineralogic and lithologic distribution maps
- Modal mineralogy
- Mineral stoichiometry
- Mineral end-member distribution maps
- Quantitative elemental ratio maps
- Fracture porosity
- Density-corrected bulk composition
- Quantitative variation diagrams

Figure 4.4: Summary graphic of the compositional mapping procedures. The mineralogic and lithologic mapping method (left) is a less robust method, and results in a mineralogic classification map of the sample under investigation. The quantitative compositional mapping (QCM) method (right) results in the same output (mineralogic classification); however, the QCM method has the added benefit of providing a quantitative compositional analysis at every pixel, which allows for additional data products to be produced during post-classification processing (see figure for details). Analytical conditions required for each approach is shown in the figure.

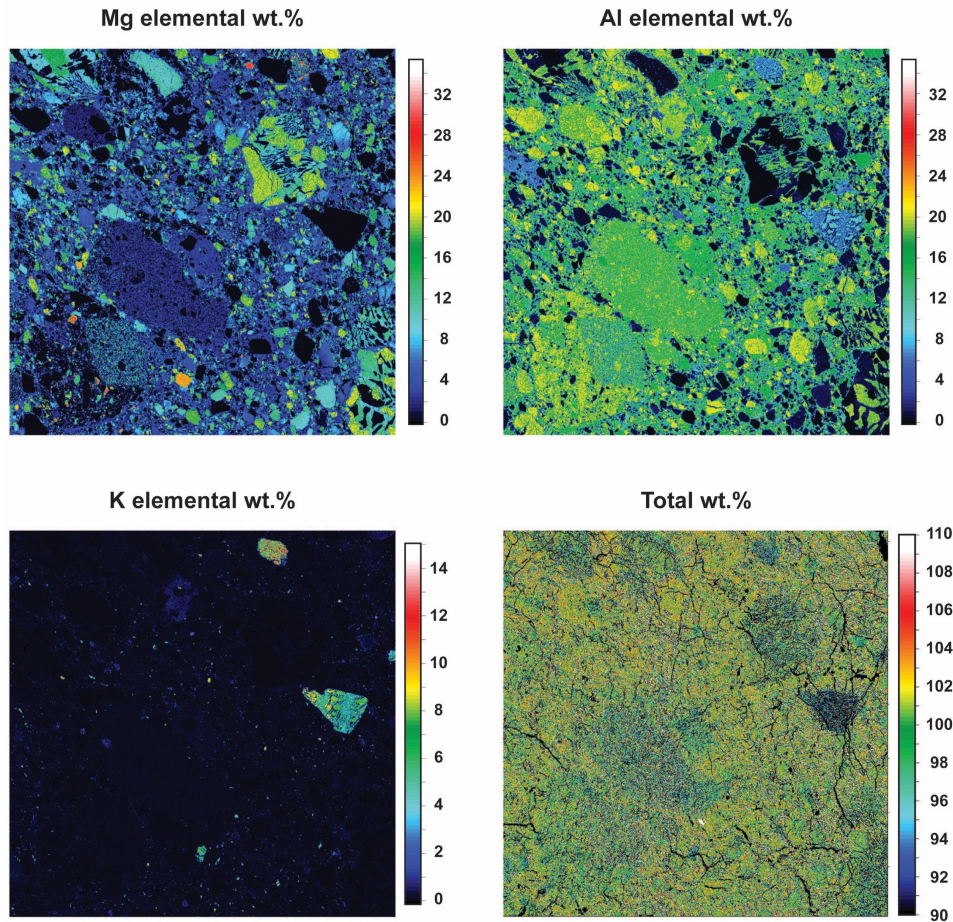


Figure 4.5: Quantitative elemental concentration maps for Mg, Al, and K. Total weight percent map is also shown, which gives the EPMA totals for each pixel. X-ray intensity maps are converted to quantitative elemental concentrations maps using a full $\Phi(\rho z)$ correction at each pixel in the map. The calibration uses a conventional quantitative analysis standardization; a MAN background correction is used to subtract WDS backgrounds. This background correction approach allows all counting time to be spent on the analytical peak and considerably improves sensitivity. Two stage maps are used to produce a 10 element WDS compositional map. Maps typically require ~12-24 hour runtimes, followed by several hours of computer processing for matrix and background corrections. After processing, a geochemical data cube is produced that contains a 10 element, fully quantitative WDS analysis at each pixel. K-rich, granophyre clasts are easily distinguishable in the K elemental concentration map. The Mg elemental concentration map shows areas of low wt.% Mg (feldspathic clasts) and areas of high wt.% Mg, which are characteristic of the mafic clasts in NWA 2995. Moreover, the total weight percent maps can be used to filter data prior to compositional data analysis and automated mineral classification algorithms. For instance, areas with low totals (e.g., epoxy-filled fractures and grain boundaries) can be removed prior to data analysis.

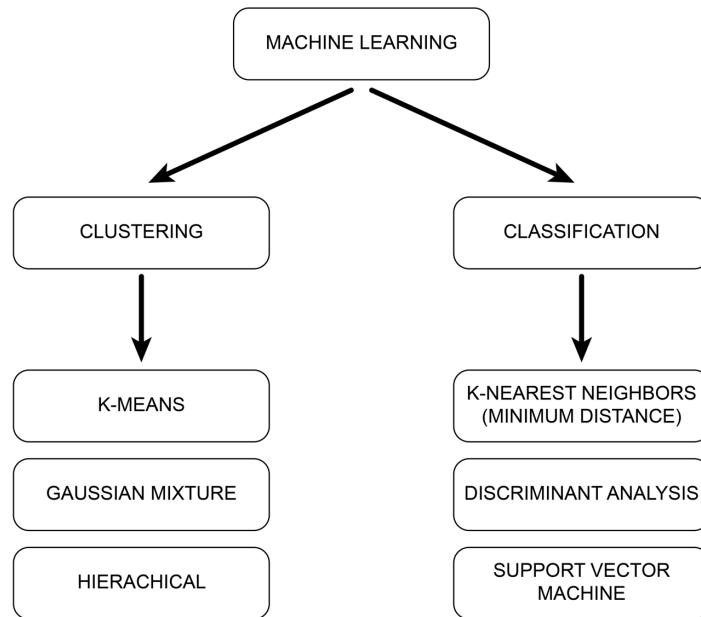
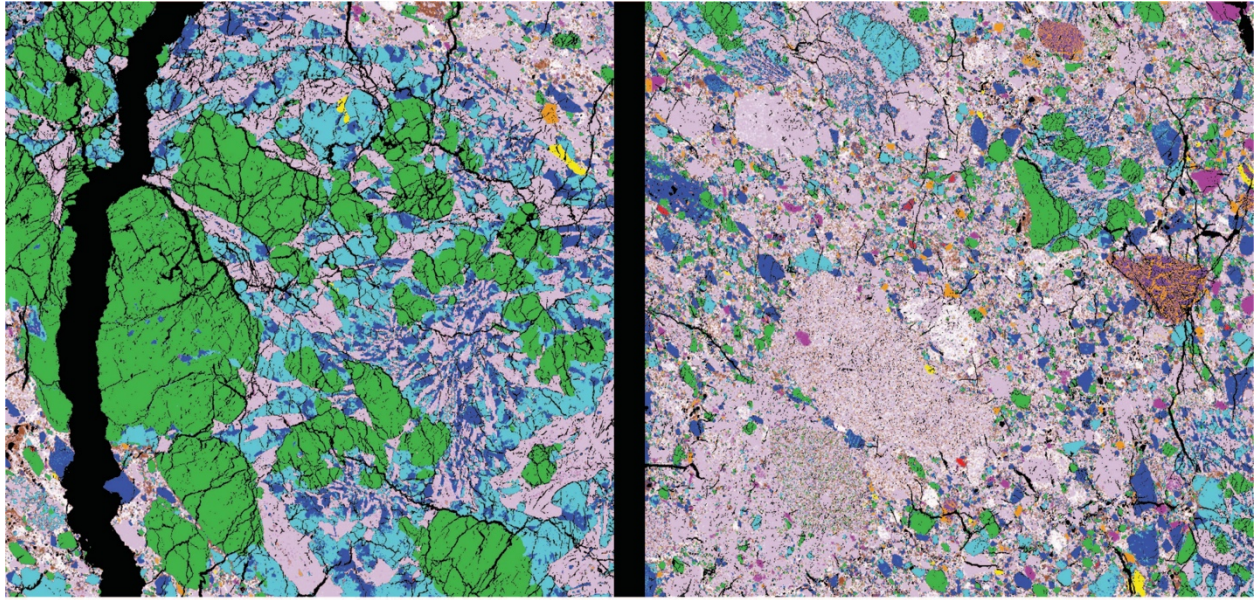


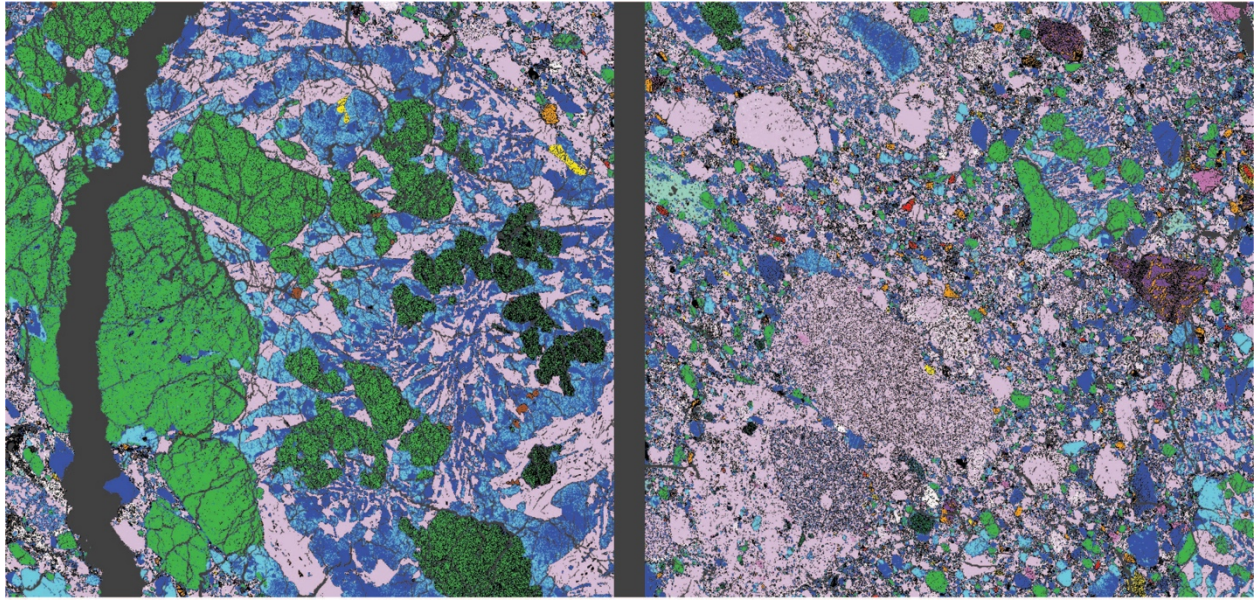
Figure 4.6: Schematic showing the two main approaches to machine learning applications in quantitative compositional mapping and mineralogic classification. Two approaches are used: unsupervised and supervised classification. Unsupervised classification (clustering) relies on pixel based classification, where the computer relies on specific clustering algorithms to determine the natural, statistical groupings within the data. A few cluster algorithms are shown; however, only the K-means clustering algorithm is explored in this paper. Unsupervised classification algorithms rely on a user-defined number of clusters and labels the data according to their assigned cluster; therefore, the user is required to evaluate the data post classification to determine what each cluster represents (i.e., identify the mineral each cluster represents). Supervised classification algorithms rely on prior knowledge of the sample or dataset under investigation. In supervised classification, the user defines “training data” to train the classification algorithm. The classification algorithm then uses the training instances to assign the remaining pixels to the appropriate training class. With supervised classification algorithms, the majority of the work is required from the user prior to classification of the dataset and requires specific care when selecting training data; however, after a classification model has been trained, the rule-based classification can be applied to new instances with relative ease. For instance, a mineral classification can be trained on a lunar sample (e.g., NWA 2995) and then be applied to a different lunar meteorite or even a meteorite from a completely different parent body (e.g., vestan meteorites) with only minor modifications required. If new minerals are present in the sample they will remain unclassified according to some user-defined parameters and can be used to further train the mineral classification model.



Legend

	Olivine		Spinel		Fa-rich Olivine
	High-Ca Pyroxene		Ilmenite		Na-plagioclase
	Low-Ca Pyroxene		K-feldspar		Melt
	Plagioclase		Silica		

Figure 4.7: Unsupervised clustering results for subophitic olivine basalt (left; Clast B) and Map Area 1 (right). The number of clusters selected was eleven in order to capture the common mineral phases observed in lunar meteorite breccias. The unsupervised cluster results contain no “unclassified” data values (black) because each data point is assigned to a cluster, unless otherwise specified using threshold parameters. Post-clustering identification of the phases is required when implementing unsupervised clustering algorithms.



Legend



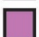

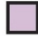

 Olivine	 Spinel	 Fa-rich Olivine
 High-Ca Pyroxene	 Ilmenite	 Na-plagioclase
 Low-Ca Pyroxene	 K-feldspar	 Melt
 Plagioclase	 Silica	

Figure 4.8: Supervised classification results for subophitic olivine basalt (Clast B) and Map Area 1. Eleven training sets were defined for classification purposes. Regions of interest were used to select training data from areas of known composition and/or mineralogy determined using energy dispersive spectrometers or wavelength dispersive spectrometers. Specifically, WDS point analysis was used to refine training data to select mineral phases of specified composition (e.g., pyroxene end-member compositions).

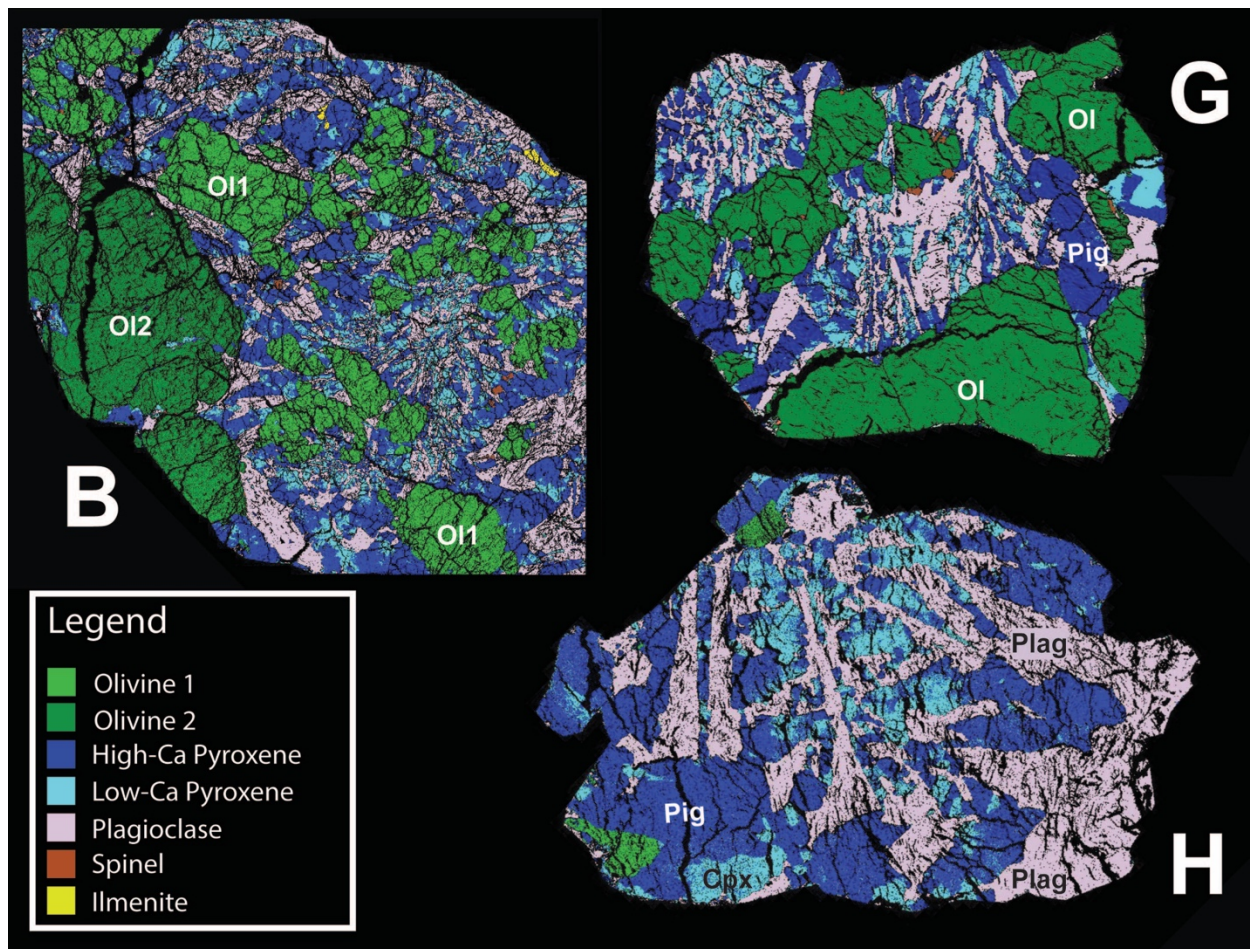


Figure 4.9: High spatial resolution classification images of lithic clasts in NWA 2995. Lithic clast data are isolated, and then used to calculate the density-corrected bulk composition; a similar routine is applied to the matrix component of the breccia to determine a representative bulk composition of the matrix and compare to spot analyses of impact melt.

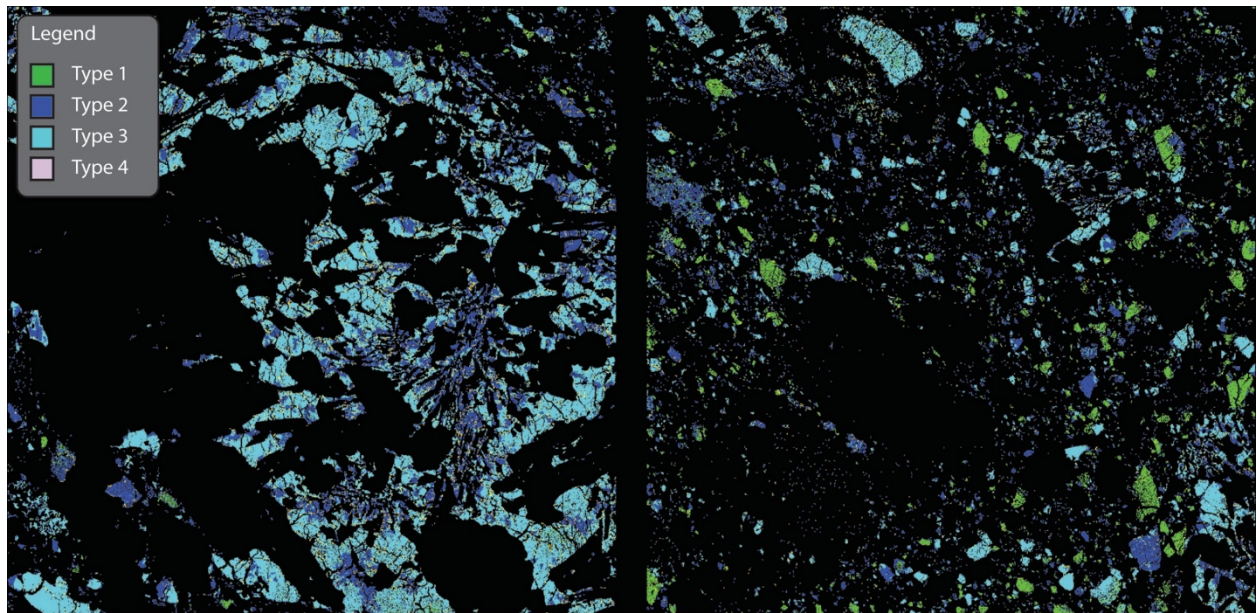


Figure 4.10: Unsupervised k-means clustering ($n=4$) of isolated pyroxene data. Pyroxenes are subset from the data using previous supervised classification rules and stoichiometric constraints. Application of the unsupervised k-means classification algorithm to the subset pyroxene data allows pyroxene compositions to be distinguished more readily and to determine natural, statistical grouping within the pyroxene data. (left) subophitic olivine basalt (Clast B). (right) Map area 1 in NWA 2995 BSE image.

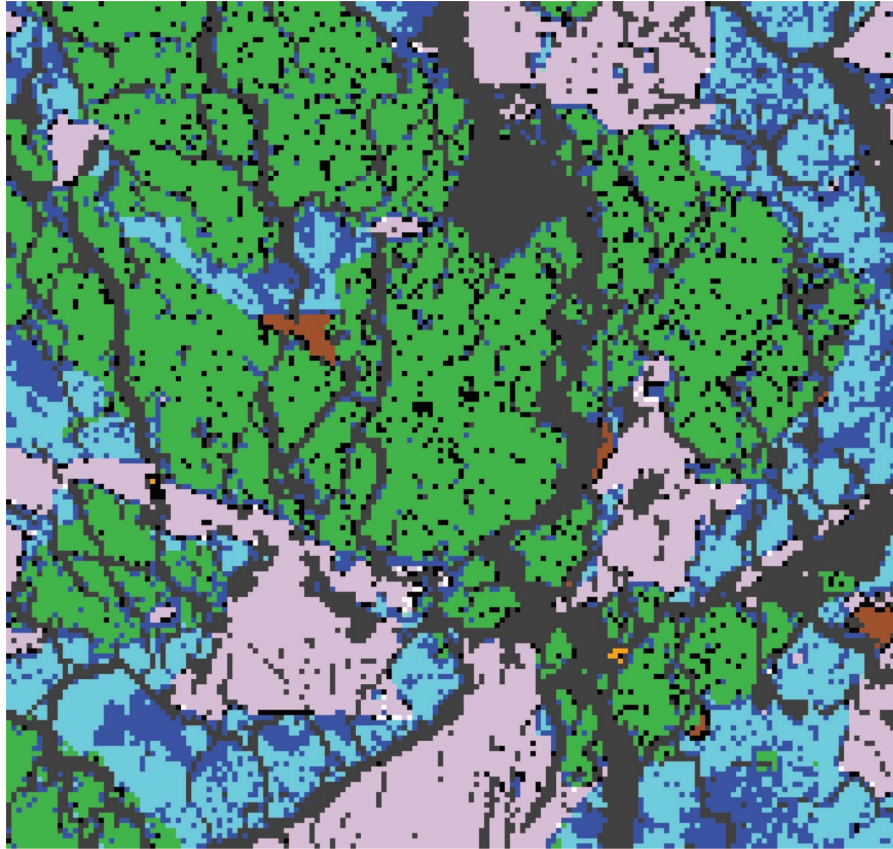


Figure 4.11: Detailed view of supervised classification results. Grain boundaries and epoxy-filled fractures introduce noise and error to the classification results but can be filtered according to the total wt.% for each 10-element quantitative analysis. Small, minor phases consisting of only a few pixels can be classified accurately (e.g., small spinel and silica grains). Image dimensions $\sim 1\text{mm} \times 1\text{mm}$. Black pixels are those that have been assigned to the “unclassified” class because they violate threshold parameters set for each group. We find that unclassified pixels are typically minor phases for which we have not created training data or pixels that contain overlapping phases or a mixture of phases (e.g., grain boundaries).

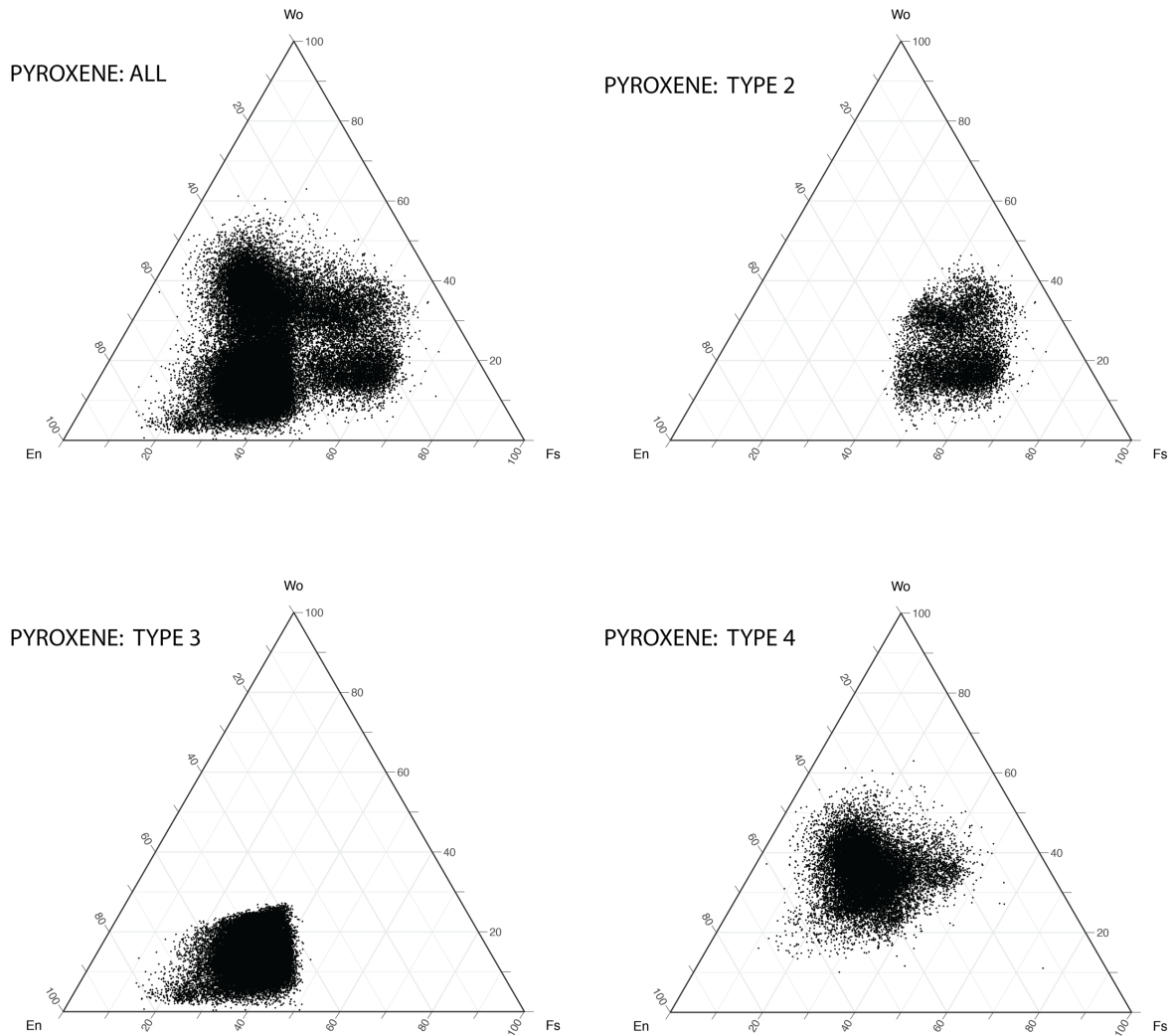


Figure 4.12: End-member compositions for pyroxene types in Figure 4.10, which have been separated based on a $n=4$ k-means clustering algorithm. The pyroxene types reflect typical pyroxene compositions (e.g., orthopyroxene, pigeonite, and augite); however, the natural compositional trends in pyroxene appear truncated, as expected. The cluster algorithm relies on similarities in the pyroxene compositions and attempts to reduce the within-cluster compositional variation and does not consider the petrologic and/or geochemical trends that develop during mineral crystallization (e.g., Mg-rich pyroxene cores and Fe-rich rims pyroxene rims).

Tables

Table 1. Calculated bulk composition of selected regions. (wt.% oxide)

Oxide	Fused Bead	Matrix	Clasts			Fused Bead	Matrix	Clasts			
			B	G	H			B	G	H	
SiO₂	46.2	46.3	43.4	43.6	49.6	Mg #	59.6	60.0	62.7	66.8	69.5
TiO₂	0.68	0.53	0.42	0.22	0.29	En			45 to 54	48 to 60	49 to 60
Al₂O₃	20.6	21.4	7.44	6.96	15.1	Wo			14 to 33	13 to 35	13 to 33
Cr₂O₃	0.23	0.2	0.31	0.34	0.38	An			91	89	90
MgO	8.08	8.11	19.8	22.3	12.8	Ab			9	10	9
CaO	13.5	13.1	7.24	6.53	12.8	Modal Analysis					
MnO	0.15	0.13	0.27	0.26	0.19	Fo			58 to 68	65	66
FeO^T	9.75	9.65	21	19.8	10	Plag			22.8	21.3	44.4
Na₂O	0.51	0.6	0.22	0.22	0.44	OI-1			22.7	47.6	1.68
K₂O	0.19	0.15	0.02	0.03	0.05	OI-2			18		
Total	99.9	100.2	100.1	100.3	101.7	High-Ca Px			11	10.2	15.8
						Low-Ca Px			25.1	20.7	38.2
						Ilm			0.2		
						Sp			0.36	0.27	

References

- Adams, J. B., C. Pieters, T. B. McCord (1974) Orange glass: Evidence for regional deposits of pyroclastic origin on the Moon. *Proc. Lunar Sci. Conf. 5th*, 171-186.
- Anders, E., & Grevesse, N. (1989). Abundances of the elements - Meteoritic and solar. *Geochimica et Cosmochimica Acta*, 53, 197-214.
- Ashley, J. W., Robinson, M. S., Stopar, J. D., Glotch, T. D., Hawke, B. R., van der Bogert, C. H., et al. (2016). The Lassell massif-A silicic lunar volcano. *Icarus*, 273, 248-261.
- Beck, A. W., Lawrence, D. J., Peplowski, P. N., Prettyman, T. H., McCoy, T. J., McSween, H. Y., et al. (2015). Using HED meteorites to interpret neutron and gamma-ray data from asteroid 4 Vesta. *Meteoritics & Planetary Science*, 50 (8), 1311-1337.
- Beck, A. W., McCoy, T. J., Sunshine, J. M., Viviano, C. E., Corrigan, C. M., Hiroi, T., & Mayne, R. G. (2013). Challenges in detecting olivine on the surface of 4 Vesta. *Meteoritics & Planetary Science*, 48 (11), 2155-2165.
- Beck, A. W., & McSween, H. Y. (2010). Diogenites as polymict breccias composed of orthopyroxenite and harzburgite. *Meteoritics and Planetary Science*, 45 (5), 850-872.
- Beck, A. W., Mittlefehldt, D. W., McSween, H. Y., Rumble, D., Lee, C. T., & Bodnar, R. J. (2011). MIL 03443, a dunite from asteroid 4 Vesta: Evidence for its classification and cumulate origin. *Meteoritics and Planetary Science*, 46 (8), 1133-1151.
- Beck, A. W., Welten, K. C., McSween, H. Y., Viviano, C. E., & Caffee, M. W. (2012). Petrologic and textural diversity among the PCA 02 howardite group, one of the largest pieces of the Vestan surface. *Meteoritics and Planetary Science*, 47 (6), 947-969.
- Bischoff, A., Scott, E. R., Metzler, K., & Goodrich, C. A. (Eds.). (2006). *Nature and origins of meteoritic breccias*.
- Brown, R. W. (1977). A sample fusion technique for whole rock analysis with the electron microprobe. *Geochimica et Cosmochimica Acta*, 41 (3), 435-438.
- Carpenter, P. K., Hahn, T. M., Korotev, R. L., & Jolliff, B. (2017). *Quantitative EPMA Compositional Mapping and Analysis of NWA 2995: Characterization and Petrologic Interpretation of Mafic Clasts*. Paper presented at the 48th Lunar and Planetary Science Conference.
- Carpenter, P. K., North, S. N., Jolliff, B., & Donovan, J. J. (2013). *EPMA Quantitative Compositional Mapping And Analysis Of Lunar Samples*. Paper presented at the 44th Lunar and Planetary Science Conference
- Cartwright, J. A., Ott, U., & Mittlefehldt, D. W. (2014). The quest for regolithic howardites. Part 2: Surface origins highlighted by noble gases. *Geochimica et Cosmochimica Acta*, 140, 488-508.
- Cartwright, J. A., Ott, U., Mittlefehldt, D. W., Herrin, J. S., Herrmann, S., Mertzman, S. A., et al. (2013). The quest for regolithic howardites. Part 1: Two trends uncovered using noble gases. *Geochimica et Cosmochimica Acta*, 105, 395-421.
- Chandrasekhar, S. (1960). *Radiative transfer*. New York: Dover Publications.
- Chin, G., Brylow, S., Foote, M., Garvin, J., Kasper, J., Keller, J., et al. (2007). Lunar reconnaissance orbiter overview: The instrument suite and mission. *Space Science Reviews*, 129 (4), 391-419.
- Clegg, R. N., Jolliff, B. L., Robinson, M. S., Hapke, B. W., & Plescia, J. B. (2014). Effects of rocket exhaust on lunar soil reflectance properties. *Icarus*, 227, 176-194.

- Clegg-Watkins, R. N., Jolliff, B. L., Boyd, A., Robinson, M. S., Wagner, R., Stopar, J. D., et al. (2016). Photometric characterization of the Chang'e-3 landing site using LROC NAC images. *Icarus*, 273, 84-95.
- Clegg-Watkins, R. N., Jolliff, B. L., Watkins, M. J., Coman, E., Giguere, T. A., Stopar, J. D., & Lawrence, S. J. (2017). Nonmare volcanism on the Moon: Photometric evidence for the presence of evolved silicic materials. *Icarus*, 285, 169-184.
- Combe, J.-P., McCord, T. B., McFadden, L. A., Ieva, S., Tosi, F., Longobardo, A., et al. (2015). Composition of the northern regions of Vesta analyzed by the Dawn mission. *Icarus*, *In Press*.
- Connolly Jr., H. C., Zipfel, J., Grossman, J. N., Folco, L., Smith, C., Jones, R. H., et al. (2006). The Meteoritical Bulletin, No. 90, 2006 September. *Meteoritics & Planetary Science*, 41 (9), 1383-1418.
- Corrigan, C., Welzenbach, L., Beck, A. W., & Lunning, N. G. (Eds.). (2011). *Petrographic Description* (Vol. 34).
- De Sanctis, M. C., Ammannito, E., Capria, M. T., Tosi, F., Capaccioni, F., Zambon, F., et al. (2012). Spectroscopic Characterization of Mineralogy and Its Diversity Across Vesta. *Science*, 336, 697-700.
- Denevi, B. W., Blewett, D. T., Buczkowski, D. L., Capaccioni, F., Capria, M. T., De Sanctis, M. C., et al. (2012). Pitted Terrain on Vesta and Implications for the Presence of Volatiles. *Science*, 338 (6104), 246-249.
- Domingue, D., Palmer, E., Gaskell, R., & Staid, M. (2018). Characterization of lunar surface within Tsiolkovsky crater: Photometric properties. *Icarus*, 312, 61-99.
- Domingue, D., & Vilas, F. (2007). Local topographic effects on photometry and reflectance spectra of planetary surfaces: An example based on lunar photometry. *Meteoritics & Planetary Science*, 42 (10), 1801-1816.
- Donovan, J. J., T. N. Tingle (1996) An improved Mean Atomic Number correction for quantitative microanalysis. *Journal of the Microscopy Society of America* 2, 1-7.
- Donovan, J. J., Singer, J. W., & Armstrong, J. T. (2016). A new EPMA method for fast trace element analysis in simple matrices. *American Mineralogist*, 101 (7-8), 1839-1853.
- Duke, M. B., & Silver, L. T. (1967). Petrology of eucrite, howardites, and mesosiderites. *Geochimica et Cosmochimica Acta*, 31, 1637-1665.
- Fowler, G. W., Papike, J. J., Spilde, M. N., & Shearer, C. K. (1994). Diogenites as asteroidal cumulates: Insights from orthopyroxene major and minor element chemistry. *Geochimica et Cosmochimica Acta*, 58 (18), 3921-3929.
- Fowler, G. W., Papike, J. J., Spilde, M. N., & Shearer, C. K. (1995). Diogenites as asteroidal cumulates: Insights from orthopyroxene trace element chemistry. *Geochimica et Cosmochimica Acta*, 59 (14), 3071-3084.
- Fuhrman, M., & Papike, J. J. (1981). Howardites and polymict eucrites: Regolith samples from the eucrite parent body. Petrology of Bholgati, Bununu, Kapoeta, and ALHA76005. *Proceedings of Lunar and Planetary Science*, 1257-1279.
- Gross, J., Treiman, A. H., & Mercer, C. N. (2014). Lunar feldspathic meteorites: Constraints on the geology of the lunar highlands, and the origin of the lunar crust. *Earth and Planetary Science Letters*, 388, 318-328.
- Guillong, M., Meier, D. L., Allan, M. M., Heinrich, C. A., & Yardley, B. W. (2008). Appendix A6: SILLS: a MatLab-based program for the reduction of Laser Ablation ICP-MS data of

- homogeneous materials and inclusions. *Mineralogical Association of Canada Short Course*, 40, 328-333.
- Haase, I., Waehlich, M., Glaeser, P., Oberst, J., & Robinson, M. S. (2019). Coordinates and Maps of the Apollo 17 Landing Site. *Earth and Space Science*, 6 (1), 59-95.
- Hahn, T. M., Lunning, N., McSween, H. Y., Bodnar, R. J., & Taylor, L. A. (2017). Dacite Formation on Vesta During Late-stage Eucrite Crystallization. *Meteoritics and Planetary Science*, 52 (6), 1173-1196.
- Hahn, T. M., Lunning, N., McSween, H. Y., Bodnar, R. J., & Taylor, L. A. (2018). Mg-rich Harzburgites from Vesta: Mantle Residua or Cumulates from Planetary Differentiation? *Meteoritics and Planetary Science*, 53 (3), 514-546.
- Hapke, B. (2012a). Bidirectional reflectance spectroscopy 7 The single particle phase function hockey stick relation. *Icarus*, 221 (2), 1079-1083.
- Hapke, B. (2012b). *Theory of reflectance and emittance spectroscopy* (2nd ed.). New York: Cambridge University Press.
- Hapke, B., Denevi, B., Sato, H., Braden, S., & Robinson, M. (2012). The wavelength dependence of the lunar phase curve as seen by the Lunar Reconnaissance Orbiter wide-angle camera. *Journal of Geophysical Research-Planets*, 117.
- Heiken, G., & McKay, D. S. (1974). Petrography of Apollo 17 soils. *Proceedings of the Fifth Lunar and Planetary Science* 1,843-860.
- Helfenstein, P., & Shepard, M. K. (2011). Testing the Hapke photometric model: Improved inversion and the porosity correction. *Icarus*, 215 (1), 83-100.
- Helfenstein, P., & Veverka, J. (1987). PHOTOMETRIC PROPERTIES OF LUNAR TERRAINS DERIVED FROM HAPKES EQUATION. *Icarus*, 72 (2), 342-357.
- Henriksen, M. R., Manheim, M. R., Burns, K. N., Seymour, P., Speyerer, E. J., Deran, A., et al. (2017). Extracting accurate and precise topography from LROC narrow angle camera stereo observations. *Icarus*, 283, 122-137.
- Hsu, W., & Crozaz, G. (1996). Mineral chemistry and the petrogenesis of eucrites: I. Non-cumulate eucrites. *Geochimica et Cosmochimica Acta*, 60 (22), 4571-4591.
- Hsu, W., & Crozaz, G. (1997). Mineral chemistry and the petrogenesis of eucrites: II. Cumulate eucrites. *Geochimica et Cosmochimica Acta*, 61 (6), 1293-1302.
- Jaumann, R., Williams, D. A., Buczkowski, D. L., Yingst, R. A., Preusker, F., Hiesinger, H., et al. (2012). Vesta's Shape and Morphology. *Science*, 336 (6082), 687-690.
- Johnson, J. R., Shepard, M. K., Grundy, W. M., Paige, D. A., & Foote, E. J. (2013). Spectrogoniometry and modeling of martian and lunar analog samples and Apollo soils. *Icarus*, 223 (1), 383-406.
- Jolliff, B. (1999). Clementine UVVIS multispectral data and the Apollo 17 landing site: What can we tell and how well? *Journal of Geophysical Research-Planets*, 104 (E6), 14123-14148.
- Jolliff, B. L., Korotev, R. L., & Haskin, L. A. (1991). A ferroan region of the lunar highlands as recorded in meteorites MAC88104 and MAC88105. *Geochimica et Cosmochimica Acta*, 55 (11), 3051-3071.
- Jolliff, B., Watkins, R., Schonwald, A., & Hahn, T. M. (2018). *LROC Narrow Angle Camera Photometric Analysis of Crustal Lithologies: Pure Anorthosite Locales*. Paper presented at the European Planetary Science Congress 2018.
- Jolliff, B. L., Rockow, K. M., Korotev, R. L., & Haskin, L. A. (1996). Lithologic distribution and geologic history of the Apollo 17 site: The record in soils and small rock particles from the highland massifs. *Meteoritics & Planetary Science*, 31 (1), 116-145.

- Jolliff, B. L., Gillis J. J., Haskin L., Korotev R. L., and Wieczorek M. A. (2000). Major lunar crustal terranes: Surface expressions and crust-mantle origins. *Journal of Geophysical Research* **105**, 4197-4216.
- Korotev, R. L., & Kremser, D. T. (1992). Compositional variations in Apollo-17 soils and their relationship to the geology of the Taurus-Littrow Site. *Proceedings of Lunar and Planetary Science*, **22**, 275-301.
- Korotev, R. L., Zeigler, R. A., Jolliff, B. L., Irvin, A. J., & Bunch, T. E. (2009). Compositional and lithological diversity among brecciated lunar meteorites of intermediate iron concentration. *Meteoritics & Planetary Science*, **44** (9), 1287-1322.
- Lemelin, M., Lucey, P. G., Gaddis, L. R., Hare, T., & Ohtake, M. (2016). Global map products from the Kaguya multiband imager at 512 ppd: Minerals, FeO, and OMAT. Paper presented at the 47th Lunar and Planetary Science Conference.
- Li, L., & Mustard, J. F. (2000). Compositional gradients across mare-highland contacts: Importance and geological implication of lateral transport. *Journal of Geophysical Research-Planets*, **105** (E8), 20431-20450.
- Lucchitta, B. K. (1977). CRATER CLUSTERS AND LIGHT MANTLE AT APOLLO 17 SITE - RESULTS OF SECONDARY IMPACT FROM TYCHO. *Icarus*, **30** (1), 80-96.
- Lucey, P. G., Blewett, D. T., & Hawke, B. R. (1998). Mapping the FeO and TiO₂ content of the lunar surface multispectral imagery. *Journal of Geophysical Research-Planets*, **103** (E2), 3679-3699.
- Lucey, P. G., Taylor, G. J., & Malaret, E. (1995). ABUNDANCE AND DISTRIBUTION OF IRON ON THE MOON. *Science*, **268** (5214), 1150-1153.
- Lunning, N. G., Hahn, T. M., Beck, A. W., & McSween, H. Y. (2015). *Lithologic Mapping of Howardites: How Many Thin Sections Are Enough*. Paper presented at the 78th Annual Meteoritical Society.
- Lunning, N. G., McSween, H. Y., Tenner, T. J., Kita, N. T., & Bodnar, R. J. (2015). Olivine and pyroxene from the mantle of asteroid 4 Vesta. *Earth and Planetary Science Letters*, **418**, 126-135.
- Lunning, N. G., Welten, K. C., McSween, H. Y., Caffee, M. W., & Beck, A. W. (2016). Grosvenor Mountains 95 howardite pairing group: Insights into the surface regolith of asteroid 4 Vesta. *Meteoritics & Planetary Science*, **51** (1), 167-194.
- Maloy, A. K., & Treiman, A. H. (2007). Evaluation of image classification routines for determining modal mineralogy of rocks from X-ray maps. *American Mineralogist*, **92** (11-12), 1781-1788.
- Mandler, B. E., & Elkins-Tanton, L. T. (2013). The origin of eucrites, diogenites, and olivine diogenites: Magma ocean crystallization and shallow magma chamber processes on Vesta. *Meteoritics and Planetary Science*, **48** (11), 2333-2349.
- Marchi, S., McSween, H. Y., O'Brien, D. P., Schenk, P., De Sanctis, M. C., Gaskell, R., et al. (2012). The Violent Collisional History of Asteroid 4 Vesta. *Science*, **336** (6082), 690-694.
- Martin, A. C., Boyd, A. K., Robinson, M. S., & Team, t. L. (2018). *Controlling LROC NAC Photometric Images*. Paper presented at the 49th Lunar and Planetary Science Conference.
- Marzari, F., Cellino, A., Davis, D., Farinella, P., Zappala, V., & Vanzani, V. (1996). Origin and evolution of the Vesta asteroid family. *Astronomy and Astrophysics*, **316**, 248-262.
- Mathworks. (2017a). *Global Optimization Toolbox User's Guide*. In Vol. 2017b. Retrieved from <https://www.mathworks.com/help/gads/>

- Mathworks. (2017b). *Parallel Computing Toolbox™ User's Guide*. In Vol. 2017b. Retrieved from <https://www.mathworks.com/help/parallel-computing/index.html>
- Mathworks. (2018a). *Optimization Toolbox™ User's Guide*. In Vol. 2018a. Retrieved from https://www.mathworks.com/help/pdf_doc/optim/index.html
- Mathworks. (2018b). *Symbolic Math Toolbox™ User's Guide*. In Vol. 2018a. Retrieved from <https://www.mathworks.com/help/symbolic/>
- Mayne, R. G., McSween, H. Y., McCoy, T. J., & Gale, A. (2009). Petrology of the unbrecciated eucrites. *Geochimica et Cosmochimica Acta*, 73 (3), 794-819.
- McCord, T. B., Adams, J. B., & Johnson, T. V. (1970). Asteroid Vesta: Spectral Reflectivity and Compositional Implications. *Science*, 168 (3938), 1445-1447.
- McCord, T. B., Clark, R. N., Hawke, B. R., McFadden, L. A., Owensby, P. D., Pieters, C. M., & Adams, J. B. (1981). Moon - near-infrared spectral reflectance, a 1st good look. *Journal of Geophysical Research*, 86 (NB11), 883-892.
- McSween, H. Y., Binzel, R. P., De Sanctis, M. C., Ammannito, E., Prettyman, T. H., Beck, A. W., et al. (2013). Dawn; the Vesta-HED connection; and the geologic context for eucrites, diogenites, and howardites. *Meteoritics and Planetary Science*, 48 (11), 2090-2104.
- Mercer, C. N., Treiman, A. H., & Joy, K. H. (2013). New lunar meteorite Northwest Africa 2996: A window into farside lithologies and petrogenesis. *Meteoritics & Planetary Science*, 48 (2), 289-315.
- Mittlefehldt, D., Ammannito, E., Hiroi, T., De Angelis, S., Di Iorio, T., Pieters, C., & De Sanctis, C. (2013). Towards Calibrating the Vestan Regolith: Correlating the Petrology, Chemistry and Spectroscopy of Howardites.
- Mittlefehldt, D. W. (1994). The genesis of diogenites and HED parent body petrogenesis. *Geochimica et Cosmochimica Acta*, 58 (5), 1537-1552.
- Mittlefehldt, D. W. (2015). Asteroid (4) Vesta: I. The howardite-eucrite-diogenite (HED) clan of meteorites. *Chemie der Erde - Geochemistry*, 75, 155-183.
- Mittlefehldt, D. W., Beck, A. W., Lee, C. T., McSween, H. Y., & Buchanan, P. C. (2012). Compositional constraints on the genesis of diogenites. *Meteoritics and Planetary Science*, 47 (1), 72-98.
- Mittlefehldt, D. W., Herrin, J. S., Quinn, J. E., Mertzman, S. A., Cartwright, J. A., Mertzman, K. R., & Peng, Z. X. (2013). Composition and petrology of HED polymict breccias: The regolith of (4) Vesta. *Meteoritics & Planetary Science*, 48 (11), 2105-2134.
- Mittlefehldt, D. W., & Lindstrom, M. M. (2003). Geochemistry of eucrites: genesis of basaltic eucrites, and Hf and Ta as petrogenetic indicators for altered antarctic eucrites. *Geochimica et Cosmochimica Acta*, 67 (10), 1911-1934.
- Morris, R. V. (1978). *The surface exposure (maturity) of lunar soils - Some concepts and Is/FeO compilation*. Paper presented at the Proceedings of the 9th Lunar and Planetary Science Conference.
- Muehlberger, W. R., Batson, R. M., Cernan, E. A., Freeman, V. L., Hait, M. H., Holt, H. E., et al. (1973). Preliminary geologic investigation of the Apollo 17 landing site. *Apollo 17 preliminary science report*, 6-1-6-91.
- Mustard, J. F., Li, L., & He, G. Q. (1998). Nonlinear spectral mixture modeling of lunar multispectral data: Implications for lateral transport. *Journal of Geophysical Research-Planets*, 103 (E8), 19419-19425.

- Pieters, C. M., Ammannito, E., Blewett, D. T., Denevi, B. W., De Sanctis, M. C., Gaffey, M. J., et al. (2012). Distinctive space weathering on Vesta from regolith mixing processes. *Nature*, 491 (7422), 79-82. 10.1038/nature11534.
- Pieters, C. M., Staid, M. I., Fischer, E. M., Tompkins, S., & He, G. (1994). A SHARPER VIEW OF IMPACT CRATERS FROM CLEMENTINE DATA. *Science*, 266 (5192), 1844-1848.
- Pommerol, A., Thomas, N., Jost, B., Beck, P., Okubo, C., & McEwen, A. S. (2013). Photometric properties of Mars soils analogs. *Journal of Geophysical Research-Planets*, 118 (10), 2045-2072.
- Pouchou, J.-L., & Pichoir, F. (1991). Quantitative analysis of homogeneous or stratified microvolumes applying the model "PAP". In *Electron probe quantitation* (pp. 31-75): Springer.
- Prêt, D., Sammartino, S., Beaufort, D., Meunier, A., Fialin, M., & Michot, L. J. (2010). A new method for quantitative petrography based on image processing of chemical element maps: Part I. Mineral mapping applied to compacted bentonites. *American Mineralogist*, 95 (10), 1379-1388.
- Prettyman, T. H., Mittlefehldt, D. W., Yamashita, N., Beck, A. W., Feldman, W. C., Hendricks, J. S., et al. (2013). Neutron absorption constraints on the composition of 4 Vesta. *Meteoritics & Planetary Science*, 48 (11), 2211-2236.
- Pun, A., Keil, K., Taylor, G. J., & Wieler, R. (1998). The Kapoeta howardite: Implications for the regolith evolution of the howardite-eucrite-diogenite parent body. *Meteoritics & Planetary Science*, 33 (4), 835-851.
- Raymond, C. A., Park, R. S., Konopliv, A. S., Asmar, S. W., Jaumann, R., McSween, H. Y., et al. (2014). *Geophysical Constraints on Vesta's Evolution*. Paper presented at the European Planetary Science Congress.
- Reddy, V., Gaffey, M. J., Kelley, M. S., Nathues, A., Li, J. Y., & Yarbrough, R. (2010). Compositional heterogeneity of Asteroid 4 Vesta's southern hemisphere: Implications for the Dawn mission. *Icarus*, 210 (2), 693-706.
- Reed, S. J. B. (2005). *Electron Microprobe Analysis and Scanning Electron Microscopy in Geology* (2 ed.). Cambridge: Cambridge University Press.
- Rhodes, J. M., Rodgers, K. V., Shih, C., Bansal, B. M., Nyquist, L., Wiesmann, H., & Hubbard, N. J. (1974). *The relationships between geology and soil chemistry at the Apollo 17 landing site*. Paper presented at the Proceedings of the Fifth Lunar Conference.
- Righter, K., & Drake, M. J. (1997). A magma ocean on Vesta: Core formation and petrogenesis of eucrites and diogenites. *Meteoritics & Planetary Science*, 32, 929-944.
- Robinson, M. S., & Jolliff, B. L. (2002). Apollo 17 landing site: Topography, photometric corrections, and heterogeneity of the surrounding highland massifs. *Journal of Geophysical Research-Planets*, 107 (E11).
- Ruesch, O., Hiesinger, H., De Sanctis, M. C., Ammannito, E., Palomba, E., Longobardo, A., et al. (2014). Detections and geologic context of local enrichments in olivine on Vesta with VIR/Dawn data. *Journal of Geophysical Research: Planets*, 119 (9), 2078-2108.
- Russell, C. T., Raymond, C. A., Coradini, A., McSween, H. Y., Zuber, M. T., Nathues, A., et al. (2012). Dawn at Vesta: Testing the Protoplanetary Paradigm. *Science*, 336, 684-686.
- Sato, H., Robinson, M. S., Hapke, B., Denevi, B. W., & Boyd, A. K. (2014). Resolved Hapke parameter maps of the Moon. *Journal of Geophysical Research-Planets*, 119 (8), 1775-1805.

- Sato, H., Robinson, M. S., Lawrence, S. J., Denevi, B. W., Hapke, B., Jolliff, B. L., & Hiesinger, H. (2017). Lunar mare TiO₂ abundances estimated from UV/Vis reflectance. *Icarus*, 296, 216-238.
- Schmitt, H. H., Petro, N. E., Wells, R. A., Robinson, M. S., Weiss, B. P., & Mercer, C. M. (2017). Revisiting the field geology of Taurus-Littrow. *Icarus*, 298, 2-33. Article.
- Schonwald, A. R., Hahn, T. M., Watkins, R. N., & Jolliff, B. (2018). *Investigating Local Variations of Lunar Rock Types at Sites of "Purest Anorthosite" Detection*. Paper presented at the American Geophysical Union.
- Seddio, S. M., Jolliff, B. L., Korotev, R. L., & Zeigler, R. A. (2013). Petrology and geochemistry of lunar granite 12032,366-19 and implications for lunar granite petrogenesis. *American Mineralogist*, 98 (10), 1697. 10.2138/am.2013.4330.
- Shearer, C. K., Burger, P., & Papike, J. J. (2010). Petrogenetic relationships between diogenites and olivine diogenites: Implications for magmatism on the HED parent body. *Geochimica et Cosmochimica Acta*, 74, 4865-4880.
- Shepard, M. K., & Helfenstein, P. (2007). A test of the Hapke photometric model. *Journal of Geophysical Research-Planets*, 112 (E3).
- Shepard, M. K., & Helfenstein, P. (2011). A laboratory study of the bidirectional reflectance from particulate samples. *Icarus*, 215 (2), 526-533.
- Stephan, K., Jaumann, R., De Sanctis, M. C., Tosi, F., Ammannito, E., Krohn, K., et al. (2014). Small fresh impact craters on asteroid 4 Vesta: A compositional and geological fingerprint. *Journal of Geophysical Research: Planets*, 119 (4), 771-797.
- Stoffler, D., Bischoff, A., Borchardt, R., Burghele, A., Deutsch, A., Jessberger, E. K., et al. (1985). COMPOSITION AND EVOLUTION OF THE LUNAR CRUST IN THE DESCARTES HIGHLANDS, APOLLO-16. *Journal of Geophysical Research*, 90, C449-C506.
- Takeda, H., & Graham, A. L. (1991). Degree of equilibration of eucritic pyroxenes and thermal metamorphism of the earliest planetary crust. *Meteoritics*, 26, 129-134.
- Thangjam, G., Nathues, A., Mengel, K., Hoffmann, M., Schäfer, M., Reddy, V., et al. (2014). Olivine-rich exposures at Bellicia and Arruntia craters on (4) Vesta from Dawn FC. *Meteoritics & Planetary Science*, 49 (10), 1831-1850.
- Thangjam, G., Nathues, A., Mengel, K., Schäfer, M., Hoffmann, M., Cloutis, E. A., et al. (2016). Three-dimensional spectral analysis of compositional heterogeneity at Arruntia crater on (4) Vesta using Dawn FC. *Icarus*, 267, 344-363.
- Theodoridis, S., & Koutroumbas, K. (2008). *Pattern Recognition, Fourth Edition*: Academic Press, Inc.
- Tooley, C. R., Houghton, M. B., Saylor, R. S., Jr., Peddie, C., Everett, D. F., Baker, C. L., & Safdie, K. N. (2010). Lunar Reconnaissance Orbiter Mission and Spacecraft Design. *Space Science Reviews*, 150 (1-4), 23-62.
- Trang, D., & Lucey, P. G. (2019). Improved space weathering maps of the lunar surface through radiative transfer modeling of Kaguya multiband imager data. *Icarus*, 321, 307-323.
- van der Bogert, C. H., Hiesinger, H., Iqbal, W., Clark, J. D., Robinson, M. S., Jolliff, B., et al. (2019). *TIMING OF RECENT EVENTS NEAR THE APOLLO 17 LANDING SITE*. Paper presented at the 50th Lunar and Planetary Science Conference.
- Warren, P. H., & Jerde, E. A. (1987). Composition and origin of Nuevo Laredo Trend eucrites. *Geochimica et Cosmochimica Acta*, 51 (3), 713-725.

- Warren, P. H., Kallemeyn, G. W., Huber, H., Ulf-Møller, F., & Choe, W. (2009). Siderophile and other geochemical constraints on mixing relationships among HED-meteoritic breccias. *Geochimica et Cosmochimica Acta*, 73 (19), 5918-5943.
- Wasson, J. T. (2013). Vesta and extensively melted asteroids: Why HED meteorites are probably not from Vesta. *Earth and Planetary Science Letters*, 381, 138-146.
- Wilson, J. T., V. R. Eke, R. J. Massey, R. C. Elphic, B. L. Jolliff, D. J. Lawrence, E. W. Llewellyn, J. N. McElwaine, L. F. A. Teodoro (2015) Evidence for explosive silicic volcanism on the Moon from the extended distribution of thorium near the Compton-Belkovich Volcanic Complex. *J. Geophys. Res.* 120, 92-108.
- Wolfe, E. W. (1981). The geologic investigation of the Taurus-Littrow valley, Apollo 17 landing site. *Washington: US Govt. Print. Off., 1981.*